



HAL
open science

Bulk topological states in a new collective dynamics model

Pierre Degond, Antoine Diez, Mingye Na

► **To cite this version:**

Pierre Degond, Antoine Diez, Mingye Na. Bulk topological states in a new collective dynamics model. SIAM Journal on Applied Dynamical Systems, 2022, 21 (2), pp.1455-1494. 10.1137/21M1393935 . hal-03119172v4

HAL Id: hal-03119172

<https://hal.science/hal-03119172v4>

Submitted on 4 Aug 2022

HAL is a multi-disciplinary open access archive for the deposit and dissemination of scientific research documents, whether they are published or not. The documents may come from teaching and research institutions in France or abroad, or from public or private research centers.

L'archive ouverte pluridisciplinaire **HAL**, est destinée au dépôt et à la diffusion de documents scientifiques de niveau recherche, publiés ou non, émanant des établissements d'enseignement et de recherche français ou étrangers, des laboratoires publics ou privés.

Bulk topological states in a new collective dynamics model*

Pierre Degond[†], Antoine Diez[‡], and Mingye Na[‡]

Abstract. In this paper, we demonstrate the existence of topological states in a new collective dynamics model. This individual-based model (IBM) describes self-propelled rigid bodies moving with constant speed and adjusting their rigid-body attitude to that of their neighbors. In previous works, a macroscopic model has been derived from this IBM in a suitable scaling limit. In the present work, we exhibit explicit solutions of the macroscopic model characterized by a non-trivial topology. We show that these solutions are well approximated by the IBM during a certain time but then the IBM transitions towards topologically trivial states. Using a set of appropriately defined topological indicators, we reveal that the breakage of the non-trivial topology requires the system to go through a phase of maximal disorder. We also show that similar but topologically trivial initial conditions result in markedly different dynamics, suggesting that topology plays a key role in the dynamics of this system.

Key words. individual-based model, macroscopic model, self-organization, topological phase transition, winding number, order parameter

AMS subject classifications. 22E70, 35Q70, 37B25, 60J76, 65C35, 70F10

1. Introduction. Systems of particles (or agents) which exhibit self-organized collective behavior are ubiquitous in the living world at all scales, from bird flocks [71] to sperm [27] or bacterial colonies [29]. Examples are also found in social sciences [18, 39] or for inert matter [15]. In such systems, the agents interact locally with a limited number of neighbors through rather simple rules such as attraction, repulsion or alignment [3, 26, 52] without any leader or centralized control. When the number of agents becomes large, vast structures encompassing many agents appear, such as clusters [72, 87], traveling bands [23], vortices [24, 29], lanes [25], etc. As there is no direct or apparent relation between these structures and the nature of the agents interactions, such a phenomenon is named “emergence”. Its study has stimulated a vast literature (see e.g. [87] for a review).

There are mainly two levels of description of particle systems: the most detailed one consists of individual based models (IBM) where the agents dynamics are described by coupled ordinary or stochastic differential equations. When the number of agents becomes large, a macroscopic description in terms of average quantities such as the agents mean density or velocity is preferred. The rigorous link between these two levels of description involves two

*Submitted to the editors January 21st, 2021

Funding: PD acknowledges support by the Engineering and Physical Sciences Research Council (EPSRC) under grants no. EP/M006883/1 and EP/P013651/1, by the Royal Society and the Wolfson Foundation through a Royal Society Wolfson Research Merit Award no. WM130048. The work of AD is supported by an EPSRC-Roth scholarship cofounded by the Engineering and Physical Sciences Research Council and the Department of Mathematics at Imperial College London.

[†]Institut de Mathématiques de Toulouse; UMR5219; Université de Toulouse; CNRS; UPS; F-31062 Toulouse Cedex 9, France (pierre.degond@math.univ-toulouse.fr, <https://sites.google.com/site/degond/Home>).

[‡]Department of Mathematics, Imperial College London, London, SW7 2AZ, United Kingdom (antoine.diez18@imperial.ac.uk, mingye.na18@imperial.ac.uk).

33 successive limits by which the number of agents is first sent to infinity (mean-field limit) and
34 then, the system size relative to the typical interaction distance between the agents is also
35 sent to infinity (hydrodynamic limit), see e.g. [21, 31]. In collective dynamics, particles are
36 capable of self-propulsion by transforming an internal source of chemical energy into motion
37 [87]. There are two main classes of IBM of self-propelled particles. The first class is based
38 on the Cucker-Smale model [4, 28, 55, 56] where self-propulsion is treated as an external
39 force. The second class is based on the Vicsek model [2, 19, 23, 29, 41, 45, 72, 86] where
40 self-propulsion is modeled by imposing the norm of the particle velocity to be a constant. At
41 the mean-field or hydrodynamic levels, the two frameworks give rise to corresponding models
42 (see e.g. [1, 5] for Cucker-Smale type models and [10, 34, 41, 45, 78, 85] for Vicsek type
43 models). The two categories are linked by an asymptotic limit [12, 13]. Of course, there are
44 many variants of these models and we refer to [8, 9, 17, 20, 42, 46, 74] for a non-exhaustive
45 set of examples.

46 Recently, a series of studies has investigated the existence of topological states in collective
47 dynamics. Topological states have appeared with the quantum Hall effect [67, 69, 75, 84] which
48 relies on so-called conducting chiral edge states: when a sample of a 2-dimensional insulator is
49 placed in a magnetic field, its bulk conductance is nil but a current can flow around its edges
50 in only one direction (hence the 'chiral' terminology). Then, materials that exhibit chiral edge
51 states without a magnetic field have been discovered, the so-called "topological insulators"
52 [58, 76, 79]. Chiral edge states are robust against perturbations because of their non trivial
53 topology which can be characterized by a integer, the winding number. Any destruction of the
54 chiral edge state would require a finite jump of this integer, which consumes a finite amount
55 of energy. Hence lower energy perturbations will fail to destroy the chiral edge state. This
56 property is of strategic interest for various applications such as quantum computers. Recently
57 a series of works have explored the occurrence of topological states in collective dynamics (see
58 e.g. [81, 82, 83]). They are based on numerical simulations of the Toner and Tu model [85],
59 which is a continuum analog of the Vicsek model [86]. Investigating appropriate geometrical
60 configurations (a sphere in [81], a network of rings in [82, 83]), they show that linearized
61 perturbations of the stationary state (i.e. sound waves) generate chiral edge states which
62 propagate uni-directionally, revealing an underpinning non-trivial topology. However, the
63 question of whether this effect could be realized with a finite (even large) number of discrete
64 particles and whether the topological states would survive the noise induced by this finite
65 particle number long enough is not investigated.

66 In this paper, we demonstrate the existence of non-trivial bulk topological states in a new
67 collective dynamics model. Bulk states propagate in the whole domain, by opposition to edge
68 states which are localized at the boundary. The collective dynamics model studied here has
69 first been proposed in [35] and later analyzed and expanded in [32, 37, 38]. Referred to below
70 as the "Body-Alignment Individual-Based Model" (BA-IBM or IBM for short), it describes
71 self-propelled rigid bodies moving with constant speed and trying to adjust their rigid body
72 attitude to that of their neighbors. In [37, 35] the BA-IBM was based on Stochastic Differ-
73 ential Equations (SDE) and a macroscopic model named the "Self-Organized Hydrodynamics
74 for Body-orientation (SOHB)" was derived. In [38, 32], SDE were replaced by Piecewise De-
75 terministic Markov Processes (PDMP) in the IBM but the macroscopic model remained the
76 SOHB model (with possibly different coefficients). In [32], a variant of the BA-IBM was shown

77 to exhibit phase transitions which were rigorously studied. In the present work, we derive ex-
 78 plicit solutions of the SOHB model which exhibit striking non-trivial topologies revealed by
 79 non-zero winding numbers. We explore how these non-trivial topologies are maintained at the
 80 level of the IBM by solving the PDMP of [38]. In particular, we observe that, due to noise
 81 induced by the finite particle number, topological phase transitions from states with non-
 82 trivial topology to states with trivial one may occur and we study these phase transitions in
 83 detail. Using a set of appropriately defined topological indicators, we reveal that the breakage
 84 of the non-trivial topology requires the system to go through a phase of maximal disorder.
 85 We also show that similar but topologically trivial initial conditions result in markedly dif-
 86 ferent dynamics, suggesting that topology plays a key role in the dynamics of this system.
 87 We are led to question the possible existence of topological protection against perturbations
 88 as mentioned above for topological insulators. Compared to previous works on topological
 89 states in collective dynamics, we deal with bulk states instead of edge states and we explore
 90 them at the level of the IBM and not just at the continuum level, which is closer to realistic
 91 particle systems. The present work adds a new item to the list of collective dynamics models
 92 exhibiting topological states. The topological protection concept could bring new perspectives
 93 to poorly understood questions such as the robustness of morphogenesis or the emergence of
 94 symmetries in growing organisms.

95 The present model belongs to the category of Vicsek-like models in the sense that it
 96 introduces a geometrical constraint within the degrees of freedom of the particles. In the
 97 Vicsek model, the particle velocities were constrained to belong to the unit sphere (after
 98 convenient normalization). In the present IBM, the particles carry an orthonormal frame,
 99 or equivalently, a rotation matrix, that describes their body attitude. Thus their degrees of
 100 freedom are constrained to belong to the manifold $SO_3(\mathbb{R})$ of 3×3 rotation matrices. Fig. 1
 101 highlights the difference between the Vicsek and body orientation models. The left picture
 102 shows alignment of two agents in the Vicsek sense, while the right picture shows alignment in
 103 the body-alignment sense. We mention that models involving full body attitudes have already
 104 been considered in [20, 59, 60, 61] in the context of flocking, but the alignment rules were
 105 different and essentially based on a velocity orientation (and not full body attitude) alignment.

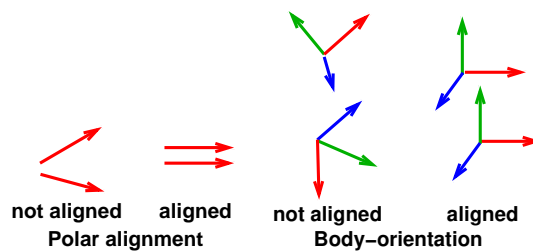


Figure 1: Vicsek model versus body-alignment model. Left: polar alignment of velocity orientations (red vectors) of two agents. Right: alignment of body-orientations: in addition to its velocity orientation (red), each agent has two other axes (green and blue), the three vectors forming a direct orthogonal frame.

106 We complete this introduction by a review of the mathematical literature on the Vicsek
 107 model and the BA-IBM. The mean-field limit of the IBM has been proven in [10] for the Vicsek
 108 model and in [43] for the body orientation model. Existence theory for the mean-field Vicsek
 109 model is available in [14, 48, 51] but the corresponding theory for the mean-field body ori-
 110 entation model is still open. The mean-field kinetic models exhibit phase transitions which have
 111 been studied in [33, 34, 49] and [32] for the Vicsek and body orientation models respectively.
 112 The numerical approximation of the mean-field kinetic model has been undertaken for the
 113 Vicsek model only in [50, 54]. The derivation of macroscopic equations from the mean-field
 114 Vicsek kinetic equations has first been formally achieved in [41] and later rigorously proved
 115 in [65]. Corresponding works for the body alignment model are only formal [35, 37, 38]. Ex-
 116 istence theory for the hydrodynamic models derived from the Vicsek model can be found in
 117 [40, 88] and numerical methods in [45, 50, 73]. Both questions are still open for the body
 118 orientation model.

119 The organization of this paper is as follows. Section 2 is devoted to the exposition of the
 120 IBM and macroscopic models. Then explicit solutions of the macroscopic model are derived
 121 in Section 3 and are shown to exhibit non-trivial topology. They also serve as benchmarks to
 122 show that the macroscopic model is an accurate approximation of the IBM. But after a some
 123 time, the IBM departs from the special solutions of the macroscopic model and undergoes a
 124 topological phase transition. The study of these phase transitions require appropriate topo-
 125 logical indicators which are developed in Section 4. Then, the topological phase transitions
 126 are analyzed in Section 5. A discussion and some open questions raised by these observations
 127 can be found in Section 6. The supplementary material (SM) collects additional informa-
 128 tion: a list of supplementary videos (Section SM1), a summary of the quaternion framework
 129 (Section SM2), a description of the numerical methods (Section SM3), a summary of the
 130 derivation of the macroscopic models (Section SM4) and finally a derivation of the explicit
 131 solutions presented in Section 3 (Section SM6).

132 2. Models.

133 2.1. The Individual-Based body-alignment Model.

134 **2.1.1. Description of the model.** In this section, we present the Individual-Based body-
 135 alignment Model (IBM). This model was first proposed in [38]. We consider N particles (or in-
 136 dividuals, or agents) indexed by $k \in \{1, \dots, N\}$ whose spatial locations are denoted by $\mathbf{X}_k(t) \in$
 137 \mathbb{R}^3 where $t \in [0, \infty)$ is the time. A direct orthonormal frame $\{\Omega_k(t), \mathbf{u}_k(t), \mathbf{v}_k(t)\}$ is attached
 138 to each particle (i.e. $\Omega_k, \mathbf{u}_k, \mathbf{v}_k \in \mathbb{S}^2$, $\Omega_k \cdot \mathbf{u}_k = 0$ and $\mathbf{v}_k = \Omega_k \times \mathbf{u}_k$). Likewise, if $(\mathbf{e}_1, \mathbf{e}_2, \mathbf{e}_3)$
 139 is a fixed direct orthonormal reference frame, we define $A_k(t)$ to be the unique element of the
 140 special orthonormal group $\text{SO}_3(\mathbb{R})$ which maps $(\mathbf{e}_1, \mathbf{e}_2, \mathbf{e}_3)$ onto $(\Omega_k(t), \mathbf{u}_k(t), \mathbf{v}_k(t))$. We will
 141 choose $(\mathbf{e}_1, \mathbf{e}_2, \mathbf{e}_3)$ once for all and write $A_k(t) = [\Omega_k(t), \mathbf{u}_k(t), \mathbf{v}_k(t)]$. This will be referred to
 142 as the local particle frame or as the particle's body orientation. $\Omega_k(t)$ is the self-propulsion
 143 direction: Particle k moves in straight line in the direction of Ω_k with unchanged local frame
 144 A_k except at exponentially distributed times at which the local frame jumps and adjusts itself
 145 to the average neighbors' local frame up to some noise. The motion of the particles is thus
 146 described by the functions $[0, \infty) \ni t \mapsto (\mathbf{X}_k(t), A_k(t)) \in \mathbb{R}^3 \times \text{SO}_3(\mathbb{R})$ for $k \in \{1, \dots, N\}$.

We first describe how the average neighbors' local frame is defined. We introduce a fixed

observation (or sensing) kernel $K: \mathbb{R}^3 \ni \mathbf{x} \mapsto K(\mathbf{x}) \in [0, \infty)$. We assume that K is a radial function (i.e. there exists $\tilde{K}: [0, \infty) \ni r \mapsto \tilde{K}(r) \in [0, \infty)$ such that $K(\mathbf{x}) = \tilde{K}(|\mathbf{x}|)$, where $|\mathbf{x}|$ is the euclidean norm of \mathbf{x}). For a collection of N particles $\{(\mathbf{X}_k, A_k)\}_{k \in \{1, \dots, N\}} \in (\mathbb{R}^3 \times \text{SO}_3(\mathbb{R}))^N$, we define the local flux as the following 3×3 matrix:

$$J_k = \frac{1}{N} \sum_{j=1}^N K(\mathbf{X}_k - \mathbf{X}_j) A_j.$$

147 Typically, we can think of $K(\mathbf{x})$ as the indicator function of the ball centered at zero with
 148 radius R . In this case, J_k is just the sum of the matrices A_j of all particles j located within
 149 a distance R to Particle k , divided by the total number of particles N . However, more
 150 sophisticated sensing functions can be used to account for the fact that e.g. distant particles
 151 will contribute to J_k less than neighboring particles. In general, J_k is not a rotation matrix.
 152 To recover a rotation matrix, we need to map J_k back onto the manifold $\text{SO}_3(\mathbb{R})$. To do so,
 153 the space $\mathcal{M}_3(\mathbb{R})$ of 3×3 matrices, is equipped with the inner product:

$$154 \quad (2.1) \quad A \cdot B := \frac{1}{2} \text{Tr}(A^T B),$$

155 where Tr denotes the trace operator and A^T is the transpose of the matrix A . Now, we define
 156 the average neighbors' local frame \mathbb{A}_k of Particle k as follows:

$$157 \quad (2.2) \quad \mathbb{A}_k := \arg \max_{A \in \text{SO}_3(\mathbb{R})} A \cdot J_k.$$

158 This expression stands for the element $\mathbb{A}_k \in \text{SO}_3(\mathbb{R})$ that maximizes the function $\text{SO}_3(\mathbb{R}) \ni$
 159 $A \mapsto A \cdot J_k \in \mathbb{R}$. The maximization procedure (2.2) has a unique solution as soon as J_k is not
 160 singular, i.e. $\det J_k \neq 0$ where \det stands for the determinant. Since the singular matrices
 161 form a zero-measure set in $\mathcal{M}_3(\mathbb{R})$ it is legitimate to assume that, except for a zero-measure
 162 set of initial data, this situation will not occur. Furthermore, when $\det J_k > 0$, \mathbb{A}_k is nothing
 163 but the unique rotation matrix involved in the polar decomposition of J_k .

164 We let the particles evolve according to the following Piecewise Deterministic Markov
 165 Process (PDMP).

- 166 • To each agent $k \in \{1, \dots, N\}$ is attached an increasing sequence of random times
 167 (jump times) T_k^1, T_k^2, \dots such that the intervals between two successive times are in-
 168 dependent and follow an exponential law with constant parameter $\nu > 0$ (Poisson
 169 process). At each jump time T_k^n , the function \mathbf{X}_k is continuous and the function A_k
 170 has a discontinuity between its left and right states respectively denoted by $A_k(T_k^n - 0)$
 171 and $A_k(T_k^n + 0)$.
- 172 • Between two jump times (T_k^n, T_k^{n+1}) , the evolution is deterministic: the orientation of
 173 Agent k does not change and it moves in straight line at speed $c_0 > 0$ in the direction
 174 $A_k(T_k^n + 0) \mathbf{e}_1$, i.e. for all $t \in [T_k^n, T_k^{n+1})$, we have

$$175 \quad (2.3) \quad \mathbf{X}_k(t) = \mathbf{X}_k(T_k^n) + c_0 (t - T_k^n) A_k(t) \mathbf{e}_1, \quad A_k(t) = A_k(T_k^n + 0).$$

- 176 • To compute $A_k(T_k^n + 0)$ from $A_k(T_k^n - 0)$, we compute the local flux defined at time
177 $T_k^n - 0$ given by:

$$178 \quad (2.4) \quad J_k^{n-} := \frac{1}{N} \sum_{j=1}^N K(\mathbf{X}_k(T_k^n) - \mathbf{X}_j(T_k^n)) A_j(T_k^n - 0),$$

179 having in mind that $A_j(T_k^n - 0) = A_j(T_k^n)$ for $j \neq k$. From J_k^{n-} , which we assume
180 is a non-singular matrix, we compute \mathbb{A}_k^n as the unique solution of the maximization
181 problem (2.2) (with J_k replaced by J_k^{n-}). Then, $A_k(T_k^n + 0)$ is drawn from a von Mises
182 distribution:

$$183 \quad (2.5) \quad A_k(T_k^n + 0) \sim M_{\mathbb{A}_k^n}.$$

184 The von Mises distribution on $\text{SO}_3(\mathbb{R})$ with parameter $\mathbb{A} \in \text{SO}_3(\mathbb{R})$ is defined to be
185 the probability density function:

$$186 \quad (2.6) \quad M_{\mathbb{A}}(A) := \frac{e^{\kappa \mathbb{A} \cdot A}}{\int_{\text{SO}_3(\mathbb{R})} e^{\kappa \mathbb{A} \cdot A'} dA'},$$

187 where $\kappa > 0$ is a supposed given parameter named concentration parameter, or inverse
188 of the noise intensity. The von Mises distribution, also known in the literature as the
189 matrix Fisher distribution [66, 70], is an analog (in the case of $\text{SO}_3(\mathbb{R})$) of the Gaussian
190 distribution in a flat space. The new orientation of Agent k at time T_n can therefore
191 be interpreted as a small random perturbation of the average local orientation given
192 by \mathbb{A}_k^n , where the perturbation size is measured by $1/\sqrt{\kappa}$.

193 In Formula (2.6) and in the remainder of this paper, the manifold $\text{SO}_3(\mathbb{R})$ is endowed with
194 its unique normalized Haar measure defined for any test function φ by:

$$195 \quad (2.7) \quad \int_{\text{SO}_3(\mathbb{R})} \varphi(A) dA := \frac{2}{\pi} \int_0^\pi \int_{\mathbb{S}^2} \varphi(\mathcal{A}(\theta, \mathbf{n})) \sin^2(\theta/2) d\theta d\mathbf{n},$$

196 where $d\mathbf{n}$ is the uniform probability measure on the sphere \mathbb{S}^2 . Here, a rotation matrix
197 $A \equiv \mathcal{A}(\theta, \mathbf{n})$ is parametrized by its rotation angle $\theta \in [0, \pi]$ and its axis $\mathbf{n} \in \mathbb{S}^2$ through
198 Rodrigues' formula:

$$199 \quad (2.8) \quad \mathcal{A}(\theta, \mathbf{n}) := I_3 + \sin \theta [\mathbf{n}]_{\times} + (1 - \cos \theta) [\mathbf{n}]_{\times}^2 = \exp(\theta [\mathbf{n}]_{\times})$$

200 with $\mathbf{n} = (n_1, n_2, n_3)^T$ and I_3 is the 3×3 identity matrix. For any vector $\mathbf{w} = (w_1, w_2, w_3)^T \in$
201 \mathbb{R}^3 , $[\mathbf{w}]_{\times}$ is the antisymmetric matrix of the linear map $\mathbb{R}^3 \ni \mathbf{u} \mapsto \mathbf{w} \times \mathbf{u}$ (where \times denotes the
202 cross product) which has the following expression:

$$203 \quad (2.9) \quad [\mathbf{w}]_{\times} := \begin{pmatrix} 0 & -w_3 & w_2 \\ w_3 & 0 & -w_1 \\ -w_2 & w_1 & 0 \end{pmatrix}.$$

204 Additional details on the structure of $\text{SO}_3(\mathbb{R})$ can be found for instance in [64]. The IBM
205 (2.3), (2.5) is schematically represented in Fig. 2.

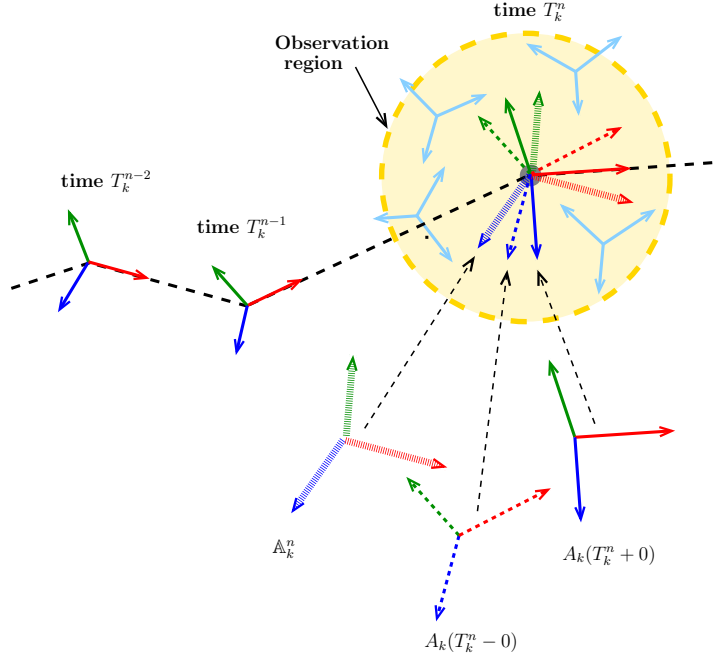


Figure 2: Schematic representation of the PDMP described in the text: the motion of Particle k is represented in physical space as the black broken dotted line. The body frame A_k is represented with Ω_k in red, \mathbf{u}_k in green and \mathbf{v}_k in blue. Each angular point of the trajectory corresponds to one of the jump times T_k^n . Between two jump times, the trajectory is the straight line spanned by Ω_k and the body frame stays constant. The jump dynamics is depicted at time T_k^n . At this time, the observation region is colored in yellow and body frames of the other particles present in this region are depicted in light blue. The averaged body frame \mathbb{A}_k^n is depicted with thick lightly colored arrows. The body frame before the jump $A_k(T_k^n - 0)$ is drawn in broken lines whereas that after the jump $A_k(T_k^n + 0)$ is drawn in plain lines. $A_k(T_k^n + 0)$ is close, but not equal to \mathbb{A}_k^n because of the noise intensity proportional to $1/\kappa$. For clarity, the frames involved in the description of the jump are magnified.

206 **2.1.2. Numerical simulations of the IBM.** Unless otherwise specified, throughout this
 207 paper, a square box of side length L with periodic boundary conditions is used. As sensing
 208 kernel K , we use the indicator function of the ball centered at 0 and of radius R . Thus, an
 209 agent interacts with all its neighbors at a distance less than R (radius of interaction). Table 1
 210 summarizes the model parameters.

211 For the numerical simulations presented in this paper, we have used the convenient frame-
 212 work offered by quaternions. Indeed, there is a group isomorphism between $\text{SO}_3(\mathbb{R})$ and
 213 $\mathbb{H}/\{\pm 1\}$ where \mathbb{H} is the group of unit quaternions. We can express the IBM (2.3), (2.5)
 214 using this representation (see [38] and Section SM2). Roughly speaking, body-alignment as
 215 described here is equivalent to nematic alignment of the corresponding quaternions (nematic

Parameter	Symbol
Number of particles	N
Computational box side length	L
Interaction radius	R
Particle speed	c_0
Concentration parameter	κ
Alignment frequency	ν

Table 1: Parameters of the IBM (2.3), (2.5).

216 alignment of a unit quaternions \mathbf{q} to the mean direction \mathbf{Q} is unchanged if \mathbf{q} is replaced by
 217 $-\mathbf{q}$, as opposed to polar alignment where the result depends on the sign of \mathbf{q}). This is because
 218 a given rotation can be represented by two opposite quaternions and thus, the outcome of
 219 the alignment process should not depend of the choice of this representative. The numerical
 220 algorithm is described in Section SM3. Additionally, the quaternion framework also suggests
 221 to use order parameters derived from nematic alignment dynamics (such as in liquid crystal
 222 polymers). We shall use this analogy to define appropriate order parameters in Section 4.1.

223 All the simulations were written in Python using the SiSyPHE library [44] specifically
 224 developed for the simulation of large-scale mean-field particle systems by the second author.
 225 The implementation is based on the PyTorch [77] library and more specifically on the GPU
 226 routines introduced by the KeOps [22] library. The computational details as well as the
 227 source code are freely available on the documentation website [https://sisyphe.readthedocs.](https://sisyphe.readthedocs.io/)
 228 [io/](https://sisyphe.readthedocs.io/). The outcomes of the simulations were analyzed and plotted using the NumPy [57] and
 229 Matplotlib [63] libraries. The 3D particle plots were produced using VPython [80]. All the
 230 particle simulations have been run on a GPU cluster at Imperial College London using an
 231 Nvidia GTX 2080 Ti GPU chip.

232 A typical outcome of the IBM is shown in Figure 3 (see also Section SM1, Video 1) for
 233 a moderate number of particles ($N = 3000$). Throughout this paper, in the plots, we will
 234 represent each agent graphically by an elongated tetrahedron pointing in the direction of
 235 motion. The three large faces around the height will be painted in blue, green and magenta
 236 and the base will be in gold, as described in Fig. 3a. We notice that, starting from a uniformly
 237 random initial state (Fig. 3b), the system self-organizes in small clusters (Fig. 3c) and finally
 238 reaches a flocking equilibrium where all the agents have roughly the same body-orientation
 239 (Fig. 3d). We will see below that flocking is not necessarily the ultimate fate of the system,
 240 because it may be trapped in a so-called topologically protected state. To better understand
 241 these aspects, we first need to develop the continuum (or macroscopic) description of the
 242 system. This is done in the next section.

243 **2.1.3. Relation with other collective dynamics models.** We finally make a comparison
 244 with previous models. First, there is a version of the IBM where particles follow a stochastic
 245 differential equation (SDE) instead of a jump process [35, 37]. Both the current and previous
 246 models have the same hydrodynamic model as macroscopic limit (see forthcoming section).
 247 There are two reasons for us to prefer the jump process. First, its simulation is slightly easier

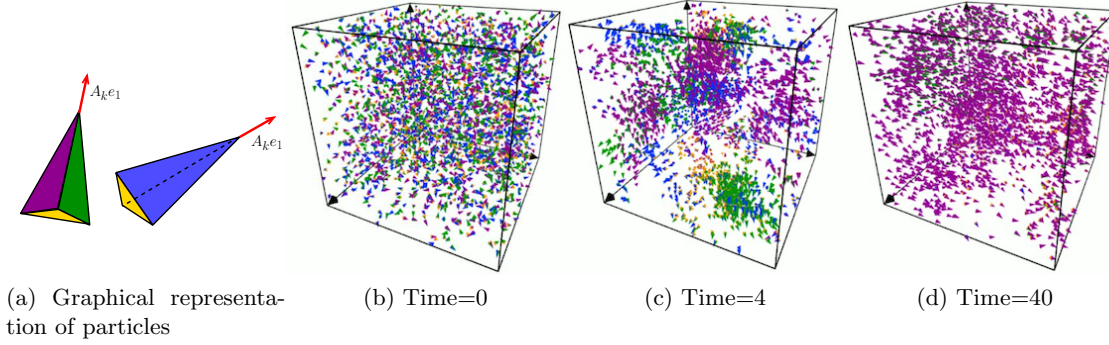


Figure 3: (a) Graphical representation of particles and their body orientations as elongated tetrahedra pointing towards the self-propulsion direction with blue, magenta and green large faces and gold bases. (b,c,d) Snapshots of a typical output of the simulation at three different times (b) Time=0, (c) Time=4 and (d) Time=40. Parameters: $N = 3000$, $L = 1$, $R = 0.075$, $\kappa = 20$, $\nu = 5$, $c_0 = 0.2$. see also Section SM1, Video 1.

248 and second, the coefficients of the macroscopic model are explicit, which is not so in the SDE
 249 case where they require the resolution of an auxiliary elliptic problem [35, 37].

250 Beyond the present body-orientation model, numerous models of self-propelled particles
 251 have been proposed in the literature (see the review [87]). The most closely related one is
 252 the celebrated Vicsek model [86]. There are several versions of this model: time-discrete
 253 ones [23, 86], time-continuous ones relying on an SDE description of the particle trajectories
 254 [41] and time-continuous ones using a jump process instead [45]. The latter version is the
 255 most closely related to the present work. In [45], the difference is that particles carry a
 256 single direction vector Ω_k instead of a whole body frame. This vector gives the direction of
 257 self-propulsion. The particles follow a similar PDMP, namely

- 258 • The random jump times are defined in the same way: they follow an exponential law
 259 with constant parameter $\nu > 0$. At jump times, the position is continuous and the
 260 direction vector Ω_k is discontinuous with left and right states respectively denoted by
 261 $\Omega_k(T_k^n - 0)$ and $\Omega_k(T_k^n + 0)$.
- 262 • Between two jump times T_k^n, T_k^{n+1} , the direction vector Ω_k does not change and the
 263 particle moves in straight line at speed $c_0 > 0$ in the direction given by $\Omega_k(T_k^n + 0)$.
- 264 • To pass from $\Omega_k(T_k^n - 0)$ to $\Omega_k(T_k^n + 0)$, we compute the local flux given by $\mathbf{J}_k^{n-} =$
 265 $\frac{1}{N} \sum_{j=1}^N K(\mathbf{X}_k(T_k^n) - \mathbf{X}_j(T_k^n)) \Omega_j(T_k^n - 0) \in \mathbb{R}^3$ and, assuming that it is non-zero,
 266 the mean direction $\bar{\Omega}_k^n = \mathbf{J}_k^{n-} / |\mathbf{J}_k^{n-}| \in \mathbb{S}^2$ at time $T_k^n - 0$. Then, $\Omega_k(T_k^n + 0)$ is
 267 drawn from a von Mises distribution on \mathbb{S}^2 : $\Omega_k(T_k^n + 0) \sim \tilde{M}_{\bar{\Omega}_k^n}$, with $M_{\bar{\Omega}}(\Omega) =$
 268 $e^{\kappa(\bar{\Omega} \cdot \Omega)} / \int_{\mathbb{S}^2} e^{\kappa(\bar{\Omega} \cdot \Omega)} d\Omega$, for Ω and $\bar{\Omega}$ in \mathbb{S}^2 .

269 So, the current model is an elaboration of [45] replacing self-propulsion directions by whole
 270 body frames and polar alignment of unit vectors (as expressed by the von Mises distribution
 271 on the sphere) by alignment of rotations matrices. Outcomes of numerical simulations of the

272 Vicsek model do not show striking differences whether one uses any of the above mentioned
 273 versions (time-discrete, time-continuous with SDE or time-continuous with jump process).
 274 Results given in [23, 86] for the time-discrete version display the emergence of a global align-
 275 ment together with the formation of clusters when the noise intensity $1/\kappa$ is not too big. The
 276 outcome strongly resembles what is shown in Fig. 3 for the body-orientation model, but for
 277 the depiction of the body orientation itself which is not provided by the Vicsek model. So,
 278 it is legitimate to wonder whether the inclusion of the full body orientation instead of the
 279 mere self-propulsion direction makes any change in the dynamics of the particle positions and
 280 direction vectors. In particular, do the particle positions and directions follow the same dy-
 281 namics in the Vicsek and body orientation model? We will see below that this is not the case
 282 and that in certain circumstances, striking differences between the two models are obtained.
 283 To show this, the use of the macroscopic limit of the IBM, as developed in the forthcoming
 284 section, will be of crucial importance.

285 2.2. The macroscopic body-alignment model.

286 **2.2.1. Description of the model.** As soon as N is not very small, the IBM (2.3), (2.5)
 287 involves a large number of unknowns which makes its mathematical analysis virtually impos-
 288 sible. A reduced description, more amenable to mathematical analysis, is obtained through
 289 the macroscopic limit of the IBM, and consists of a system of partial differential equations.
 290 This reduced description gives a valid approximation of the IBM in an appropriate range of
 291 parameters, namely

$$292 \quad (2.10) \quad N \gg 1, \quad \frac{R}{L} \sim \frac{c_0}{\nu L} \ll 1.$$

293 Throughout the remainder of this paper, we will focus on this regime. The macroscopic
 294 limit of the IBM (2.3), (2.5) has first been proposed in [38] and leads to a model called “Self-
 295 Organized Hydrodynamics for Body orientation (SOHB)”. The derivation relies on earlier work
 296 [35, 37]. This derivation is “formally rigorous” in the sense that, if appropriate smoothness
 297 assumptions are made on the involved mathematical objects, the limit model can be identified
 298 rigorously as being the SOHB. For the reader’s convenience, we summarize the main steps of
 299 this mathematical result in Section SM4.

300 The unknowns in the SOHB are the particle density $\rho(t, \mathbf{x})$ and mean body-orientation
 301 $\mathbb{A}(t, \mathbf{x}) \in \text{SO}_3(\mathbb{R})$ at time t and position $\mathbf{x} = (x, y, z) \in \mathbb{R}^3$. They satisfy the following set of
 302 equations:

$$303 \quad (2.11a) \quad \partial_t \rho + c_1 \nabla_{\mathbf{x}} \cdot (\rho \mathbb{A} \mathbf{e}_1) = 0,$$

$$304 \quad (2.11b) \quad (\partial_t + c_2 (\mathbb{A} \mathbf{e}_1 \cdot \nabla_{\mathbf{x}})) \mathbb{A} + [(\mathbb{A} \mathbf{e}_1) \times (c_3 \nabla_{\mathbf{x}} \log \rho + c_4 \mathbf{r}) + c_4 \delta \mathbb{A} \mathbf{e}_1]_{\times} \mathbb{A} = 0.$$

The quantities \mathbf{r} and δ have intrinsic expressions in terms of \mathbb{A} [35]. However, it is more
 convenient to write the rotation field \mathbb{A} in terms of the basis vectors

$$\Omega = \mathbb{A} \mathbf{e}_1, \quad \mathbf{u} = \mathbb{A} \mathbf{e}_2, \quad \mathbf{v} = \mathbb{A} \mathbf{e}_3.$$

306 With these notations, the vector $\mathbf{r}(t, \mathbf{x}) \in \mathbb{R}^3$ and scalar $\delta(t, \mathbf{x}) \in \mathbb{R}$ fields are defined by

$$307 \quad (2.12) \quad \mathbf{r} := (\nabla_{\mathbf{x}} \cdot \Omega) \Omega + (\nabla_{\mathbf{x}} \cdot \mathbf{u}) \mathbf{u} + (\nabla_{\mathbf{x}} \cdot \mathbf{v}) \mathbf{v},$$

$$308 \quad (2.13) \quad \delta := [(\Omega \cdot \nabla_{\mathbf{x}}) \mathbf{u}] \cdot \mathbf{v} + [(\mathbf{u} \cdot \nabla_{\mathbf{x}}) \mathbf{v}] \cdot \Omega + [(\mathbf{v} \cdot \nabla_{\mathbf{x}}) \Omega] \cdot \mathbf{u}.$$

309 Here, for a vector field $\mathbf{B}(\mathbf{x}) \in \mathbb{R}^3$ and a scalar field $\lambda(\mathbf{x}) \in \mathbb{R}$ we denote by $\nabla_{\mathbf{x}} \cdot \mathbf{B}$, and
 310 $\nabla_{\mathbf{x}} \times \mathbf{B}$ the divergence and curl of \mathbf{B} respectively, by $\nabla_{\mathbf{x}} \lambda$, the gradient of λ and we set
 311 $(\mathbf{B} \cdot \nabla_{\mathbf{x}}) \lambda = \mathbf{B} \cdot \nabla_{\mathbf{x}} \lambda$ with \cdot the inner product of vectors in \mathbb{R}^3 . We remind that \times denotes the
 312 cross product and we refer to formula (2.9) for the definition of $[\mathbf{w}]_{\times}$ when \mathbf{w} is a vector in
 313 \mathbb{R}^3 . Alternate expressions of δ can be found in Section SM5 of the Supplementary Material.

314 The quantities c_1, c_2, c_3, c_4 are functions of κ and c_0 given as follows:

$$315 \quad (2.14) \quad \frac{c_1}{c_0} = \frac{2}{3} \left\langle \frac{1}{2} + \cos \theta \right\rangle_{\exp(\kappa(\frac{1}{2} + \cos \theta)) \sin^2(\frac{\theta}{2})},$$

$$316 \quad (2.15) \quad \frac{c_2}{c_0} = \frac{1}{5} \left\langle 2 + 3 \cos \theta \right\rangle_{\exp(\kappa(\frac{1}{2} + \cos \theta)) \sin^4(\frac{\theta}{2}) \cos^2(\frac{\theta}{2})},$$

$$317 \quad (2.16) \quad \frac{c_3}{c_0} = \frac{1}{\kappa},$$

$$318 \quad (2.17) \quad \frac{c_4}{c_0} = \frac{1}{5} \left\langle 1 - \cos \theta \right\rangle_{\exp(\kappa(\frac{1}{2} + \cos \theta)) \sin^4(\frac{\theta}{2}) \cos^2(\frac{\theta}{2})},$$

319 where, for two functions f and $g: [0, \pi] \rightarrow \mathbb{R}$, we write

$$\langle f \rangle_g = \frac{\int_0^\pi f(\theta) g(\theta) d\theta}{\int_0^\pi g(\theta) d\theta}.$$

320 Fig. 4 provides a graphical representation of these functions.

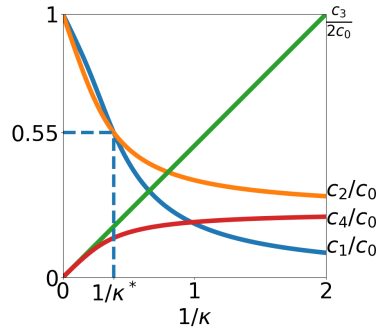


Figure 4: Dimensionless coefficients c_i/c_0 as functions of the inverse of concentration parameter $1/\kappa$. Blue curve c_1/c_0 , orange curve c_2/c_0 , green curve $c_3/2c_0$ and red curve c_4/c_0 . At the crossover value $\kappa^* \simeq 2.58$, the sign of $c_2 - c_1$ changes (see Section 3.2).

321 **2.2.2. Interpretation of the model.** To better understand what the SOHB system (2.11)
 322 does, we re-write it as follows:

$$323 \quad (2.18a) \quad \partial_t \rho + c_1 \nabla_{\mathbf{x}} \cdot (\rho \Omega) = 0,$$

$$324 \quad (2.18b) \quad D_t \mathbb{A} + [\mathbf{w}]_{\times} \mathbb{A} = 0,$$

325 where the convective derivative D_t and the vector \mathbf{w} are given by:

$$326 \quad (2.19) \quad D_t = \partial_t + c_2 \Omega \cdot \nabla_{\mathbf{x}},$$

$$327 \quad (2.20) \quad \mathbf{w} = -\Omega \times \mathbf{F} + c_4 \delta \Omega, \quad \text{with} \quad \mathbf{F} = -c_3 \nabla_{\mathbf{x}} \log \rho - c_4 \mathbf{r},$$

328
 329

Eq. (2.18a) is the mass conservation equation of the fluid. The vector Ω gives the direction of the fluid motion. The fluid velocity deduced from (2.18a) is $c_1\Omega$. Since $c_1/c_0 \in [0, 1]$ as can be seen from Fig. 4 (see also [35] for a rigorous proof), the fluid motion is oriented positively along Ω and its magnitude is smaller than the particles self-propulsion velocity c_0 . This is because the average of vectors of identical norms has smaller norm. The quantity c_1/c_0 can be seen as an order parameter [32] but we will not dwell on this issue here.

Eq. (2.18b) provides the rate of change of \mathbb{A} with time along the integral curves of the vector field $c_2\Omega$ as expressed by the convective derivative D_t . Note that this vector field is not the fluid velocity $c_1\Omega$ since $c_2 \neq c_1$. It can be interpreted as the propagation velocity of \mathbb{A} when \mathbf{w} is zero. Since $D_t\mathbb{A}$ is the derivative of an element of $\text{SO}_3(\mathbb{R})$, it must lie in the tangent space to $\text{SO}_3(\mathbb{R})$ at \mathbb{A} which consists of all matrices of the form $\mathbb{W}\mathbb{A}$ with \mathbb{W} antisymmetric. This structure is indeed satisfied by Eq. (2.18b) since, from the definition (2.9), the matrix $[\mathbf{w}]_{\times}$ is antisymmetric. It can be shown that the SOHB system is hyperbolic [36].

In fact, Eq. (2.18b) shows that the vector \mathbf{w} is the instantaneous rotation vector of the frame $\mathbb{A}(t, \mathbf{X}(t))$, where $t \mapsto \mathbf{X}(t)$ is any solution of $\frac{d\mathbf{X}}{dt} = c_2\Omega(t, \mathbf{X}(t))$. Indeed, Eq. (2.18b) can be equivalently written as a system of equations for $(\Omega, \mathbf{u}, \mathbf{v})$ of the form $D_t\mathbf{Z} = \mathbf{w} \times \mathbf{Z}$, with $\mathbf{Z} = \Omega, \mathbf{u}, \mathbf{v}$. This describes a rigid body rotation of the frame $\{\Omega, \mathbf{u}, \mathbf{v}\}$ with angular velocity \mathbf{w} . The rotation vector \mathbf{w} has two components. The first one is $\Omega \times \mathbf{F}$ and tends to relax Ω towards \mathbf{F} . Due to its expression (2.20), the force \mathbf{F} includes two contributions: that of the pressure gradient $-c_3\nabla_{\mathbf{x}} \log \rho$ and that of gradients of the body orientation through the vector $-c_4\mathbf{r}$. The second component of the rotation vector is $-c_4\delta\Omega$ and corresponds to a rotation of the body frame about the self propulsion direction Ω driven by gradients of the body orientation through the scalar $-c_4\delta$. The contributions of gradients of body orientation in the two components of the rotation vector are under the control of the single coefficient c_4 . Fig. 5 gives a graphical representation of the actions of these two infinitesimal rotations.

2.2.3. Relation with other models. To better understand how the SOHB model (2.11) relates to other models, we re-write the equation for Ω as follows:

$$(2.21) \quad D_t\Omega = P_{\Omega^\perp}\mathbf{F},$$

where P_{Ω^\perp} is the 3×3 projection matrix on the orthogonal plane to the vector Ω and is written $P_{\Omega^\perp} = I_3 - \Omega \otimes \Omega$ with \otimes standing for the tensor (or outer) product. Eq. (2.21) bears similarities and differences with the momentum equation of isothermal compressible fluids. The latter is exactly recovered if the following three modifications are made:

1. the projection matrix P_{Ω^\perp} is removed from (2.21) (i.e. it is replaced by I_3);
2. $c_2 = c_1$ in the convective derivative D_t (see (2.19));
3. $c_4 = 0$ in the expression of \mathbf{F} (see (2.20)).

Indeed, under these three modifications, we get the following system for (ρ, \mathbf{U}) where $\mathbf{U} = c_1\Omega$ is the fluid velocity:

$$\partial_t\rho + \nabla_{\mathbf{x}} \cdot (\rho\mathbf{U}) = 0, \quad (\partial_t + \mathbf{U} \cdot \nabla_{\mathbf{x}})\mathbf{U} = -\Theta \nabla_{\mathbf{x}} \log \rho.$$

This is the isothermal compressible Euler equations with the fluid temperature $\Theta = c_1 c_3$.

We now investigate what consequences follow from undoing the above three modifications, one by one.

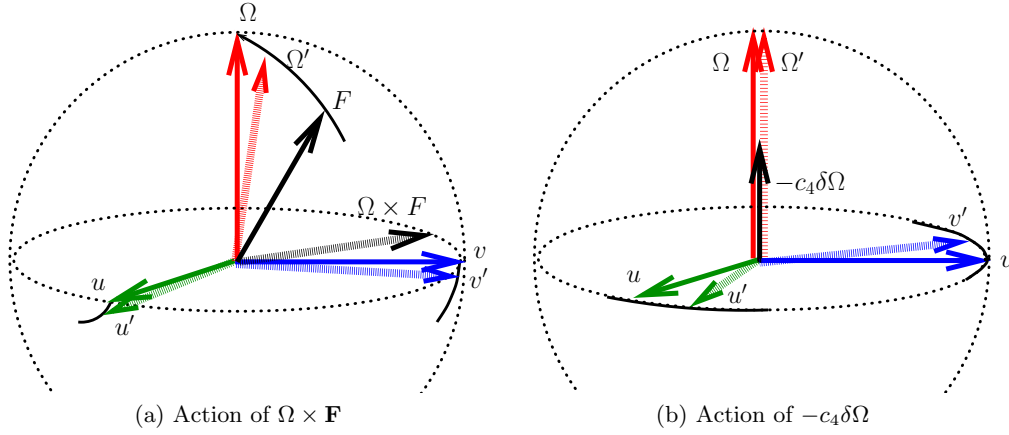


Figure 5: Graphical representations of the two components of the infinitesimal rotation. $(\Omega, \mathbf{u}, \mathbf{v})$ denotes the position of the frame at time t while $(\Omega', \mathbf{u}', \mathbf{v}')$ is its position at time $t + dt$ with $dt \ll 1$. The frame at time t is denoted in plain colors (red for Ω , green for \mathbf{u} and blue for \mathbf{v}) while that at time $t + dt$ is in light colors. The motion of the vectors is indicated by a segment of circle in black color. (a) Action of $\Omega \times \mathbf{F}$: the vectors \mathbf{F} and $\Omega \times \mathbf{F}$ are in plain and light black respectively. The vector \mathbf{F} is shown with unit norm for the ease of the representation but could be of any norm in reality. The passage from $(\Omega, \mathbf{u}, \mathbf{v})$ to $(\Omega', \mathbf{u}', \mathbf{v}')$ is via an infinitesimal rotation of axis $\Omega \times \mathbf{F}$. (b) Action of δ : the vector $-c_4 \delta \Omega$ is shown in black. The vectors Ω and Ω' are identical and collinear to $-c_4 \delta \Omega$. The passage from $(\Omega, \mathbf{u}, \mathbf{v})$ to $(\Omega', \mathbf{u}', \mathbf{v}')$ is via an infinitesimal rotation of axis Ω .

- 371 1. Introducing the projection P_{Ω^\perp} in (2.21) guarantees that the constraint $|\Omega| = 1$ is
 372 preserved in the course of time, if it is satisfied at time 0. Indeed, dotting Eq. (2.21)
 373 with Ω (and assuming that all functions are smooth) leads to $D_t |\Omega|^2 = 0$, which
 374 guarantees that $|\Omega|$ is constant along the integral curves of the vector field $c_2 \Omega$. Thus,
 375 if $|\Omega| = 1$ at time $t = 0$, it will stay so at any time.
 376 2. Having $c_2 \neq c_1$ is a signature of a loss of Galilean invariance. This is consistent with
 377 the fact that the microscopic system is not Galilean invariant as well, Indeed, there is
 378 a distinguished reference frame where the particle speed is c_0 . Of course, this speed
 379 does not remain equal to c_0 in frames that translate at constant speed with respect to
 380 this frame.

381 So far, with the introduction of P_{Ω^\perp} and different constants $c_2 \neq c_1$ but still with
 382 $c_4 = 0$, the system for (ρ, Ω) is decoupled from the equations for u and v and is
 383 written (see Eqs. (2.18a), (2.21) with \mathbf{F} given by (2.20) in which $c_4 = 0$):

384 (2.22a)
$$\partial_t \rho + c_1 \nabla_{\mathbf{x}} \cdot (\rho \Omega) = 0,$$

385 (2.22b)
$$D_t \Omega = -c_3 P_{\Omega^\perp} \nabla_{\mathbf{x}} \log \rho.$$

387 This is nothing but the hydrodynamic limit of the Vicsek particle model (known as
 388 ‘‘Self-Organized Hydrodynamics (SOH)’’) as established in [41, 45]. This system has

389 been shown to be hyperbolic [41] and to have local-in-time smooth solutions [40].
 390 3. When $c_4 \neq 0$, in addition to the pressure gradient, a second component of the force \mathbf{F}
 391 appears. This component depends on the full rotation matrix \mathbb{A} through Ω , \mathbf{u} , \mathbf{v} and
 392 their gradients (see Eq. 2.12). It is thus truly specific of the body orientation model.

393 We are now going to compare the IBM and the SOHB models on a set of explicit stationary
 394 solutions of the SOHB model described in the next section.

395 3. Special solutions of the macroscopic model.

396 **3.1. Three classes of explicit solutions.** In this section, we exhibit three different classes
 397 of global-in-time solutions of the SOHB model (2.18). They are special classes of a larger
 398 family of solutions which will also be introduced. All these solutions are characterized by
 399 uniform (i.e. independent of the spatial coordinate) fields ρ , \mathbf{r} and δ . From now on we fix a
 400 wave-number (inverse of the length) $\xi \in \mathbb{R} \setminus \{0\}$ and define

$$401 \quad (3.1) \quad \omega = \xi c_4, \quad \lambda = c_2 + c_4.$$

402 We denote by $\mathbf{x} = (x, y, z)^\top$ the coordinates of \mathbf{x} in the basis $(\mathbf{e}_1, \mathbf{e}_2, \mathbf{e}_3)$.

3.1.1. Flocking state. The flocking state (FS) is a trivial but important special solu-
 tion of the SOHB model (2.18) where both the density and rotation fields are constant (i.e.
 independent of time) and uniform:

$$\rho(t, \mathbf{x}) \equiv \rho_0 = \text{constant}, \quad \mathbb{A}(t, \mathbf{x}) \equiv \mathbb{A}_0 = \text{constant}, \quad \forall (t, \mathbf{x}) \in [0, \infty) \times \mathbb{R}^3.$$

403 **3.1.2. Milling orbits.** We have the following

404 **Lemma 3.1.** *The pair (ρ, \mathbb{A}) consisting of a constant and uniform density $\rho(t, \mathbf{x}) = \rho_0 =$
 405 constant and the following rotation field:*

$$406 \quad \mathbb{A}(t, \mathbf{x}) = \tilde{\mathbb{A}}_{\text{mill}}(t, z)$$

$$407 \quad (3.2) \quad = \begin{pmatrix} \cos(\omega t) & \sin(\omega t) \cos(\xi z) & -\sin(\omega t) \sin(\xi z) \\ -\sin(\omega t) & \cos(\omega t) \cos(\xi z) & -\cos(\omega t) \sin(\xi z) \\ 0 & \sin(\xi z) & \cos(\xi z) \end{pmatrix}$$

$$408 \quad (3.3) \quad = \mathcal{A}(-\omega t, \mathbf{e}_3) \mathcal{A}(\xi z, \mathbf{e}_1),$$

409 is a solution of the SOHB system (2.18), where ω and ξ are given by (3.1). We recall that
 410 $\mathcal{A}(\theta, \mathbf{n})$ is the rotation of axis $\mathbf{n} \in \mathbb{S}^2$ and angle $\theta \in \mathbb{R}$ defined by (2.8). This solution will be
 411 referred to as a milling orbit (MO).

412 The proof of this lemma is deferred to Section SM6. The MO is independent of x and y .
 413 Its initial condition is

$$414 \quad (3.4) \quad \mathbb{A}_{\text{mill}}(0, z) = \mathcal{A}(\xi z, \mathbf{e}_1) = \begin{pmatrix} 1 & 0 & 0 \\ 0 & \cos(\xi z) & -\sin(\xi z) \\ 0 & \sin(\xi z) & \cos(\xi z) \end{pmatrix}.$$

The initial direction of motion (the first column of $\mathbb{A}_{\text{mill}}(0, z)$) is independent of z and aligned
 along the x -direction, i.e. $\Omega(0, z) \equiv \mathbf{e}_1$. As z varies, the body-orientation rotates uniformly

about the x -direction with spatial angular frequency ξ . As the rotation vector is perpendicular to the direction of variation, (3.4) is called a “perpendicular twist”. As time evolves, the rotation field is obtained by multiplying on the left the initial perpendicular twist by the rotation $\mathcal{A}(-\omega t, \mathbf{e}_3)$. This means that the whole body frame undergoes a uniform rotation about the z -axis with angular velocity $-\omega$. As a consequence, the direction of motion is again independent of z . It belongs to the plane orthogonal to z and undergoes a uniform rotation about the z -axis. Consequently, the fluid streamlines, which are the integral curves of $c_1\Omega$, are circles contained in planes orthogonal to z of radius $\frac{c_1}{\omega} = \frac{c_1}{c_4} \frac{1}{\xi}$ traversed in the negative direction if $\xi > 0$. These closed circular streamlines motivate the “milling” terminology. It can be checked that the MO satisfies:

$$\mathbf{r} = \xi (\sin(\omega t), \cos(\omega t), 0)^T, \quad \delta = 0.$$

415 As announced, \mathbf{r} and δ are uniform but \mathbf{r} depends on time. Actually, $\Omega \times \mathbf{r} = \xi \mathbf{e}_3$ is inde-
 416 pendent of time. The MO is depicted in Fig. 6 and its dynamics is visualized in Video 2 (see
 417 Section SM1).

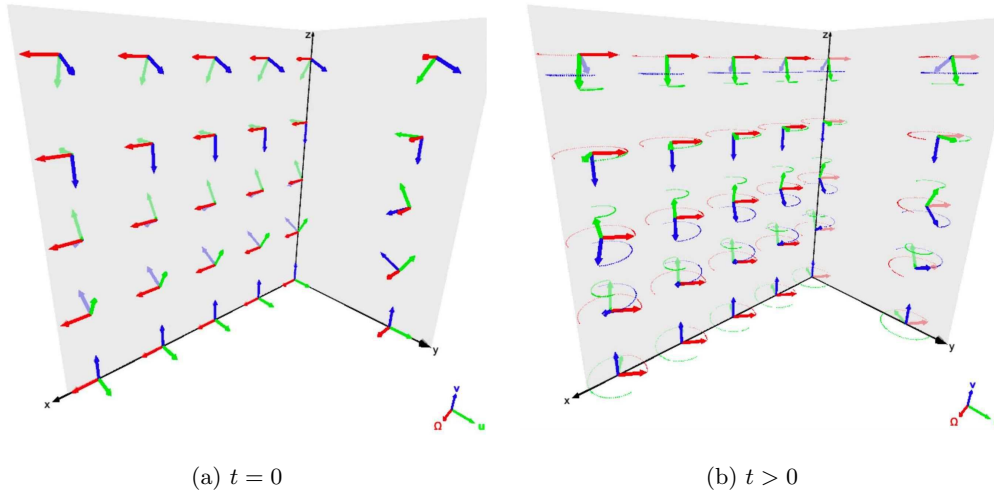


Figure 6: Graphical representation of the milling orbit (MO) at (a): initial time, and (b): time $t > 0$. The frame vectors Ω , \mathbf{u} and \mathbf{v} are represented at a certain number of points of the (O, x, y) and (O, y, z) planes. In (b), the rotation motion of the frame vectors is depicted by dotted circles of the color of the corresponding frame vector. The red dotted circle can be seen as a depiction of the fluid streamlines. See also Section SM1, Video 2.

418 Many examples of milling (also known as vortex) solutions have been observed in the
 419 collective dynamics literature as well as in biological systems [16, 25, 87]. On the modelling
 420 side, milling states have not been observed so far in alignment models without the inclusion of
 421 an additional process such as an attraction-repulsion force between the agents [17], a bounded
 422 cone of vision [24] or an anticipation mechanism [53]. The body-orientation framework is,
 423 to the best of our knowledge, a new situation in which milling can be observed just with

424 alignment assumptions. Milling states can also be found in physical systems. A typical and
 425 important example is the motion of a charged particle in a uniform magnetic field, resulting in
 426 the formation of so-called cyclotron orbits. Once again, in the body-orientation framework, an
 427 external field is not needed and self-induced cyclotron orbits emerge only from the variations
 428 of the internal body-orientation. Here, the analog of the magnetic field would be $\Omega \times \mathbf{r}$ and
 429 the cyclotron frequency would be ω . Note that ω is under the control of coefficient c_4 which
 430 depends on the noise intensity $1/\kappa$.

431 **3.1.3. Helical traveling wave.** We have the following

432 **Lemma 3.2.** *The pair (ρ, \mathbb{A}) consisting of a constant and uniform density $\rho(t, \mathbf{x}) = \rho_0 =$
 433 ρ_0 constant and the following rotation field:*

$$434 \quad \mathbb{A}(t, \mathbf{x}) = \tilde{\mathbb{A}}_{htw}(t, x)$$

$$435 \quad (3.5) \quad = \begin{pmatrix} 1 & 0 & 0 \\ 0 & \cos(\xi(x - \lambda t)) & -\sin(\xi(x - \lambda t)) \\ 0 & \sin(\xi(x - \lambda t)) & \cos(\xi(x - \lambda t)) \end{pmatrix}$$

$$436 \quad (3.6) \quad = \mathcal{A}(\xi(x - \lambda t), \mathbf{e}_1),$$

437 *is a solution of the SOHB system (2.18) where ξ and λ are defined by (3.1). This solution*
 438 *will be referred to as a helical traveling wave (HW).*

439 The proof of this lemma is given in Section SM6.2. The HW is independent of y and z .
 440 Its initial condition is

$$441 \quad (3.7) \quad \mathbb{A}_{htw}(0, x) = \mathcal{A}(\xi x, \mathbf{e}_1) = \begin{pmatrix} 1 & 0 & 0 \\ 0 & \cos(\xi x) & -\sin(\xi x) \\ 0 & \sin(\xi x) & \cos(\xi x) \end{pmatrix}.$$

Here the self-propulsion direction is still independent of x and equal to \mathbf{e}_1 . Also, the body orientation still rotates uniformly about \mathbf{e}_1 with spatial angular frequency ξ but when x is varied instead of z . This means that the body orientation is now twisted when varied along the propagation direction. So, this initial condition is called a “parallel twist”. In the HW, the self propulsion direction Ω remains constant in time and uniform in space. The initial twist is propagated in time in this direction at speed λ and gives rise to a traveling wave

$$\tilde{\mathbb{A}}_{htw}(t, x) = \tilde{\mathbb{A}}_{htw}(0, x - \lambda t).$$

Note that the traveling wave speed λ depends on the noise intensity $1/\kappa$ and is different from the fluid speed c_1 . So, the frame carried by a given fluid element followed in its motion is not fixed but rotates in time. Since Ω does not change, the fluid streamlines are now straight lines parallel to \mathbf{e}_1 . So, as a fluid element moves, the ends of the frame vectors \mathbf{u} and \mathbf{v} follow a helical trajectory with axis \mathbf{e}_1 , hence the terminology “helical traveling waves” for these solutions. It can be checked that

$$\mathbf{r} = 0, \quad \delta = \xi,$$

442 and again, \mathbf{r} and δ are spatially uniform as announced. The HW is depicted graphically in
 443 Fig. 7. Its dynamics is visualized in Video 3 (see Section SM1). The HW belongs to a larger
 444 class of solutions described in Section SM6.2.

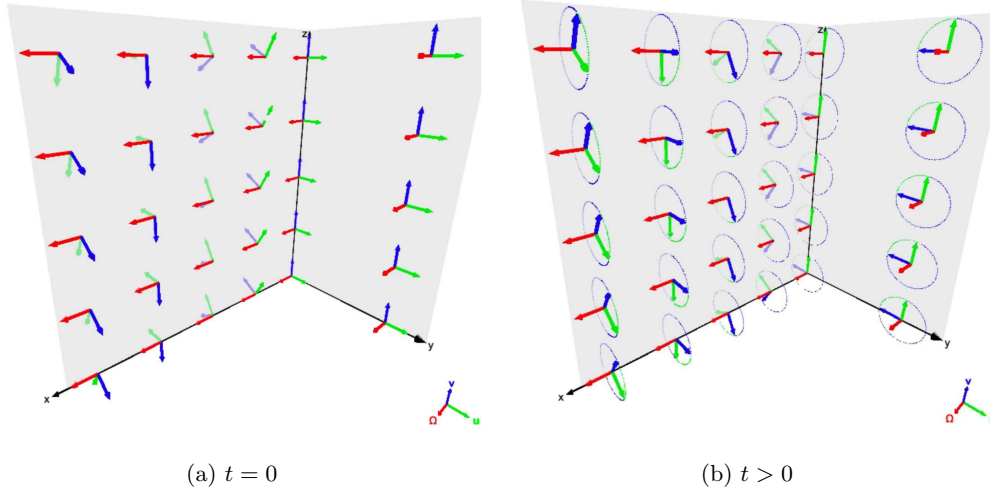


Figure 7: Graphical representation of the helical traveling wave (HW) at (a): initial time, and (b): time $t > 0$. See Fig. 6 for captions. See also Section SM1, Video 3.

445 **3.1.4. Generalized topological solutions.** The three above described classes of solutions
 446 can be encompassed by a single family of generalized solutions as stated in the following
 447 lemma.

448 **Lemma 3.3 (Generalized solutions).** Let $\xi \in \mathbb{R}$ and $\theta \in [0, \pi]$ be two parameters. Let $\omega \in \mathbb{R}$
 449 and $\tilde{\lambda} \in \mathbb{R}$ be defined by

$$450 \quad \omega = c_4 \xi, \quad \tilde{\lambda} = c_2 \cos \theta.$$

451 The pair (ρ, \mathbb{A}) consisting of a constant and uniform density $\rho(t, \mathbf{x}) = \rho_0 = \text{constant}$ and the
 452 following rotation field:

$$453 \quad (3.8) \quad \mathbb{A}(t, \mathbf{x}) = \mathbb{A}_{\xi, \theta}(t, z) := \mathcal{A}(-\omega t, \mathbf{e}_3) \mathcal{A}\left(\theta - \frac{\pi}{2}, \mathbf{e}_2\right) \mathcal{A}(\xi(z - \tilde{\lambda}t), \mathbf{e}_1),$$

454 is a solution of the SOHB system (2.18). We recall that $\mathcal{A}(\theta, \mathbf{n})$ is the rotation of axis $\mathbf{n} \in \mathbb{S}^2$
 455 and angle $\theta \in \mathbb{R}$. This solution will be referred to as a Generalized topological Solution (GS).

456 The proof of this lemma is deferred to the Supplementary Material SM6.3. Each of the
 457 three previous classes of solutions can be obtained for specific values of the parameters ξ and θ .

- 458 • When $\xi = 0$, the solution $\mathbb{A}_{0, \theta}$ is constant for any θ , which corresponds to a FS.
- 459 • When $\theta = \frac{\pi}{2}$ and $\xi \in \mathbb{R}$, then $\tilde{\lambda} = 0$ and the rotation with respect to the y -axis is
 460 equal to the identity: the solution $\mathbb{A}_{\xi, \pi/2}$ is therefore equal to the MO (3.3).
- 461 • When $\theta = 0$ and $\xi \in \mathbb{R}$ then $\tilde{\lambda} = c_2$ and the solution $\mathbb{A}_{\xi, 0}$ is equal to

$$462 \quad \mathbb{A}_{\xi, 0} = \begin{pmatrix} 0 & -\sin(\xi(z - \lambda t)) & -\cos(\xi(z - \lambda t)) \\ 0 & \cos(\xi(z - \lambda t)) & -\sin(\xi(z - \lambda t)) \\ 1 & 0 & 0 \end{pmatrix}, \quad \lambda = c_2 + c_4,$$

463 which is an HW along the z -axis. The situation is analogous when $\theta = \pi$.

464 All these solutions have a non-zero gradient in the body-orientation variable which is al-
 465 ways along the z -axis. This gradient is controlled by the parameter ξ . However, in the GS,
 466 the direction of motion Ω (or fluid velocity) is not necessarily parallel nor perpendicular to
 467 this gradient. Specifically, Ω has a constant polar angle equal to the parameter θ . The be-
 468 havior of the solution is then a combination of the two previously introduced phenomena:
 469 milling around the z -axis and a travelling wave of the body-orientation variable along the
 470 same axis. The applet accessible at [https://www.glowscript.org/#/user/AntoineDiez/folder/](https://www.glowscript.org/#/user/AntoineDiez/folder/MyPrograms/program/BOfield)
 471 [MyPrograms/program/BOfield](https://www.glowscript.org/#/user/AntoineDiez/folder/MyPrograms/program/BOfield) provides a graphical representation of the GS for arbitrary
 472 polar angles using VPython [80] and with the same conventions as in Fig. 6.

473 In the following, we will focus on each of these two elementary behaviors, i.e. the standard
 474 milling and helical travelling wave solutions, and in particular on their topological properties.
 475 The study of the full continuum of generalized solutions is left for future work. However, we
 476 will encounter GS obtained from a perturbed milling solution in Section 5.4.

477 **3.2. Some properties of these special solutions.** Clearly, in the definitions of the MO
 478 and HW, the choice of reference frame is unimportant. So, in the whole space \mathbb{R}^3 , such
 479 solutions exist in association with any reference frame. In a square domain of side-length L
 480 with periodic boundary conditions, periodicity imposes some constraints on the direction of
 481 the reference frame. For simplicity, we will only consider the case where the reference frame
 482 has parallel axes to the sides of the square and ξ is linked to L by an integrality condition
 483 $L\xi = 2\pi n$, with $n \in \mathbb{Z} \setminus \{0\}$.

484 The study of the stability of the MO and the HW is left for future work. By contrast, the
 485 FS is linearly stable as the SOHB system is hyperbolic [36]. However, there is no guarantee
 486 that the FS at the level of the IBM is stable. Indeed, there are strong indications that the FS
 487 is not stable for the Vicsek model [23] for some parameter ranges and a similar trend is likely
 488 to occur here.

489 We can now answer the question posed at the end of Section 2.1.3 namely whether the
 490 inclusion of the full body orientation makes any change in the dynamics of the particle positions
 491 and directions compared to the Vicsek model. To this end, we consider the corresponding
 492 macroscopic models, i.e. the SOH model (2.22) for the Vicsek model and the SOHB model
 493 (2.11) for the body-orientation dynamics. If we initialize the SOH model with uniform initial
 494 density ρ and mean direction Ω , inspection of (2.22) shows that the solution remains constant
 495 in time and thus corresponds to a flocking state of the Vicsek model. In the SOHB model,
 496 the three classes of solutions described in the previous sections (the FS, MO and HW) also
 497 have uniform initial density ρ and mean direction Ω . If the dynamics of the particle positions
 498 and directions in the body orientation model was the same as in the Vicsek model, these
 499 three classes of solutions should have a constant mean direction Ω . However, it is not the
 500 case for the MO, where Ω changes with time and is subject to a planar rotation. This means
 501 that gradients of body attitude do have a non-trivial influence on the direction of motion of
 502 the particles and that the body orientation model does not reduce to a Vicsek model for the
 503 particle positions and directions.

504 There is another, more subtle, difference between the two models concerning the dynamics
 505 of Ω . It does not concern the MO and HW but we discuss it here in relation with the previous
 506 paragraph. Indeed, Fig. 4 reveals that the velocities c_1 and c_2 for the SOHB model crossover

507 at a certain value κ^* of the concentration parameter. The coefficients c_1 and c_2 for the
 508 SOH model can be found in [45], Fig. A1(b) and appear to satisfy $c_1 > c_2$ for the whole
 509 range of values of κ , i.e. do not exhibit any crossover. In particular, at large noise, the
 510 propagation velocity c_2 of Ω in the SOHB model is larger than the mass transport velocity c_1 .
 511 This means that information (which triggers adjustments in Ω) propagates downstream the
 512 fluid by contrast to the Vicsek case where it propagates upstream. While the reason for this
 513 difference is unclear at this stage, we expect that it may induce large qualitative differences
 514 in the behavior of the system in some cases. This point will be investigated in future work.

515 Numerical simulation of the SOHB will be subject to future work. Here, we will restrict
 516 ourselves to the MO and HW for which we have analytical formulas. In the next section,
 517 using these two special solutions, we verify that the SOHB model and the IBM are close in
 518 an appropriate parameter range.

519 **3.3. Agreement between the models.** In this section we use the MO and HW to demon-
 520 strate the quantitative agreement between the SOHB model (2.11) and the IBM (2.3), (2.5)
 521 in the scaling (2.10). In the simulations below, we consider a periodic cube of side-length L
 522 and choose

$$523 \quad (3.9) \quad R = 0.025, \quad \nu = 40, \quad c_0 = 1, \quad L = 1, \quad \xi = 2\pi,$$

524 so that $\frac{R}{L} = \frac{c_0}{\nu L} = 0.025 \ll 1$, ensuring that the scaling (2.10) is satisfied. Furthermore, we
 525 see that the choice of ξ is such that the twists in the MO or HW have exactly one period over
 526 the domain size.

527 **3.3.1. The IBM converges to the macroscopic model as $N \rightarrow \infty$.** In this section, we
 528 numerically demonstrate that the solutions of the IBM converge to those of the macroscopic
 529 model in the limit $N \rightarrow \infty$ and investigate the behavior of the IBM at moderately high values
 530 of N .

We sample N particles according to the initial condition (3.4) of the MO and simulate
 the IBM (2.3), (2.5). We recall that the average direction $\Omega(t)$ of the exact MO (3.2) is
 spatially uniform at any time and undergoes a uniform rotation motion about the z -axis. So,
 we will compare $\Omega(t)$ with the average direction $\bar{\Omega}(t)$ of all the particles of the IBM, where
 $\bar{\Omega}(t) = (\bar{\Omega}^1, \bar{\Omega}^2, \bar{\Omega}^3)^T$ is defined by:

$$\bar{\Omega} = \frac{\sum_{k=1}^N \Omega_k(t)}{|\sum_{k=1}^N \Omega_k(t)|},$$

531 (provided the denominator is not zero, and where we recall that $\Omega_k(t) = A_k(t) \mathbf{e}_1$). To ease
 532 the comparison, we compute the azimuthal and polar angles of $\bar{\Omega}$ respectively defined by:

$$533 \quad (3.10) \quad \bar{\varphi} := \arg(\bar{\Omega}^1 + i\bar{\Omega}^2) \in [0, 2\pi), \quad \bar{\theta} = \arccos(\bar{\Omega}^3) \in [0, \pi],$$

534 where $\arg(x + iy)$ stands for the argument of the complex number $x + iy$. We note that the
 535 corresponding angles φ and θ of $\Omega(t)$ are given by

$$536 \quad (3.11) \quad \varphi(t) = -\omega t = -2\pi c_4(\kappa) t, \quad \theta = \pi/2,$$

537 where we have used (3.1) and (3.9) to compute the value of ω .

538 Fig. 8a shows the azimuthal angle $\bar{\varphi}$ as a function of time over 5 units of time, for increasing
 539 particle numbers: $N = 5 \cdot 10^4$ (green curve), $N = 1.5 \cdot 10^5$ (orange curve) and $N = 1.5 \cdot 10^6$ (blue
 540 curve). Note that for very small values of N , the macroscopic model loses its relevance:
 541 below a few thousand particles we only observe a noisy behavior, not shown in the figure.
 542 For the considered range of particle numbers, we notice that the angle $\bar{\varphi}$ decreases linearly
 543 with time, which shows that the behavior of the IBM is consistent with the exact solution
 544 (3.11). However, quantitatively, we see that $|\mathrm{d}\bar{\varphi}/\mathrm{d}t|$ depends on the particle number and
 545 decreases with increasing particle number. We investigate this behavior in more detail in
 546 Fig. 8b where the difference between the measured angular velocity $|\mathrm{d}\bar{\varphi}/\mathrm{d}t|$ and the theoretical
 547 prediction $2\pi c_4(\kappa)$ is plotted as a function of N . Each data point (blue dot) is an average
 548 of 10 independent simulations. This figure confirms that, as N increases, $|\mathrm{d}\bar{\varphi}/\mathrm{d}t|$ decreases
 549 and converges towards $2\pi c_4(\kappa)$. The inset in Fig. 8b shows the same data points in a log-
 550 log-scale with the associated regression line (orange solid line). We observe that the error
 551 between the measured and theoretical angular velocities behaves like $N^{-\alpha}$ with a measured
 552 exponent $\alpha \simeq 1.01$ which is close to the theoretical value $\alpha = 1$ derived in Section SM7 of the
 553 Supplementary Material.

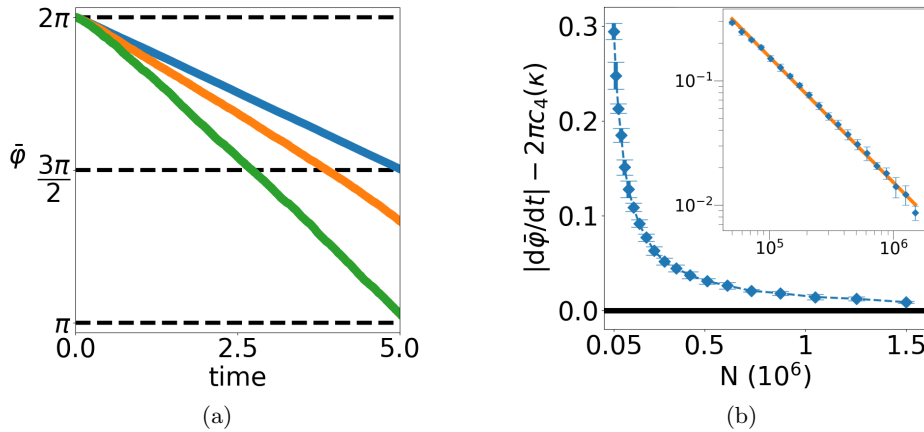


Figure 8: (a) Time evolution of the angle $\bar{\varphi}$ for three values of N : $N = 0.05 \cdot 10^6$ (green curve), $N = 0.15 \cdot 10^6$ (orange curve) and $N = 1.5 \cdot 10^6$ (blue curve). (b) Difference between the measured angular velocity $|\mathrm{d}\bar{\varphi}/\mathrm{d}t|$ and the theoretical value $2\pi c_4(\kappa)$. Each data point (blue dot) is an average of 10 independent simulations with the error bar showing one standard deviation. Solid black horizontal line at 0 for convenience. Inset: same data in log-log scale and regression line (solid orange line). Parameters: $L = 1$, $\xi = 2\pi$, $R = 0.025$, $\nu = 40$, $c_0 = 1$, $\kappa = 10$.

554 **3.3.2. Quantitative comparison between the models.** In order to quantitatively confirm
 555 the agreement between the IBM and the macroscopic model, we fix a large number $N = 1.5 \cdot 10^6$
 556 of particles and we run the IBM for different values of the concentration parameter κ and for

557 the two classes of special solutions, the MO and the HW. To compare the models, we compute
 558 the following macroscopic quantities:

- 559 • For the MO: starting from a sampling of the initial condition (3.4), we measure the
 560 angular velocity $|\mathrm{d}\bar{\varphi}/\mathrm{d}t|$ in a similar way as in the previous section. Given the param-
 561 eter choice (3.9), the theoretical value of $|\mathrm{d}\varphi/\mathrm{d}t|$ predicted by (3.2) is $|\omega| = 2\pi c_4(\kappa)$
 562 where the function c_4 is given by (2.17).
- 563 • For the HW, starting from a sampling of the initial condition (3.7), we measure the
 564 wave speed. To this aim, using (2.2), we compute the mean body-orientation \mathbb{A} of
 565 the agents in a slice of size 10^{-3} along the x -axis (which is the global direction of
 566 motion) as a function of time. As predicted by (3.5) the coefficient \mathbb{A}_{22} of the mean
 567 orientation is a periodic signal. The inverse of the period of this signal (obtained
 568 through a discrete Fourier transform) gives the traveling wave speed of the HW. The
 569 theoretical value predicted by (3.5) is given by $\lambda = c_2(\kappa) + c_4(\kappa)$ where the function
 570 c_2 is given by (2.15).

571 The output of these simulations is shown in Figs. 9a for the MO and 9b for the HW.
 572 They respectively display the angular velocity and traveling wave speed obtained by running
 573 the IBM for a discrete set of values of κ (big blue dots). By comparison, the black dotted
 574 curves show the theoretical values as functions of κ . For the parameters of Fig. 9, the order
 575 of magnitude of the standard deviation of 10 independent simulations is 10^{-3} . The relative
 576 error between the average measured value and its theoretical prediction varies between 2%
 577 and 5% on the whole range of concentration parameters considered.

578 These figures show an excellent agreement between the prediction of the macroscopic
 579 SOHB model and the results obtained by running the IBM when the number of particles is
 580 large. This confirms that the SOHB model provides an excellent approximation of the IBM,
 581 at least during a certain period of time which is a function of the particle number. We will see
 582 below that fluctuations induced by the finite number of particles may eventually destabilize
 583 the MO and lead to a HW or a FS. As these solutions are associated with different topological
 584 structure, these transitions will be analyzed as topological phase transitions in the forthcoming
 585 sections.

586 **3.4. Topology.** Both the MO and HW have non-trivial topology: inspecting the perpen-
 587 dicular twist (3.4) (see also Fig. 6a), we observe that the two-dimensional curve generated by
 588 the end of the vector \mathbf{u} in the (y, z) -plane as one moves along the z -axis is a closed circle. A
 589 similar observation can be made on the parallel twist (3.7) (see Fig. 7a) as one moves along
 590 the x -axis. Both curves have therefore non-zero winding numbers about the origin. When
 591 the domain is \mathbb{R}^3 , these winding numbers are $\pm\infty$ (where the sign corresponds to that of ξ)
 592 as these curves make an infinite number of turns. If the domain has finite extension L along
 593 the z -axis (in the MO case) or the x -axis (in the HW case) and, due to the periodic boundary
 594 conditions, L is related to ξ by $L = n 2\pi/\xi$ with $n \in \mathbb{Z} \setminus \{0\}$, then the winding numbers
 595 are equal to n . As observed on Formulas (3.2) and (3.5) (or on Figs 6b and 7b), this initial
 596 non-trivial topological structure is propagated in time.

597 When we initialize particles by sampling the initial conditions (3.4) or (3.7), we expect that
 598 the solution of the IBM remains an approximation of the MO (3.2) or HW (3.5) respectively
 599 as evidenced in Section 3.3.2. However, noise induced by both the inherent stochasticity of the

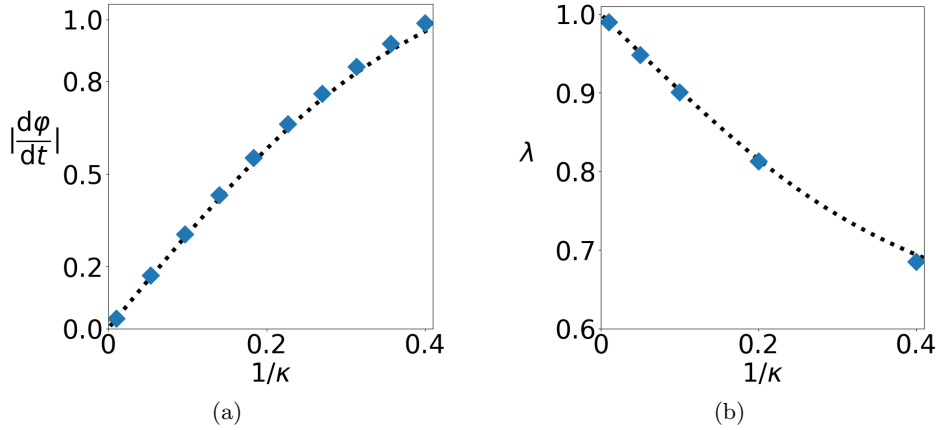


Figure 9: (a) MO: angular velocity $|\frac{d\varphi}{dt}|$ as a function of $1/\kappa$. (b) HW: traveling wave speed λ as a function of $1/\kappa$. Measured values from the IBM at discrete values of κ (big blue dots) and theoretical prediction from the SOHB model (dotted black curve). Parameters: $N = 1.5 \cdot 10^6$, $L = 1$, $\xi = 2\pi$, $R = 0.025$, $\nu = 40$, $c_0 = 1$.

600 IBM and finite particle number effects as explained in Section 3.3.1 may eventually destabilize
 601 the IBM. Then, in most cases, its solution is seen to transition towards an approximation of
 602 the FS after some time. This transition implies a change of the topology of the solution which,
 603 from initially non-trivial, becomes trivial, since the winding number of the FS is zero. One may
 604 wonder whether the evolution towards a FS is slower if the initial state has non-trivial topology
 605 and exhibits some kind of “topological protection” against noise-induced perturbations. To
 606 test this hypothesis quantitatively, we first need to develop appropriate indicators. This is
 607 done in the next section.

608 **4. Order parameters and topological indicators.** We will use two types of indicators.
 609 The first one is the global order parameter which will discriminate between the various types
 610 of organization of the system (disorder, MO or HW and FS). The second type of indicators
 611 are based on analyzing the roll angle. They will enable a finer characterization of topological
 612 phase transitions.

613 **4.1. Global order parameter.** We first introduce the following scalar binary order param-
 614 eter which measures the degree of alignment between two agents with body-orientations A ,
 615 $\tilde{A} \in \text{SO}_3(\mathbb{R})$:

$$616 \quad (4.1) \quad \psi(A, \tilde{A}) := \frac{1}{2} A \cdot \tilde{A} + \frac{1}{4}.$$

617 In the quaternion framework (see Section 2.1.2 and SM2 for details), we have

$$618 \quad (4.2) \quad \psi(A, \tilde{A}) = (q \cdot \tilde{q})^2,$$

619 where q and \tilde{q} are two unit quaternions respectively associated to A and \tilde{A} , and $q \cdot \tilde{q}$ indicates
 620 the inner product of two quaternions. This expression makes it clear that $\psi(A, \tilde{A}) \in [0, 1]$. The

621 square exponent in (4.2) indicates that $\psi(A, \tilde{A})$ measures the nematic alignment of the two
 622 associated unit quaternions, as it should because two opposite quaternions represent the same
 623 rotation. We note that $\psi(A, \tilde{A}) = 1$ if and only if $\tilde{A} = A$. On the other hand, $\psi(A, \tilde{A}) = 0$ if
 624 and only if $A \cdot \tilde{A} = -1/2$, which corresponds to the two rotation axes being orthogonal and
 625 one rotation being an inversion about its axis.

626 The Global Order Parameter (GOP) of a system of N agents at time $t > 0$ is the average
 627 of all binary order parameters over all pairs of particles:

$$628 \quad (4.3) \quad \text{GOP}^N(t) = \frac{1}{N(N-1)} \sum_{k \neq \ell} \psi(A_k(t), A_\ell(t)).$$

629 From (4.3) we have $\text{GOP}^N(t) \in [0, 1]$. A small GOP^N indicates large disorder and a large
 630 one, strong alignment. This is a global measure of alignment, by contrast to a local one where
 631 ψ would be averaged over its neighbors only (and the result, averaged over all the particles).
 632 This global measure of alignment allows us to separate the MO and HW from the FS as shown
 633 below, which would not be possible with a local one.

The GOP (4.3) can also be defined at the continuum level. As shown in Section SM4,
 in the macroscopic limit, the particles become independent and identically distributed over
 $\mathbb{R}^3 \times \text{SO}_3(\mathbb{R})$, with common distribution $\rho M_{\mathbb{A}}$ where (ρ, \mathbb{A}) satisfies the SOHB system (2.11)
 and $M_{\mathbb{A}}$ is the von Mises distribution (2.6). Therefore, the GOP of a solution of the SOHB
 system (ρ, \mathbb{A}) is obtained as (4.3) where the sum is replaced by an integral, $A_k(t)$ is replaced
 by A distributed according to the measure $(\rho M_{\mathbb{A}})(t, \mathbf{x}, A) d\mathbf{x} dA$ and $A_\ell(t)$ is replaced by \tilde{A}
 distributed according to the same measure, but independently to A . Therefore,

$$\text{GOP}(\rho, \mathbb{A}) := \iint_{(\mathbb{R}^3 \times \text{SO}_3(\mathbb{R}))^2} \psi(A, \tilde{A}) \rho(\mathbf{x}) \rho(\tilde{\mathbf{x}}) M_{\mathbb{A}(\mathbf{x})}(A) M_{\mathbb{A}(\tilde{\mathbf{x}})}(\tilde{A}) d\mathbf{x} d\tilde{\mathbf{x}} dA d\tilde{A}.$$

634 Using (2.7) and (2.8) one can prove that for any $\mathbb{A} \in \text{SO}_3(\mathbb{R})$, we have

$$635 \quad (4.4) \quad \int_{\text{SO}_3(\mathbb{R})} A M_{\mathbb{A}}(A) dA = \frac{c_1(\kappa)}{c_0} \mathbb{A},$$

636 with $c_1(\kappa)$ defined by (2.14) and c_0 being the particle speed. Using (4.1), we obtain:

$$637 \quad (4.5) \quad \text{GOP}(\rho, \mathbb{A}) = \frac{1}{2} \left(\frac{c_1(\kappa)}{c_0} \right)^2 \int_{\mathbb{R}^3 \times \mathbb{R}^3} \mathbb{A}(\mathbf{x}) \cdot \mathbb{A}(\tilde{\mathbf{x}}) \rho(\mathbf{x}) \rho(\tilde{\mathbf{x}}) d\mathbf{x} d\tilde{\mathbf{x}} + \frac{1}{4}.$$

638 From now on, we let ρ be the uniform distribution on a square box of side-length L . We
 639 can compute the GOP corresponding to each of the three solutions defined in Section 3.1.
 640 For the MO (3.2), HW (3.5) and GS (3.8), for all time $t > 0$, in all cases, the GOP remains
 641 equal to:

$$642 \quad (4.6) \quad \text{GOP}_1 = \frac{1}{4} \left(\frac{c_1(\kappa)}{c_0} \right)^2 + \frac{1}{4}.$$

643 For the FS, $\mathbb{A}(\mathbf{x}) \equiv \mathbb{A} = \text{constant}$ and the GOP is equal to

$$644 \quad (4.7) \quad \text{GOP}_2 = \frac{3}{4} \left(\frac{c_1(\kappa)}{c_0} \right)^2 + \frac{1}{4}.$$

645 Note that the GOP:

$$646 \quad \text{GOP}_0 = \frac{1}{4},$$

647 corresponds to a disordered state of the IBM where the body-orientations of the particles are
648 chosen independently and randomly uniformly (or equivalently to the SOHB case $\kappa \rightarrow 0$ in
649 (4.6) and (4.7)). For the typical value $\kappa = 10$ used in our simulations, one can compute that:

$$650 \quad (4.8) \quad \text{GOP}_1 \simeq 0.45, \quad \text{GOP}_2 \simeq 0.85.$$

651 The GOP values between GOP_1 and GOP_2 can be reached by generalized HW as shown in
652 Section SM6.4.

653 4.2. Roll angle.

4.2.1. Definition. Let $A = [\Omega, \mathbf{u}, \mathbf{v}] \in \text{SO}_3(\mathbb{R})$ be a body-orientation. Let $\theta \in [0, \pi]$,
 $\varphi \in [0, 2\pi)$ be the spherical coordinates of Ω defined by (3.10) (omitting the bars). We let
 $\{\Omega, \mathbf{e}_\theta, \mathbf{e}_\varphi\}$ be the local orthonormal frame associated with the spherical coordinates (θ, φ)
and we define $\mathbf{p}(\Omega) = \mathbf{e}_\varphi$ and $\mathbf{q}(\Omega) = -\mathbf{e}_\theta$. Then we define the rotation matrix

$$\mathbf{R}(\Omega) := [\Omega, \mathbf{p}(\Omega), \mathbf{q}(\Omega)] = \begin{pmatrix} \sin \theta \cos \varphi & -\sin \varphi & -\cos \theta \cos \varphi \\ \sin \theta \sin \varphi & \cos \varphi & -\cos \theta \sin \varphi \\ \cos \theta & 0 & \sin \theta \end{pmatrix}.$$

654 Since \mathbf{u} and \mathbf{v} belong to the plane spanned by $\mathbf{p}(\Omega)$ and $\mathbf{q}(\Omega)$, we let $\zeta \in [0, 2\pi)$ be the
655 angle between $\mathbf{p}(\Omega)$ and \mathbf{u} . Then, it is an easy matter to show that $A = \mathbf{R}(\Omega) \mathcal{A}(\zeta, \mathbf{e}_1)$. In
656 aircraft navigation, θ , φ and ζ are respectively called the pitch, yaw and roll angles: the
657 pitch and yaw control the aircraft direction with respect to the vertical and in the horizontal
658 plane respectively, while the roll controls the plane attitude (see Fig. 10a). These angles are
659 related to the Euler angles. The construction of the roll angle ζ is summarized in Figure 10b.
660 Pursuing the analogy with aircraft navigation, we see from Fig. 5 that \mathbf{F} controls variations
661 of pitch and yaw while δ controls variations of roll.

662 As an example, we examine the pitch, yaw and roll of the three solutions of the SOHB
663 model (2.11) described in Section 3.1.

- 664 1. FS: \mathbb{A} is constant and uniform. Then, the pitch, yaw and roll are also constant and
665 uniform.
- 666 2. MO: \mathbb{A} is given by (3.2) (see Figs. 6). Using Eq. (3.3), we have $\mathbf{R}(\Omega) = \mathcal{A}(-\omega t, \mathbf{e}_3)$
667 and the roll is given by $\zeta = \xi z$. The pitch and yaw are constant and uniform. The
668 roll is constant in time and is also uniform on planes of constant z . The non-trivial
669 topology of the MO results from the roll making a complete turn when z increases by
670 the quantity $2\pi/\xi$.
- 671 3. HW: \mathbb{A} is given by (3.5) (see Fig. 7). Then, we have $\mathbf{R}(\Omega) = \mathbf{I}_3$ and $\zeta = \xi(x - \lambda t)$.
672 The pitch and yaw are constant and uniform while the roll is uniform on planes of
673 constant x . It depends on x and time through the traveling phase $x - \lambda t$. Here, the
674 non-trivial topology results from the roll making a complete turn when x increases by
675 the quantity $2\pi/\xi$.

676 The goal of the next section is to see how we can recover the roll field from the simulation of
677 a large particle system.

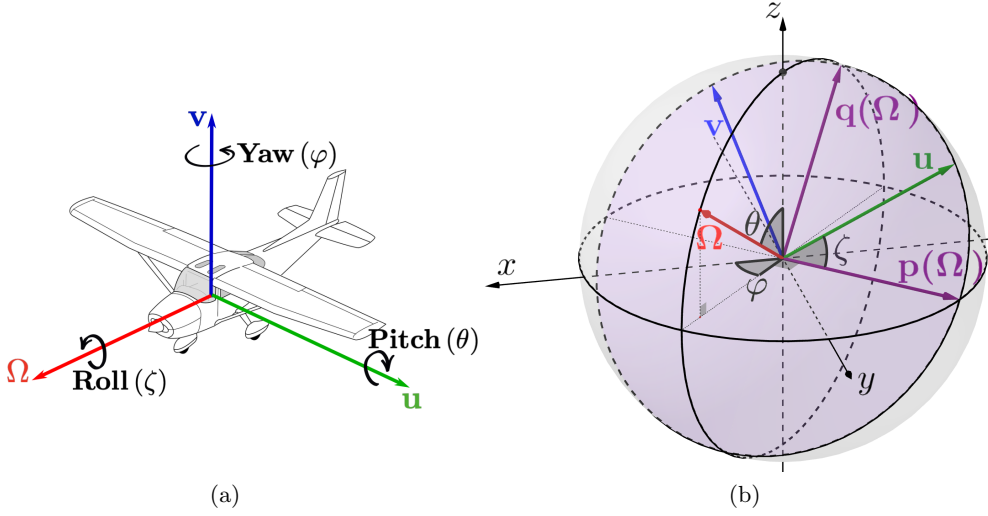


Figure 10: (a) Pitch, yaw and roll angles of an aircraft with body orientation $[\Omega, \mathbf{u}, \mathbf{v}]$ (original picture released under the Creative Commons CC0 license by <https://pixabay.com>). (b) Construction of the roll angle of $A = [\Omega, \mathbf{u}, \mathbf{v}]$, where the vectors Ω , \mathbf{u} and \mathbf{v} are respectively in red, green and blue. The local frame is $(\Omega, \mathbf{p}(\Omega), \mathbf{q}(\Omega))$ where $\mathbf{p}(\Omega)$ and $\mathbf{q}(\Omega)$ and the plane generated by them are in purple. \mathbf{u} and \mathbf{v} belong to this plane. ζ is the angle between $\mathbf{p}(\Omega)$ and u .

678 **4.2.2. Roll polarization.** As shown in the last section, the roll of the MO is uniform
 679 on planes of constant z . When simulating the MO by the IBM, we will use this property to
 680 compute an average roll on planes of constant z . To cope with the discreteness of the particles,
 681 we will rather consider slices comprised between two planes of constant z . If the distance Δz
 682 between the planes is chosen appropriately, we can access to both the average and the variance
 683 of the roll. They will be collected into one single vector, the Roll Polarization in planes of
 684 constant z or RPZ. A similar quantity characterizes the HW, the Roll Polarization in planes
 685 of constant x or RPX. Below, we detail the construction of the RPZ. Obviously the procedure
 686 is the same (changing z into x) for the RPX.

We assume that the domain is a rectangular box of the form $\mathcal{D} := [0, L_x] \times [0, L_y] \times [0, L_z]$, and $L_z = n(2\pi/\xi)$ with $n \in \mathbb{Z} \setminus \{0\}$. The domain \mathcal{D} is partitioned into M slices of fixed size across z , where M is a fixed integer. For $m \in \{1, \dots, M\}$, the slice S_m is defined by:

$$S_m := [0, L_x] \times [0, L_y] \times \left[\frac{m-1}{M} L_z, \frac{m}{M} L_z \right].$$

687 Let us consider a system of N agents with positions and body-orientations (\mathbf{X}_k, A_k) , indexed
 688 by $k \in \{1, \dots, N\}$. Each body orientation A_k has roll $\zeta_k \in [0, 2\pi)$. We define the discrete

689 RPZ for Slice m , $\bar{\mathbf{u}}_m$, by

690 (4.9)
$$\bar{\mathbf{u}}_m := \frac{1}{N_m} \sum_{k \in I_m} (\cos \zeta_k, \sin \zeta_k)^T \in \mathbb{R}^2,$$

691 where $I_m = \{k \in \{1, \dots, N\}, X_k \in S_m\}$ and N_m is the cardinal of I_m . Note that the RPZ $\bar{\mathbf{u}}_m$
 692 has norm smaller than one. The unit vector $\bar{\mathbf{u}}_m/|\bar{\mathbf{u}}_m|$ or equivalently, its angle with the vector
 693 $(1, 0)^T$ gives the average roll in S_m . The euclidean norm $|\bar{\mathbf{u}}_m|$ is a measure of the variance of
 694 the set of roll angles $\{\zeta_k\}_{k \in I_m}$. If this variance is small, then $|\bar{\mathbf{u}}_m| \sim 1$, while if the variance is
 695 large, $|\bar{\mathbf{u}}_m| \ll 1$. When plotted in the plane \mathbb{R}^2 , the set of RPZ $\{\bar{\mathbf{u}}_m\}_{m=1, \dots, M}$ forms a discrete
 696 curve referred to as the RPZ-curve. It will be used to characterize the topological state of the
 697 particle system. A summary of this procedure is shown in Figure 11.

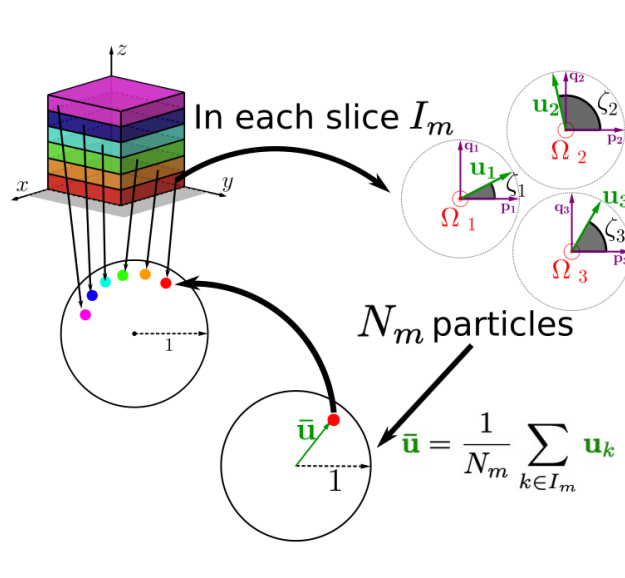


Figure 11: Construction of the RPZ and graphical representation. The spatial domain \mathcal{D} is partitioned into M slices represented in different colors (top left). In each slice S_m , we have I_m particles with roll ζ_k each of them plotted in the particle's local plane spanned by $\mathbf{p}(\Omega_k)$, $\mathbf{q}(\Omega_k)$ (top right: we plot 3 particles in the slice S_1). Note that the local planes of different particles of the same slice may not coincide when imbedded in \mathbb{R}^3 . For this given slice, the RPZ $\bar{\mathbf{u}}_m$ is computed and plotted in \mathbb{R}^2 (bottom right). The RPZ has norm smaller than 1 and belongs to the unit disk, whose boundary, the unit circle, is plotted for clarity. The RPZ of each slice is then plotted on a single figure in the same color as the slice it corresponds to (bottom left). This collection of points forms a discrete curve (here a fragment of a circle): the RPZ-curve.

698 **4.2.3. Indicators of RPZ-curve morphology.** The RPZ-curve is shown in Figure 12 (a)
 699 to (c), in the three following cases.

- 700 1. **Disordered state:** the particles are drawn independently uniformly randomly in the
 701 product space $\mathcal{D} \times \text{SO}_3(\mathbb{R})$. For each m , the RPZ (4.9) is an average of uniformly
 702 distributed vectors on the circle and its norm is therefore close to 0. The RPZ-curve
 703 is thus reduced to the origin, as shown in Figure 12a;
- 704 2. **FS:** the positions of the particles are drawn independently uniformly in \mathcal{D} and their
 705 body-orientations independently according to a von Mises distribution $M_{\mathbb{A}_0}$ with a
 706 fixed mean body orientation $\mathbb{A}_0 \in \text{SO}_3(\mathbb{R})$. In this case, for all slices, the corre-
 707 sponding RPZ (4.9) is an average of identically distributed vectors on the circle whose
 708 distribution is peaked around the same point of the unit circle, and the peak is nar-
 709 rower as κ is larger. Therefore, the RPZ vectors (4.9) concentrate on a point near the
 710 unit circle (Figure 12b). The RPZ-curve reduces to a single point different from the
 711 origin;
- 712 3. **MO:** the positions of the particles are drawn independently uniformly in \mathcal{D} . Then for
 713 a particle at position \mathbf{x} , its body-orientation is drawn independently according to a von
 714 Mises distribution $M_{\mathbb{A}_{\text{mill}}(0,z)}$ with $\mathbb{A}_{\text{mill}}(0,z)$ defined by (3.4) (with $\xi = 2\pi/L_z$). This
 715 time, the von Mises distribution is peaked around a point which depends on z . For
 716 each slice, the position of the RPZ (4.9) depends on m . Since $\mathbb{A}_{\text{mill}}(0,z)$ is L_z -periodic,
 717 the RPZ-curve is a discrete closed circle (Figure 12c). Note that the RPX-curve of a
 718 HW is similar.

719 From Figure 12, we realize that three quantities of interest can be extracted from the
 720 RPZ-curve:

- 721 1. the distance of its center of mass to the origin d_z :

$$722 \quad (4.10) \quad d_z = \left| \frac{1}{M} \sum_{m=1}^M \bar{\mathbf{u}}_m \right|,$$

- 723 2. its mean distance to the origin \bar{r}_z :

$$724 \quad (4.11) \quad \bar{r}_z = \frac{1}{M} \sum_{m=1}^M |\bar{\mathbf{u}}_m|,$$

3. its winding number about the origin w_z : for $m \in \{1, \dots, M\}$, let $\beta_m = \arg((\bar{\mathbf{u}}_m)^1 + i(\bar{\mathbf{u}}_m)^2) \in [0, 2\pi)$ (with $\bar{\mathbf{u}}_m = ((\bar{\mathbf{u}}_m)^1, (\bar{\mathbf{u}}_m)^2)^T$) and $\delta\beta_{m+1/2} \in [-\pi, \pi)$ be such that $\delta\beta_{m+1/2} \equiv \beta_{m+1} - \beta_m$ modulo 2π , where we let $\beta_{M+1} = \beta_1$. Then:

$$w_z = \frac{1}{2\pi} \sum_{m=1}^M \delta\beta_{m+1/2},$$

725 (see e.g. [62, p. 176]).

726 The subscript z indicates that the slicing has been made across z . Similar quantities with an
 727 index ' x ' will correspond to the slicing made across x . Fig. 12d provides a graphical illustration
 728 of the triple (d_z, \bar{r}_z, w_z) . For the examples given above, this triple has the following values:

$$729 \quad (4.12) \quad \text{Disordered state: } (d_z, \bar{r}_z, w_z) = (0, 0, \text{ND}), \text{ where ND stands for "undefined",}$$

$$730 \quad (4.13) \quad \text{FS: } (d_z, \bar{r}_z, w_z) \approx (1, 1, 0),$$

$$731 \quad (4.14) \quad \text{MO: } (d_z, \bar{r}_z, w_z) \approx (0, 1, w), \text{ with } w \neq 0.$$

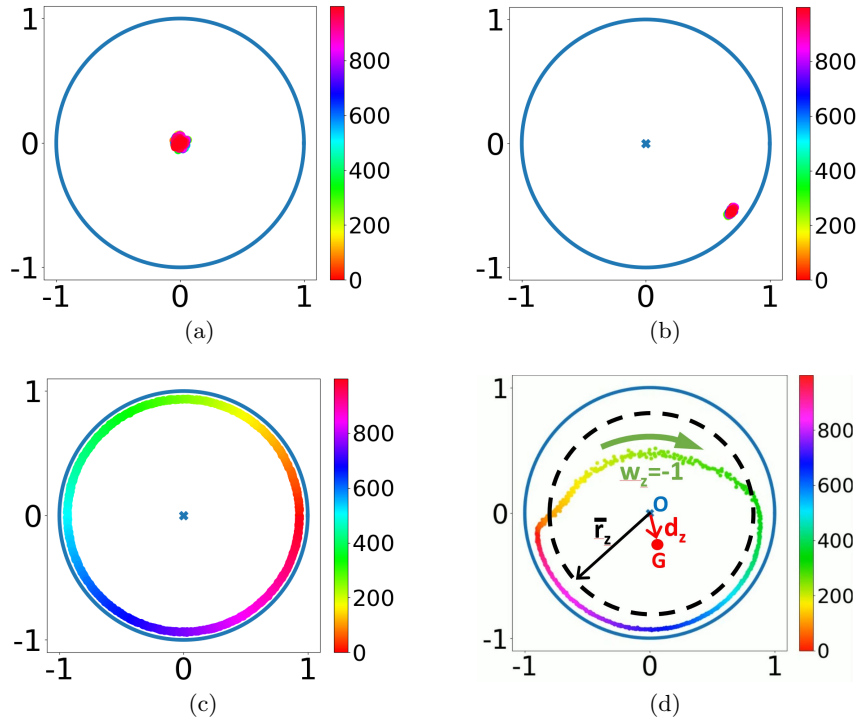


Figure 12: Examples of RPZ-curves: in each figure, the roll Polarization RPZ vectors corresponding to $M = 1000$ slices are plotted. The color bar to the right of each figure assigns a unique color to each slice. The same color is used to plot the corresponding RPZ. In each figure the unit circle and its center are represented in blue. (a) Disordered state: all RPZ concentrate near the origin. (b) FS: all RPZ concentrate on a point close to the unit circle. (c) MO (3.4): the RPZ-curve is a discrete circle centered at the origin and of radius close to unity. The total number of particles is $N = 1.5 \cdot 10^6$. Note that in Figs. (a) and (b), all RPZ are superimposed and only the last one (in magenta color) is visible. (d) Quantifiers of RPZ curve morphology: point G (in red) is the center-of-mass of the RPZ curve and d_z is its distance to the origin O (shown in blue). The mean radius \bar{r}_z of the RPZ curve is illustrated by the circle in black broken line which has same radius. The winding number, which is the number of turns one makes following the spectrum of colors in the same order as in the color bar from bottom to top (the green arrow indicates the direction of progression along the RPZ curve) is $w_z = -1$ in this example.

732 We have a similar conclusion with (d_x, \bar{r}_x, w_x) for a disordered state or an FS. For an HW, we
 733 have $(d_x, \bar{r}_x, w_x) \approx (0, 1, w)$ with $w \neq 0$. Thus, monitoring either or both triples (according
 734 to the situation) will give us an indication of the state of the system in the course of time.
 735 In particular, non-trivial topological states are associated with non-zero winding numbers w_x
 736 or w_z . In practice, we will use the nonzero-rule algorithm to compute the winding numbers

737 numerically [62, p. 176].

738 **5. Topological phase transitions: are the MO and HW topologically protected?** As
 739 pointed out in Section 3.4, for the IBM, the MO and HW are only metastable: they typically
 740 persist for a finite time before degenerating into a FS. This is in stark contrast with the
 741 macroscopic model for which they persist for ever. The transition of a MO or HW to a FS
 742 implies a topological change. To analyze whether the MO or HW are more robust due to
 743 their non-trivial topological structure (i.e. are topologically protected), we will compare them
 744 with similar but topologically trivial initial conditions (Sections 5.1, 5.2 and 5.3). We also
 745 test their robustness against perturbed initial conditions and show that, in this case, MO
 746 may transition to GS (Section 5.4). In the Supplementary Material SM8, we investigate rarer
 747 events, where an MO does not transition directly to an FS but through a HW.

748 **5.1. Initial conditions.** In Section 5.2, we will compare the solutions of the IBM with
 749 different initial conditions using the perpendicular or parallel twists as building blocks. Some
 750 will have a non-trivial topology and the others, a trivial one. Specifically we define the
 751 following initial conditions.

752 **5.1.1. Milling orbit.** Let $\mathcal{D} = [0, L] \times [0, L] \times [0, 2L]$ be a rectangular domain with periodic
 753 boundary conditions and let $\xi = 2\pi/L$. We consider the following two initial conditions:

- 754 • **Double mill** initial condition MO1:

$$755 \quad (5.1) \quad \mathbb{A}_{m,1}(0, z) = \mathcal{A}(\xi z, \mathbf{e}_1), \quad z \in [0, 2L],$$

756 where we recall again that $\mathcal{A}(\theta, \mathbf{n})$ is the rotation of axis $\mathbf{n} \in \mathbb{S}^2$ and angle $\theta \in \mathbb{R}$
 757 defined by (2.8). This initial condition has non-trivial topology: the curve generated
 758 by the end of the vector \mathbf{u} in the (y, z) -plane as z ranges in $[0, 2L]$ makes two complete
 759 turns around the origin in the same direction. Thus, this initial condition has winding
 760 number equal to 2.

- 761 • **Opposite mills** initial condition MO2:

$$762 \quad (5.2) \quad \mathbb{A}_{m,2}(0, z) = \begin{cases} \mathcal{A}(\xi z, \mathbf{e}_1), & z \in [0, L], \\ \mathcal{A}(-\xi z, \mathbf{e}_1), & z \in [L, 2L]. \end{cases}$$

763 This initial condition has trivial topology: starting from $z = 0$, the curve generated
 764 by the end of the vector \mathbf{u} makes one complete turn around the origin in the coun-
 765 terclockwise direction until it reaches $z = L$ but then reverses its direction and makes
 766 a complete turn in the clockwise direction until it reaches $z = 2L$. Thus, this initial
 767 condition has winding number equal to 0 and has trivial topology.

- 768 • **Perturbed double mill** initial condition MO3:

$$769 \quad (5.3) \quad \mathbb{A}_{m,3}(0, z) = \mathcal{A}(\xi z + \sqrt{\sigma} B_z, \mathbf{e}_1), \quad z \in [0, 2L],$$

770 where $(B_z)_z$ is a given one-dimensional standard Brownian motion in the z variable
 771 and $\sigma > 0$ is a variance parameter which sets the size of the perturbation. The
 772 Brownian motion is subject to $B_0 = B_{2L} = 0$ (i.e. it is a Brownian bridge). Similarly
 773 to the initial condition MO1 (5.1), this initial condition has a nontrivial topology, in
 774 this case a winding number equal to 2.

775 **5.1.2. Helical traveling wave.** Let now $\mathcal{D} = [0, 2L] \times [0, L] \times [0, L]$. Compared to the
 776 previous case, the domain has size $2L$ in the x -direction instead of the z -direction. Let again
 777 $\xi = 2\pi/L$. We consider now the following two initial conditions:

778 • **Double helix** initial condition HW1:

$$779 \quad (5.4) \quad \mathbb{A}_{h,1}(0, x) = \mathcal{A}(\xi x, \mathbf{e}_1), \quad x \in [0, 2L],$$

780 This initial condition has non-trivial topology and has winding number equal to 2 by
 781 the same consideration as for initial condition MO1.

782 • **Opposite helices** initial condition HW2:

$$783 \quad (5.5) \quad \mathbb{A}_{h,2}(0, x) = \begin{cases} \mathcal{A}(\xi x, \mathbf{e}_1), & x \in [0, L], \\ \mathcal{A}(-\xi x, \mathbf{e}_1), & x \in [L, 2L]. \end{cases}$$

784 Again, by the same considerations as for MO2, this initial condition has trivial topol-
 785 ogy, i.e. winding number equal to 0.

786 **5.2. Observation of topological phase transitions.** We initialize the IBM by drawing N
 787 positions independently uniformly randomly in the spatial domain and N body-orientations
 788 independently from the von Mises distribution $M_{\mathbb{A}(0, \mathbf{x})}$ where $\mathbb{A}(0, \mathbf{x})$ is one of the initial
 789 conditions MO1 or MO2. Then, we run the IBM and record the various indicators introduced
 790 in Section 4 as functions of time. The results are plotted in Fig. 13, as plain blue lines for
 791 the solution issued from MO1 (the topologically non-trivial initial condition), and as broken
 792 orange lines for that issued from MO2 (the topologically trivial one). We proceed similarly for
 793 the two initial conditions HW1 and HW2 and display the results in Fig. 14. See also Videos 4
 794 to 7 in Section SM1 supplementing Fig. 13 and Videos 8 to 11 supplementing Fig. 14.

795 Figs. 13a and 14a display the GOP. We observe that, for all initial conditions, the GOP
 796 has initial value GOP_1 , which is consistent with the fact that the initial conditions are either
 797 MO or HW. Then, again, for all initial conditions, at large times, the GOP has final value
 798 GOP_2 which indicates that the final state is a FS. This is confirmed by the inspection of the
 799 second line of figures in Figs. 13 and 14 which provide the triplet of topological indicators
 800 (d_z, \bar{r}_z, w_z) for MO solutions and (d_x, \bar{r}_x, w_x) for HW solutions. Specifically, d_z and d_x are given
 801 in Figs. 13d and 14d respectively, \bar{r}_z and \bar{r}_x in Figs. 13e and 14e, and w_z and w_x in Figs. 13f
 802 and 14f. Initially both triplets corresponding to MO1 or HW1 solutions have value $(0, 1, 2)$ as
 803 they should (see (4.14)). Their final value is $(1, 1, 0)$ which indicates a FS (see (4.13)). The fact
 804 that the final state is a FS implies, for MO1 and HW1, first that the IBM has departed from the
 805 MO and HW exact solutions of the macroscopic model described in Sections 3.1.2 and 3.1.3,
 806 and second, that a topological phase transition has taken place, bringing the topologically
 807 non-trivial MO1 and HW1 to a topologically trivial FS. For the topologically trivial MO2
 808 and HW2 initial conditions, no topological phase transition is needed to reach the FS. The
 809 differences in the initial topology of the solutions induce strong differences in the trajectories
 810 followed by the system.

811 For the topologically non-trivial initial conditions MO1 or HW1, the system remains in
 812 the MO or HW state for some time; hence it follows the macroscopic solution during this
 813 phase. Indeed, the GOP displays an initial plateau at the value GOP_1 , while the triplet of
 814 topological indicators stays at the value $(0, 1, 2)$, which characterize the MO or HW state. For

815 MO1, this is also confirmed by the yaw $\bar{\varphi}$ (Fig. 13c, blue curve), which varies linearly in time
 816 and by the pitch $\bar{\theta}$ (Fig. 13b blue curve) which is constant in time, consistently with the MO
 817 solution of the macroscopic model (Section 3.1.2) (see also Fig. 8a for the linear variation
 818 of the yaw). The duration of this initial phase, also referred to as the persistence time, is
 819 significantly longer for HW1 than for MO1. In our experiments, the former can reach several
 820 hundred units of time and sometimes be infinite (up to our computational capacity). By
 821 contrast, the latter is random and of the order of ten units of time. After this initial plateau,
 822 the GOP decreases until it reaches a minimum at a time highlighted in Figs. 13, 14 and
 823 subsequent figures by a gray shaded zone, showing that the system passes through a state of
 824 maximal disorder. Around that time, \bar{r} has a sharp drop which is another confirmation of an
 825 increased disorder. The topological transition precisely occurs at this time with a transition of
 826 the winding number from 2 to 0 through a short sequence of oscillations. However, \bar{r} has not
 827 reached 0 and d has already started to increase, which suggests that disorder is not complete.
 828 At this time also, the linear variation of $\bar{\varphi}$ suddenly stops and $\bar{\varphi}$ remains constant afterward,
 829 while $\bar{\theta}$ shows a small oscillation and jump. For HW1, $\bar{\theta}$ and $\bar{\varphi}$ are initially plateauing with
 830 small oscillations. At the time when the system leaves the HW state (around $t \simeq 178$), we
 831 observe a sudden drop of $\bar{\varphi}$ from 2π to π which indicates that the system suddenly reverses
 832 its average direction of motion. The GOP starts to decrease significantly before this time
 833 so we can infer that during the time period between $t \simeq 125$ and $t \simeq 178$, even though the
 834 mean direction of motion $\bar{\Omega}$ remains constant, groups of particles of almost similar proportions
 835 are moving in opposite directions, which preserves the average direction of motion (and may
 836 explain the oscillations during the initial persistence phase). This is confirmed by Video 8
 837 (see description in Section SM1). Then, once this minimum is reached, the GOP increases
 838 quickly to finally reach the value GOP_2 of the FS. Likewise, \bar{r} and d quickly reach the value 1
 839 while the winding number stays at the value 0.

840 By contrast to the previous case, the system immediately leaves the topologically trivial
 841 initial conditions MO2 or HW2 as shown by the GOP immediately leaving the value GOP_1 .
 842 For HW2 the GOP increases right after initialization and smoothly reaches the value GOP_2 ,
 843 at a much earlier time than HW1. The trend is different for MO2. In this case, the GOP first
 844 decreases. Then, after a minimum value, it increases again and smoothly reaches the value
 845 GOP_2 at a time similar to MO1. The initial decay of the GOP for the MO2 solution can be
 846 explained by the fact that the macroscopic direction Ω turns in opposite directions for the two
 847 opposite mills, thus decreasing the global order. For HW2, the macroscopic direction stays
 848 constant and uniform. So, it is the same for the two opposite helices, giving rise to a larger
 849 GOP. The mean radii \bar{r}_z and \bar{r}_x stay constant it time, showing that the evolutions of MO2
 850 and HW2 do not involve phases of larger disorder. The quantity d_x increases monotonically
 851 towards the value 1 while d_z is subject to some oscillations close to convergence. This is due
 852 to the fact that the RPZ or RPX curves stay arcs of circles with decreasing arc length for
 853 the RPX and with some arc length oscillations for the RPZ as displayed in Videos 7 and 11.
 854 Of course, the winding number stays constant equal to 0 as it should for topologically trivial
 855 solutions. In both the MO2 and HW2 cases, $\bar{\theta}$ and $\bar{\varphi}$ remain constant throughout the entire
 856 simulation. In the MO2 case, this is the consequence of the two counter-rotating mills which
 857 preserve the direction of motion on average. In the HW2 case, this is due to the fact that there
 858 is no variation of the direction of motion for HW solutions in general (see also Video 6 and

859 Video 10). Again, we observe that the convergence towards the FS takes more time for HW2
 860 than for MO2. This points towards a greater stability of the HW-type solutions compared to
 861 the MO ones.

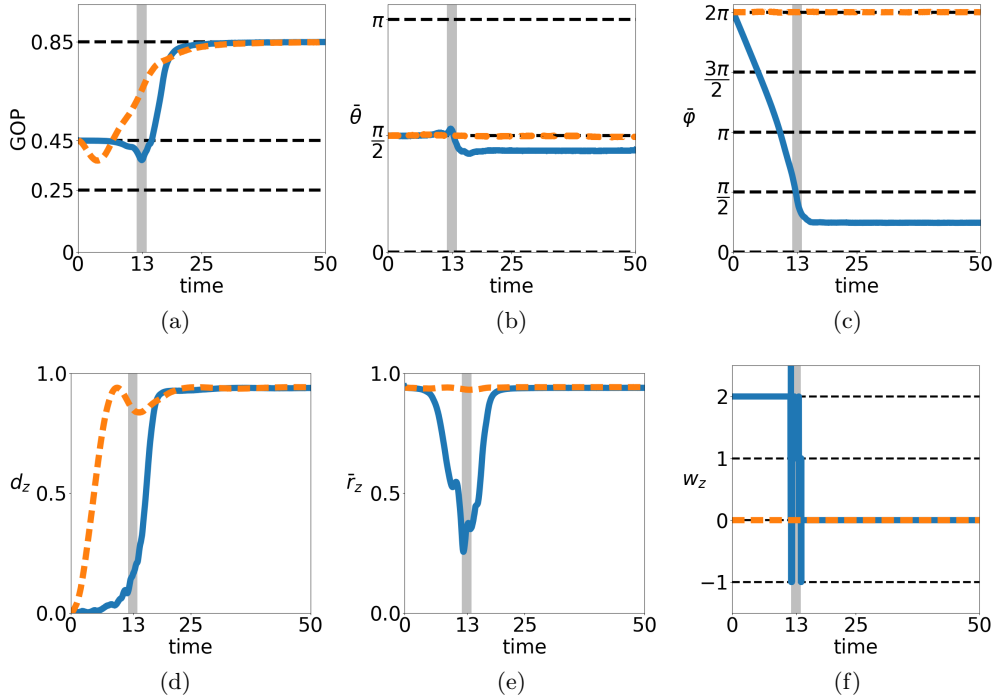


Figure 13: Examples of solutions of the IBM for initial conditions sampled from the double mill MO1 (plain blue curves) and the opposite mills MO2 (boken orange curves). The following indicators are plotted as functions of time: (a) Global Order Parameter (GOP) (see Eq. (4.3)). Horizontal lines at GOP values 0.25, 0.45 and 0.85 materialize the special values GOP_0 , GOP_1 and GOP_2 respectively corresponding to totally disordered states, MO or HW, and FS (see Eqs. (4.6)-(4.8)). (b) Pitch angle $\bar{\theta}$ of the global particle average direction $\bar{\Omega}$ (see (3.10)). (c) Yaw $\bar{\varphi}$ of $\bar{\Omega}$. (d) Distance of center of mass of RPZ curve to the origin d_z (see (4.10)). (e) Mean distance of RPZ curve to the origin \bar{r}_z (see (4.11)). (f) Winding number of RPZ curve w_z (see (4.10)). Gray shaded zones highlight a small region around the time of minimal GOP for the MO1 solution. Parameters: $N = 3 \cdot 10^6$, $R = 0.025$, $\kappa = 10$, $\nu = 40$, $c_0 = 1$, $L = 1$, $\xi = 2\pi$. See also Videos 4 to 7 in Section SM1.

862 **5.3. Reproducibility.** Since the IBM is a stochastic model, one may wonder whether
 863 Figs. 13 and 14 are representative of a typical solution. In Fig. 15, the GOP is plotted
 864 as a function of time for 20 independent simulations with MO1 initial conditions and the
 865 same parameters as in Fig. 13 (blue curves). The same features as in Fig. 13 are observed,
 866 namely: (i) an initial stable milling phase which lasts about 10 units of time; (ii) a decrease
 867 of the GOP between approximately 10 to 15 units of time; (iii) a subsequent increase of the

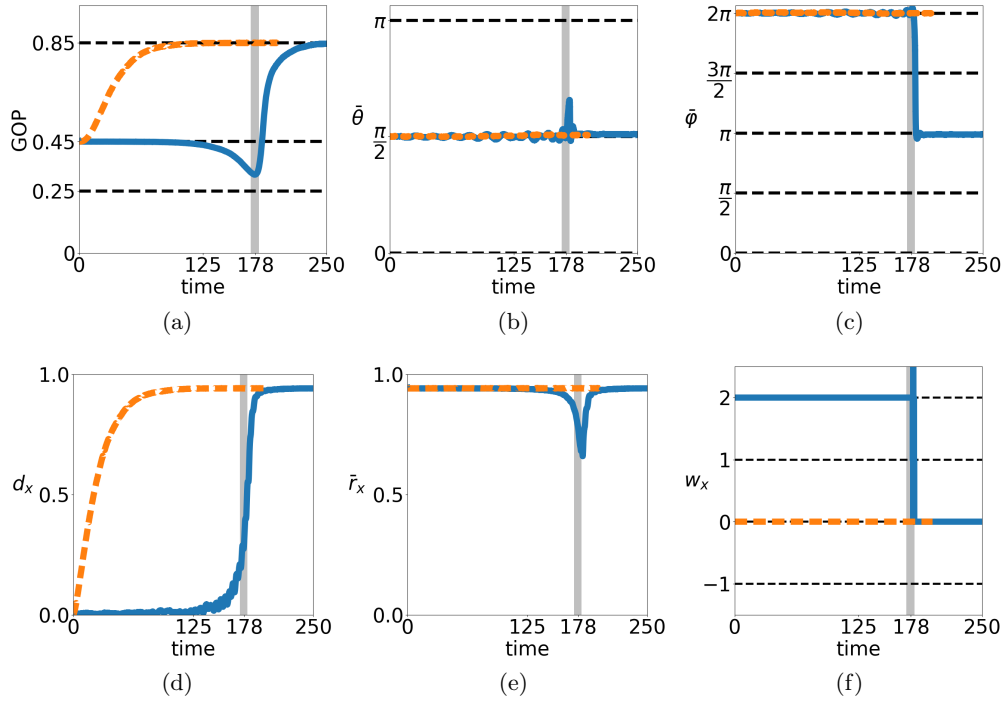


Figure 14: Examples of solutions of the IBM for initial conditions sampled from the double helix HW1 (plain blue curves) and the opposite helices HW2 (broken orange curves). The following indicators are plotted as functions of time: (a) Global Order Parameter (GOP). (b) Pitch angle $\bar{\theta}$ of $\bar{\Omega}$. (c) Yaw $\bar{\varphi}$ of $\bar{\Omega}$. (d) Distance of center of mass of RPX curve to the origin d_x . (e) Mean distance of RPX curve to the origin \bar{r}_x . (f) Winding number of RPX curve w_x . Gray shaded zones highlight a small region around the time of minimal GOP for the HW1 solution. The HW2 and HW1 solutions are computed during 200 and 250 units of time respectively. The two simulations have reached equilibrium by their final time. Parameters: $N = 3 \cdot 10^6$, $R = 0.025$, $\kappa = 10$, $\nu = 40$, $c_0 = 1$, $L = 1$, $\xi = 2\pi$. See caption of Fig. 13 for further indications. See also Videos 8 to 11 in Section SM1.

868 GOP which reaches the value GOP_2 of the FS. A similar reproducibility of the results has
 869 been observed for the other initial conditions (MO2, HW1, HW2) (not shown).

870 **5.4. Robustness against perturbations of the initial conditions.** In this section, we study
 871 the robustness of the MO when the initial condition is randomly perturbed as described by
 872 the initial condition MO3 (5.3). Three typical outcomes for three different values of the
 873 perturbation size σ are shown in Fig. 16. For each value of σ , the temporal evolution of
 874 the four main indicators are shown: the GOP (Figs. 16a, 16e, 16i), the mean polar angle
 875 or pitch (Figs. 16b, 16f, 16j), the mean azimuthal angle or yaw (Figs. 16c, 16g, 16k) and
 876 the winding number along the z -axis (Figs. 16d, 16h, 16l). For small to moderate values
 877 (approximately $\sigma < 100$), the outcomes of the simulation are the same as in Fig. 13 and are

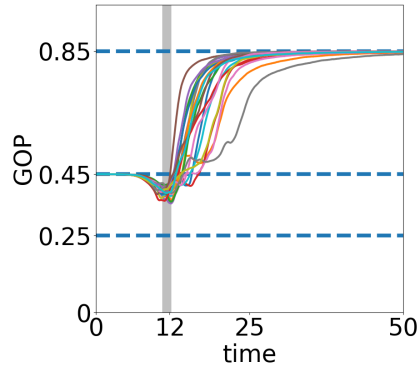


Figure 15: GOP as a function of time for 20 independent simulations of the transition from a MO to a FS starting from MO1. The parameters are the same as the ones on Figure 13.

878 not shown. However, they demonstrates the robustness of the topological solutions. When σ
 879 increases and crosses this threshold, the behavior becomes different. Around this threshold (for
 880 $\sigma = 134$), in Fig. 16a, we observe that the GOP does not remain initially constant (contrary
 881 to the un-perturbed case shown in Fig. 13a) but immediately decreases, then increases and
 882 oscillates around the value GOP_1 before transitioning towards the value GOP_2 corresponding
 883 to a FS. In Figs. 16c and 16d, we observe that the MO is preserved during a comparable,
 884 slightly longer, time than in Figs. 13c and 13f (around 20 units of time) before degenerating
 885 into a FS.

886 Passed this threshold, when σ increases again and up to another threshold value around
 887 $\sigma \simeq 1000$, a new topological phase transition is observed from a MO with winding number 2 to
 888 a GS (3.8) with winding number 1. For $\sigma = 753$, the GOP shown in Fig. 16e initially strongly
 889 oscillates around the value GOP_1 before stabilizing, still around this value, which is in stark
 890 contrast with the previous experiments. The winding number shown in Fig. 16h reveals that
 891 this final steady behavior is linked to a winding number equal to 1 after a transition around
 892 $t \simeq 12$. Consequently, a milling behavior is observed in Fig. 16g for the mean azimuthal
 893 angle. This angle evolves linearly but with a slower speed, approximately divided by 2, after
 894 the transition, as expected since the winding number has dropped from 2 to 1. However, the
 895 final mean polar angle $\bar{\theta}$ shown in Fig. 16f is not equal to $\pi/2$. Since the gradient in body-
 896 orientation is along the z -axis, this indicates that the final state corresponds to a GS rather
 897 than a standard MO. This demonstrates that the family of generalized topological solutions
 898 enjoys some greater stability. The transition between MO and GS has not been observed
 899 when starting from a non-perturbed initial state. However, starting with perturbed initial
 900 conditions, the MO and GS with winding number 1 seem stable during several tens of units
 901 of time.

902 The transition between MO and GS with different winding numbers happens when the
 903 perturbation size is large enough and seems to be the typical behavior: out of 6 independent
 904 simulations for values of σ evenly spread between 258 and 876, 5 simulations led to a MO
 905 or a GS with winding number 1 stable during more than 50 units of time. The other one

906 led to a FS. We can think that the perturbation brings the system to a state closer to the
 907 MO with winding number 1, in particular due to the stochastic spatial inhomogeneities of
 908 the perturbation. On the particle simulations, we observe that the density of agents does not
 909 remain uniform, which creates different milling zones with possibly different milling speeds
 910 depending on the local gradient of body-orientations. The denser region then seems to attract
 911 the other particles before expanding into the full domain. The global direction of motion is
 912 not necessarily preserved during this process. In comparison, starting from an unperturbed
 913 MO with winding number 2, the density remains uniform and the system is globally subject to
 914 numerical errors which homogeneously degrade the topology up to the point that the system
 915 becomes closer to a FS. The situation is analogous when the size of the perturbation is too
 916 large as shown in Figs. 16i, 16k, 16l for $\sigma = 1000$: the MO is preserved during less than 5
 917 units of time and after an immediate drop of the GOP, the system quickly reaches a FS.

918 **5.5. Critique.** The existence of a persistence time for the MO1 and HW1 solutions sug-
 919 gests that they enjoy some kind of topological protection against the noisy perturbations
 920 induced by the IBM and that MO2 and HW2 do not have such protection. However, since ex-
 921 plicit solutions of the SOHB model for the initial conditions MO2 and HW2 are not available,
 922 it is not possible to assess the role of noise in the observed evolutions of the MO2 and HW2
 923 solutions. So, further investigations are needed to confirm that non-trivial topology actually
 924 provides increased robustness against perturbations. Moreover, the MO1 is robust against
 925 perturbed initial conditions. The MO and GS with winding number 1 seem to be much more
 926 more stable than with winding number 2.

927 **6. Discussion and conclusion.** An Individual Based Model describing the alignment of
 928 body-orientations in 3D and its macroscopic limit have been presented. The model involves
 929 new kinds of internal degrees of freedom involving geometrical constraints, here due to the
 930 manifold structure of $SO_3(\mathbb{R})$, leading to new types of self-organized phenomena. In particular,
 931 the macroscopic model has been shown to host special solutions with non-trivial topological
 932 structures. Corresponding solutions of the Individual Based Model have been computed and
 933 their non-trivial topological structure, shown to persist for a certain time before being de-
 934 stroyed by noise-induced fluctuations. Quantitative estimates of the agreement between the
 935 Individual Based Model and the Macroscopic model have been given. This study provides
 936 one more evidence of the role of geometry and topology in the emergence of self-organized
 937 behavior in active particle systems. The model presented in this article opens many new
 938 research directions. Some of them are listed below.

- 939 1. The stability of the MO (3.2), HW (3.5) and GS (3.8) solutions as well as those of
 940 the generalized HW solutions described in Section SM6 is an open problem. It would
 941 enable us to investigate the potential link between topological structure and stability.
- 942 2. Numerical simulations have been carried out in a periodic setting. Real systems though
 943 are confined by solid walls. To model the influence of confinement, it is necessary to
 944 explore wider classes of boundary conditions.
- 945 3. Most topological states in physical systems consist of linear perturbations of bulk
 946 states that propagate on the edges of the system (edge states). It would be interesting
 947 to determine whether linear perturbations of the MO or HW solutions could host such
 948 edge states.

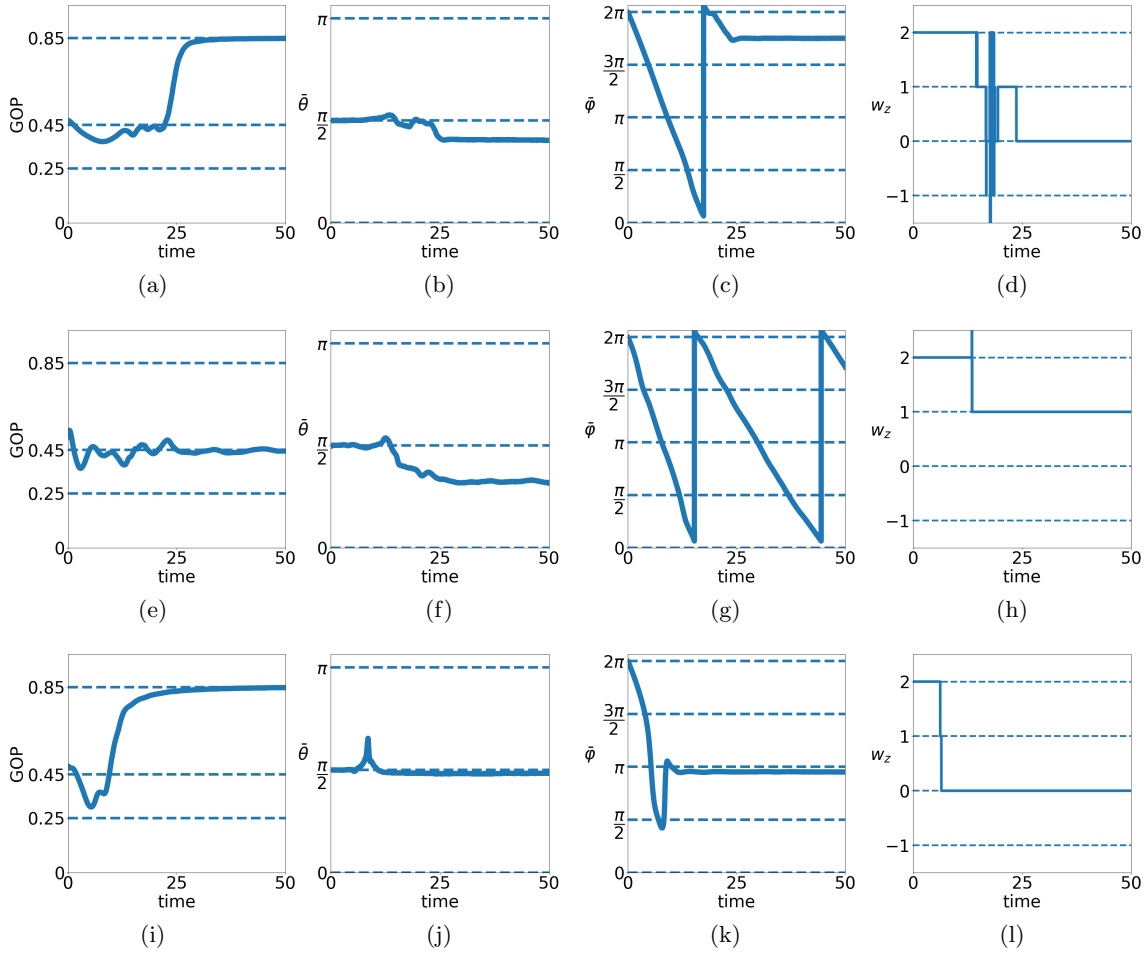


Figure 16: Different outcomes of the simulation of the IBM starting from perturbed initial MO. Only the four main indicators are shown: from left to right, the GOP, the mean polar angle (or pitch) $\bar{\theta}$, the mean azimuthal angle (or yaw) $\bar{\varphi}$ and the winding number w_z . (a)-(d) For $\sigma = 134$, the system stays a MO for a long time ($t \simeq 20$) but eventually converges to a FS; (e)-(h) for $\sigma = 753$, the system converges towards a generalized solution with a polar angle not equal to $\pi/2$ and a winding number equal to 1 along the z -axis; (i)-(l) for $\sigma = 1000$, the MO is quickly disrupted (at $t \simeq 5$) and converges almost immediately towards a FS. Parameters: $N = 3 \cdot 10^6$, $R = 0.025$, $\kappa = 10$, $\nu = 40$, $c_0 = 1$, $L = 1$, $\xi = 2\pi$.

- 949 4. Beyond the mean-field limit $N \rightarrow \infty$, it would be interesting to quantify the fluctuation
950 about the mean-field, for instance through a large deviation approach (see e.g. [6, 7,
951 11, 30, 47, 68]).
952 5. Direct numerical simulations of the macroscopic model need to be developed to answer
953 some of the questions raised by the study of topological protection (see Section 5).

- 954 6. It is desirable to develop more sophisticated topological indicators to gain better insight
 955 into the topological structure of the solutions.
 956 7. The multiscale approach developed here could be extended to other geometrically
 957 structured systems involving e.g. a wider class of manifolds which would enlarge the
 958 applicability of the models.

959 **Acknowledgments.** Part of this research was done when PD was affiliated to Department
 960 of Mathematics, Imperial College London, London, SW7 2AZ, United Kingdom.

961 **Data statement:.** No new data were collected in the course of this research.

962

REFERENCES

- 963 [1] P. ACEVES-SANCHEZ, M. BOSTAN, J.-A. CARRILLO, AND P. DEGOND, *Hydrodynamic limits for kinetic*
 964 *flocking models of Cucker-Smale type*, Math. Biosci. Eng., 16 (2019), pp. 7883–7910.
 965 [2] M. ALDANA, H. LARRALDE, AND B. VÁZQUEZ, *On the emergence of collective order in swarming systems:*
 966 *a recent debate*, Int. J. Mod. Phys. B, 23 (2009), pp. 3661–3685.
 967 [3] I. AOKI, *A simulation study on the schooling mechanism in fish*, Bull. Japan. Soc. Sci. Fish, 48 (1982),
 968 pp. 1081–1088.
 969 [4] A. BARBARO AND P. DEGOND, *Phase transition and diffusion among socially interacting self-propelled*
 970 *agents*, Discrete Contin. Dyn. Syst. Ser. B, 19 (2014), pp. 1249–1278.
 971 [5] A. B. BARBARO, J. A. CANIZO, J. A. CARRILLO, AND P. DEGOND, *Phase transitions in a kinetic flocking*
 972 *model of Cucker-Smale type*, Multiscale Model. Simul., 14 (2016), pp. 1063–1088.
 973 [6] J. BARRÉ, C. BERNARDIN, R. CHÉTRITE, Y. CHOPRA, AND M. MARIANI, *Gamma convergence approach*
 974 *for the large deviations of the density in systems of interacting diffusion processes*, arXiv preprint
 975 arXiv:1910.04026, (2019).
 976 [7] L. BERLYAND, R. CREESE, P.-E. JABIN, AND M. POTOMKIN, *Continuum approximations to systems of*
 977 *correlated interacting particles*, J. Stat. Phys., 174 (2019), pp. 808–829.
 978 [8] E. BERTIN, M. DROZ, AND G. GRÉGOIRE, *Boltzmann and hydrodynamic description for self-propelled*
 979 *particles*, Phys. Rev. E, 74 (2006), p. 022101.
 980 [9] E. BERTIN, M. DROZ, AND G. GRÉGOIRE, *Hydrodynamic equations for self-propelled particles: micro-*
 981 *scopic derivation and stability analysis*, J. Phys. A, 42 (2009), p. 445001.
 982 [10] F. BOLLEY, J. A. CAÑIZO, AND J. A. CARRILLO, *Mean-field limit for the stochastic Vicsek model*, Appl.
 983 Math. Lett., 25 (2012), pp. 339–343.
 984 [11] L. BORTOLUSSI AND N. GAST, *Mean-field limits beyond ordinary differential equations*, in International
 985 School on Formal Methods for the Design of Computer, Communication and Software Systems,
 986 Springer, 2016, pp. 61–82.
 987 [12] M. BOSTAN AND J. A. CARRILLO, *Asymptotic fixed-speed reduced dynamics for kinetic equations in*
 988 *swarming*, Math. Models Methods Appl. Sci., 23 (2013), pp. 2353–2393.
 989 [13] M. BOSTAN AND J. A. CARRILLO, *Reduced fluid models for self-propelled particles interacting through*
 990 *alignment*, Math. Models Methods Appl. Sci., 27 (2017), pp. 1255–1299.
 991 [14] M. BRIANT, A. DIEZ, AND S. MERINO-ACEITUNO, *Cauchy theory and mean-field limit for general Vicsek*
 992 *models in collective dynamics*, arXiv preprint arXiv:2004.00883, (2020).
 993 [15] A. BRICARD, J.-B. CAUSSIN, D. DAS, C. SAVOIE, V. CHIKKADI, K. SHITARA, O. CHEPIZHKO, F. PE-
 994 RUANI, D. SAINTILLAN, AND D. BARTOLO, *Emergent vortices in populations of colloidal rollers*, Nat.
 995 Commun., 6 (2015), p. 7470.
 996 [16] D. S. CALOVI, U. LOPEZ, S. NGO, C. SIRE, H. CHATÉ, AND G. THERAULAZ, *Swarming, schooling,*
 997 *milling: phase diagram of a data-driven fish school model*, New J. Phys., 16 (2014), p. 015026.
 998 [17] J. A. CARRILLO, M. R. D’ORSOGNA, AND V. PANFEROV, *Double milling in self-propelled swarms from*
 999 *kinetic theory*, Kinet. Relat. Models, 2 (2009), p. 363.
 1000 [18] C. CASTELLANO, S. FORTUNATO, AND V. LORETO, *Statistical physics of social dynamics*, Rev. Modern
 1001 Phys., 81 (2009), p. 591.

- 1002 [19] J.-B. CAUSSIN, A. SOLON, A. PESHKOV, H. CHATÉ, T. DAUXOIS, J. TAILLEUR, V. VITELLI, AND
 1003 D. BARTOLO, *Emergent spatial structures in flocking models: a dynamical system insight*, Phys. Rev.
 1004 Lett., 112 (2014), p. 148102.
- 1005 [20] A. CAVAGNA, L. DEL CASTELLO, I. GIARDINA, T. GRIGERA, A. JELIC, S. MELILLO, T. MORA,
 1006 L. PARISI, E. SILVESTRI, M. VIALE, ET AL., *Flocking and turning: a new model for self-organized*
 1007 *collective motion*, J. Stat. Phys., 158 (2015), pp. 601–627.
- 1008 [21] C. CERCIGNANI, R. ILLNER, AND M. PULVIRENTI, *The Mathematical Theory of Dilute Gases*, vol. 106,
 1009 Springer Science & Business Media, 2013.
- 1010 [22] B. CHARLIER, J. FEYDY, J. A. GLAUNÈS, F.-D. COLLIN, AND G. DURIF, *Kernel operations on the GPU,*
 1011 *with autodiff, without memory overflows*, arXiv preprint arXiv:2004.11127, (2020).
- 1012 [23] H. CHATÉ, F. GINELLI, G. GRÉGOIRE, AND F. RAYNAUD, *Collective motion of self-propelled particles*
 1013 *interacting without cohesion*, Phys. Rev. E, 77 (2008), p. 046113.
- 1014 [24] A. COSTANZO AND C. HEMELRIJK, *Spontaneous emergence of milling (vortex state) in a Vicsek-like model,*
 1015 J. Phys. D: Appl. Phys., 51 (2018), p. 134004.
- 1016 [25] I. D. COUZIN AND N. R. FRANKS, *Self-organized lane formation and optimized traffic flow in army ants,*
 1017 Proc. Biol. Sci., 270 (2003), pp. 139–146.
- 1018 [26] I. D. COUZIN, J. KRAUSE, R. JAMES, G. D. RUXTON, AND N. R. FRANKS, *Collective memory and*
 1019 *spatial sorting in animal groups*, Journal of theoretical biology, 218 (2002), pp. 1–12.
- 1020 [27] A. CREPPY, F. PLOURABOUÉ, O. PRAUD, X. DRUART, S. CAZIN, H. YU, AND P. DEGOND, *Symmetry-*
 1021 *breaking phase transitions in highly concentrated semen*, J. R. Soc. Interface, 13 (2016), p. 20160575.
- 1022 [28] F. CUCKER AND S. SMALE, *Emergent behavior in flocks*, IEEE Trans. Automat. Control, 52 (2007),
 1023 pp. 852–862.
- 1024 [29] A. CZIRÓK, E. BEN-JACOB, I. COHEN, AND T. VICSEK, *Formation of complex bacterial colonies via*
 1025 *self-generated vortices*, Phys. Rev. E, 54 (1996), p. 1791.
- 1026 [30] D. A. DAWSON AND J. GÄRTNER, *Large deviations from the McKean-Vlasov limit for weakly interacting*
 1027 *diffusions*, Stochastics, 20 (1987), pp. 247–308.
- 1028 [31] P. DEGOND, *Macroscopic limits of the Boltzmann equation: a review*, in Modeling and Computational
 1029 Methods for Kinetic Equations, P. Degond, L. Pareschi, and G. Russo, eds., Modeling and Simulation
 1030 in Science, Engineering and Technology, Birkhäuser Basel, 2004, pp. 3–57.
- 1031 [32] P. DEGOND, A. DIEZ, A. FROUVELLE, AND S. MERINO-ACEITUNO, *Phase transitions and macroscopic*
 1032 *limits in a BGK model of body-attitude coordination*, J. Nonlinear Sci., 30 (2020), pp. 2671–2736.
- 1033 [33] P. DEGOND, A. FROUVELLE, AND J.-G. LIU, *Macroscopic limits and phase transition in a system of*
 1034 *self-propelled particles*, J. Nonlinear Sci., 23 (2013), pp. 427–456.
- 1035 [34] P. DEGOND, A. FROUVELLE, AND J.-G. LIU, *Phase transitions, hysteresis, and hyperbolicity for self-*
 1036 *organized alignment dynamics*, Arch. Ration. Mech. Anal., 216 (2015), pp. 63–115.
- 1037 [35] P. DEGOND, A. FROUVELLE, AND S. MERINO-ACEITUNO, *A new flocking model through body attitude*
 1038 *coordination*, Math. Models Methods Appl. Sci., 27 (2017), pp. 1005–1049.
- 1039 [36] P. DEGOND, A. FROUVELLE, S. MERINO-ACEITUNO, AND A. TRESCASES, *Some properties of Self-*
 1040 *Organized Hydrodynamics for body orientation*, In preparation.
- 1041 [37] P. DEGOND, A. FROUVELLE, S. MERINO-ACEITUNO, AND A. TRESCASES, *Quaternions in collective*
 1042 *dynamics*, Multiscale Model. Simul., 16 (2018), pp. 28–77.
- 1043 [38] P. DEGOND, A. FROUVELLE, S. MERINO-ACEITUNO, AND A. TRESCASES, *Alignment of self-propelled rigid*
 1044 *bodies: from particle systems to macroscopic equations*, in Stochastic Dynamics Out of Equilibrium,
 1045 G. Giacomin, S. Olla, E. Saada, H. Spohn, and G. Stoltz, eds., vol. 282 of Springer Proceedings
 1046 in Mathematics and Statistics, Institut Henri Poincaré, Paris, France, 2017, Springer International
 1047 Publishing, 2019, pp. 28–66.
- 1048 [39] P. DEGOND, J.-G. LIU, S. MERINO-ACEITUNO, AND T. TARDIVEAU, *Continuum dynamics of the in-*
 1049 *tention field under weakly cohesive social interaction*, Math. Models Methods Appl. Sci., 27 (2017),
 1050 pp. 159–182.
- 1051 [40] P. DEGOND, J.-G. LIU, S. MOTSCH, AND V. PANFEROV, *Hydrodynamic models of self-organized dynam-*
 1052 *ics: derivation and existence theory*, Methods Appl. Anal., 20 (2013), pp. 89–114.
- 1053 [41] P. DEGOND AND S. MOTSCH, *Continuum limit of self-driven particles with orientation interaction*, Math.
 1054 Models Methods Appl. Sci., 18 (2008), pp. 1193–1215.
- 1055 [42] P. DEGOND AND S. MOTSCH, *A macroscopic model for a system of swarming agents using curvature*

- 1056 control, *J. Stat. Phys.*, 143 (2011), pp. 685–714.
- 1057 [43] A. DIEZ, *Propagation of chaos and moderate interaction for a piecewise deterministic system of geomet-*
 1058 *rically enriched particles*, *Electron. J. Probab.*, 25 (2020).
- 1059 [44] A. DIEZ, *SiSyPHE: A Python package for the Simulation of Systems of interacting mean-field Particles*
 1060 *with High Efficiency*, *Journal of Open Source Software*, 6 (2021), p. 3653.
- 1061 [45] G. DIMARCO AND S. MOTSCH, *Self-alignment driven by jump processes : Macroscopic limit and numerical*
 1062 *investigation*, *Math. Models Methods Appl. Sci.*, 26 (2016), pp. 1385–1410.
- 1063 [46] M. R. D’ORSOGNA, Y.-L. CHUANG, A. L. BERTOZZI, AND L. S. CHAYES, *Self-propelled particles with*
 1064 *soft-core interactions: patterns, stability, and collapse*, *Phys. Rev. Lett.*, 96 (2006), p. 104302.
- 1065 [47] B. FERNANDEZ AND S. MÉLÉARD, *A Hilbertian approach for fluctuations on the McKean-Vlasov model*,
 1066 *Stochastic Process. Appl.*, 71 (1997), pp. 33–53.
- 1067 [48] A. FIGALLI, M.-J. KANG, AND J. MORALES, *Global well-posedness of the spatially homogeneous*
 1068 *Kolmogorov–Vicsek model as a gradient flow*, *Arch. Ration. Mech. Anal.*, 227 (2018), pp. 869–896.
- 1069 [49] A. FROUVELLE AND J.-G. LIU, *Dynamics in a kinetic model of oriented particles with phase transition*,
 1070 *SIAM J. Math. Anal.*, 44 (2012), pp. 791–826.
- 1071 [50] I. M. GAMBA, J. R. HAACK, AND S. MOTSCH, *Spectral method for a kinetic swarming model*, *J. Comput.*
 1072 *Phys.*, 297 (2015), pp. 32–46.
- 1073 [51] I. M. GAMBA AND M.-J. KANG, *Global weak solutions for Kolmogorov–Vicsek type equations with orien-*
 1074 *tational interactions*, *Arch. Ration. Mech. Anal.*, 222 (2016), pp. 317–342.
- 1075 [52] J. GAUTRAIS, F. GINELLI, R. FOURNIER, S. BLANCO, M. SORIA, H. CHATÉ, AND G. THERAULAZ,
 1076 *Deciphering interactions in moving animal groups*, *PLoS Comput. Biol.*, (2012).
- 1077 [53] P. GERLEE, K. TUNSTRØM, T. LUNDH, AND B. WENNBERG, *Impact of anticipation in dynamical systems*,
 1078 *Phys. Rev. E*, 96 (2017), p. 062413, <https://doi.org/10.1103/PhysRevE.96.062413>, <https://link.aps.org/doi/10.1103/PhysRevE.96.062413>.
- 1079 [54] Q. GRIETTE AND S. MOTSCH, *Kinetic equations and self-organized band formations*, in *Active Particles*,
 1080 *Volume 2*, Springer, 2019, pp. 173–199.
- 1082 [55] S.-Y. HA, J.-G. LIU, ET AL., *A simple proof of the Cucker–Smale flocking dynamics and mean-field limit*,
 1083 *Commun. Math. Sci.*, 7 (2009), pp. 297–325.
- 1084 [56] S.-Y. HA AND E. TADMOR, *From particle to kinetic and hydrodynamic descriptions of flocking*, *Kinet.*
 1085 *Relat. Models*, 1 (2008), pp. 415–435.
- 1086 [57] C. R. HARRIS, K. J. MILLMAN, S. J. VAN DER WALT, R. GOMMERS, P. VIRTANEN, D. COURNAPEAU,
 1087 E. WIESER, J. TAYLOR, S. BERG, N. J. SMITH, R. KERN, M. PICUS, S. HOYER, M. H. VAN KERK-
 1088 WIJK, M. BRETT, A. HALDANE, J. F. DEL RÍO, M. WIEBE, P. PETERSON, P. GÉRARD-MARCHANT,
 1089 K. SHEPPARD, T. REDDY, W. WECKESSER, H. ABBASI, C. GOHLKE, AND T. E. OLIPHANT, *Array*
 1090 *programming with NumPy*, *Nature*, 585 (2020), pp. 357–362.
- 1091 [58] M. Z. HASAN AND C. L. KANE, *Colloquium: topological insulators*, *Rev. Modern Phys.*, 82 (2010), p. 3045.
- 1092 [59] C. K. HEMELRIJK AND H. HILDENBRANDT, *Schools of fish and flocks of birds: their shape and internal*
 1093 *structure by self-organization*, *Interface Focus*, 2 (2012), pp. 726–737, <https://doi.org/10.1098/rsfs.2012.0025>, <http://dx.doi.org/10.1098/rsfs.2012.0025>.
- 1095 [60] C. K. HEMELRIJK, H. HILDENBRANDT, J. REINDERS, AND E. J. STAMHUIS, *Emergence of oblong school*
 1096 *shape: models and empirical data of fish*, *Ethology*, 116 (2010), pp. 1099–1112.
- 1097 [61] H. HILDENBRANDT, C. CARERE, AND C. K. HEMELRIJK, *Self-organized aerial displays of thousands of*
 1098 *starlings: a model*, *Behavioral Ecology*, 21 (2010), pp. 1349–1359.
- 1099 [62] J. F. HUGHES, A. VAN DAM, M. MCGUIRE, D. F. SKLAR, J. D. FOLEY, S. K. FEINER, AND A. KURT,
 1100 *Computer Graphics: Principles and Practice*, Addison-Wesley Professional, 3rd edition ed., 2013.
- 1101 [63] J. D. HUNTER, *Matplotlib: A 2D graphics environment*, *Comput Sci Eng.*, 9 (2007), pp. 90–95.
- 1102 [64] D. Q. HUYNH, *Metrics for 3D rotations: Comparison and analysis*, *J. Math. Imaging Vis.*, 35 (2009),
 1103 pp. 155–164.
- 1104 [65] N. JIANG, L. XIONG, AND T.-F. ZHANG, *Hydrodynamic limits of the kinetic self-organized models*, *SIAM*
 1105 *J. Math. Anal.*, 48 (2016), pp. 3383–3411.
- 1106 [66] J. T. KENT, A. M. GANEIBER, AND K. V. MARDIA, *A new unified approach for the simulation of a wide*
 1107 *class of directional distributions*, *J. Comput. Graph. Statist.*, 27 (2018), pp. 291–301.
- 1108 [67] K. V. KLITZING, G. DORDA, AND M. PEPPER, *New Method for High-Accuracy Determination of the Fine-*
 1109 *Structure Constant Based on Quantized Hall Resistance*, *Phys. Rev. Lett.*, 45 (1980), pp. 494–497,

- 1110 <https://doi.org/10.1103/physrevlett.45.494>, <http://dx.doi.org/10.1103/PhysRevLett.45.494>.
- 1111 [68] C. LANCELLOTTI, *On the fluctuations about the Vlasov limit for N -particle systems with mean-field in-*
1112 *teractions*, J. Stat. Phys., 136 (2009), pp. 643–665.
- 1113 [69] R. B. LAUGHLIN, *Quantized Hall conductivity in two dimensions*, Phys. Rev. B, 23 (1981), pp. 5632–5633,
1114 <https://doi.org/10.1103/physrevb.23.5632>, <http://dx.doi.org/10.1103/PhysRevB.23.5632>.
- 1115 [70] T. LEE, *Bayesian attitude estimation with the matrix Fisher distribution on $SO(3)$* , IEEE Trans. Automat.
1116 Contr., 63 (2018), pp. 3377–3392.
- 1117 [71] R. LUKEMAN, Y.-X. LI, AND L. EDELSTEIN-KESHET, *Inferring individual rules from collective behavior*,
1118 Proc. Natl. Acad. Sci. USA, 107 (2010), pp. 12576–12580.
- 1119 [72] A. MARTÍN-GÓMEZ, D. LEVIS, A. DÍAZ-GUILERA, AND I. PAGONABARRAGA, *Collective motion of active*
1120 *brownian particles with polar alignment*, Soft Matter, 14 (2018), pp. 2610–2618.
- 1121 [73] S. MOTSCH AND L. NAVORET, *Numerical simulations of a nonconservative hyperbolic system with geo-*
1122 *metric constraints describing swarming behavior*, Multiscale Model. Simul., 9 (2011), pp. 1253–1275.
- 1123 [74] S. MOTSCH AND E. TADMOR, *A new model for self-organized dynamics and its flocking behavior*, J. Stat.
1124 Phys., 144 (2011), p. 923.
- 1125 [75] NOBEL FOUNDATION, *The Nobel Prize in Physics 1985*. [https://www.nobelprize.org/prizes/physics/1985/](https://www.nobelprize.org/prizes/physics/1985/summary/)
1126 [summary/](https://www.nobelprize.org/prizes/physics/1985/summary/).
- 1127 [76] NOBEL FOUNDATION, *The Nobel Prize in Physics 2016*. [https://www.nobelprize.org/prizes/physics/2016/](https://www.nobelprize.org/prizes/physics/2016/summary/)
1128 [summary/](https://www.nobelprize.org/prizes/physics/2016/summary/).
- 1129 [77] A. PASZKE, S. GROSS, F. MASSA, A. LERER, J. BRADBURY, G. CHANAN, T. KILLEEN, Z. LIN,
1130 N. GIMELSHEIN, L. ANTIGA, A. DESMAISON, A. KOPF, E. YANG, Z. DEVITO, M. RAISON, A. TE-
1131 JANI, S. CHILAMKURTHY, B. STEINER, L. FANG, J. BAI, AND S. CHINTALA, *PyTorch: An imperative*
1132 *style, high-performance deep learning library*, in Advances in Neural Information Processing Systems
1133 32, H. Wallach, H. Larochelle, A. Beygelzimer, F. d’Alché Buc, E. Fox, and R. Garnett, eds., Curran
1134 Associates, Inc., 2019, pp. 8024–8035.
- 1135 [78] F. PERUANI, A. DEUTSCH, AND M. BÄR, *A mean-field theory for self-propelled particles interacting by*
1136 *velocity alignment mechanisms*, Eur. Phys. J. Spec. Top., 157 (2008), pp. 111–122.
- 1137 [79] X.-L. QI AND S.-C. ZHANG, *Topological insulators and superconductors*, Rev. Modern Phys., 83 (2011),
1138 p. 1057.
- 1139 [80] D. SCHERER, P. DUBOIS, AND B. SHERWOOD, *VPython: 3D interactive scientific graphics for students*,
1140 Comput Sci Eng., 2 (2000), pp. 56–62.
- 1141 [81] S. SHANKAR, M. J. BOWICK, AND M. C. MARCHETTI, *Topological sound and flocking on curved surfaces*,
1142 Phys. Rev. X, 7 (2017), p. 031039.
- 1143 [82] K. SONE AND Y. ASHIDA, *Anomalous topological active matter*, Phys. Rev. Lett., 123
1144 (2019), p. 205502, <https://doi.org/10.1103/PhysRevLett.123.205502>, [https://link.aps.org/doi/10.](https://link.aps.org/doi/10.1103/PhysRevLett.123.205502)
1145 [1103/PhysRevLett.123.205502](https://link.aps.org/doi/10.1103/PhysRevLett.123.205502).
- 1146 [83] A. SOUSLOV, B. C. VAN ZUIDEN, D. BARTOLO, AND V. VITELLI, *Topological sound in active-liquid*
1147 *metamaterials*, Nature Phys., 13 (2017), p. 1091.
- 1148 [84] D. J. THOULESS, *Quantization of particle transport*, Phys. Rev. B, 27 (1983), pp. 6083–6087, [https:](https://doi.org/10.1103/physrevb.27.6083)
1149 [//doi.org/10.1103/physrevb.27.6083](https://doi.org/10.1103/physrevb.27.6083), <http://dx.doi.org/10.1103/PhysRevB.27.6083>.
- 1150 [85] J. TONER AND Y. TU, *Flocks, herds, and schools: A quantitative theory of flocking*, Phys. Rev. E, 58
1151 (1998), p. 4828.
- 1152 [86] T. VICSEK, A. CZIRÓK, E. BEN-JACOB, I. COHEN, AND O. SHOCHET, *Novel type of phase transition in*
1153 *a system of self-driven particles*, Phys. Rev. Lett., 75 (1995), p. 1226.
- 1154 [87] T. VICSEK AND A. ZAFEIRIS, *Collective motion*, Phys. Rep., 517 (2012), pp. 71–140.
- 1155 [88] T.-F. ZHANG AND N. JIANG, *A local existence of viscous self-organized hydrodynamic model*, Nonlinear
1156 Anal. Real World Appl., 34 (2017), pp. 495–506.

SUPPLEMENTARY MATERIALS: Bulk topological states in a new collective dynamics model*

Pierre Degond[†], Antoine Diez[‡], and Mingye Na[‡]

SM1. List of supplementary videos. This article is supplemented by several videos which can be accessed by following this link: https://figshare.com/projects/Bulk_topological_states_in_a_new_collective_dynamics_model/96491. They are listed and described below.

Video 1. *It supplements Fig. 3 of Section 2.1.2 and provides a visualization of the time evolution of the system considered in this figure.*

Video 2. *It supplements Fig. 6 of Section 3.1.2: it provides a visualization of the time evolution of a MO. Several frames $\mathbb{A} = (\Omega, \mathbf{u}, \mathbf{v}) \in SO_3(\mathbb{R})$ are placed at various locations of space and evolve according to (3.2) (with arbitrary chosen parameters). The vectors Ω , \mathbf{u} and \mathbf{v} are displayed respectively in red, green and blue.*

Video 3. *It supplements Fig. 7 of Section 3.1.3: it provides a visualization of the time evolution of a HW. See caption of Video 2 for details on the graphical representation.*

Video 4. *It supplements Fig. 13 in Section 5.2. It shows the time-evolution of the particles for the initial condition MO1 (5.1). For clarity, only a sample of 5000 particles are shown. We refer to Fig. 3a for details on the representation of the body orientation using four-colored tetrahedra. We notice the ensemble rotation of the particle directions about the z axis until an instability disrupts the body orientation twist along the z axis (around time $t \approx 13$) and eventually drives the system to a FS.*

Video 5. *It supplements Fig. 13 in Section 5.2. It provides the time-evolution of the RPZ curve for the initial condition MO1 (5.1). The RPZ curve remains a circle until time $t \approx 8$ where its radius shrinks down. Then, the RPZ-curve shows a fairly chaotic dynamics during which the topology is lost. This happens around time $t \approx 13$ which is the first time when the RPZ-curve passes through the origin; at this time, the winding number is not defined. Then, the RPZ-curve slowly migrates towards the unit circle while shrinking to a single point which signals a FS. From time $t \approx 15$ on, it remains a single immobile point.*

Video 6. *It supplements Fig. 13 in Section 5.2. It shows the time-evolution of the particles for the initial condition MO2 (5.2). For clarity, only a sample of 5000 particles are shown*

*Submitted to the editors January 21st, 2021

Funding: PD acknowledges support by the Engineering and Physical Sciences Research Council (EPSRC) under grants no. EP/M006883/1 and EP/P013651/1, by the Royal Society and the Wolfson Foundation through a Royal Society Wolfson Research Merit Award no. WM130048. The work of AD is supported by an EPSRC-Roth scholarship cofounded by the Engineering and Physical Sciences Research Council and the Department of Mathematics at Imperial College London.

[†]Institut de Mathématiques de Toulouse; UMR5219; Université de Toulouse; CNRS; UPS; F-31062 Toulouse Cedex 9, France (pierre.degond@math.univ-toulouse.fr, <https://sites.google.com/site/degond/Home>).

[‡]Department of Mathematics, Imperial College London, London, SW7 2AZ, United Kingdom (antoine.diez18@imperial.ac.uk, mingye.na18@imperial.ac.uk).

SM1

31 (see Fig. 3a for details on the representation of the body orientation). We notice the counter-
 32 rotation of the particle directions about the z axis in the bottom and top halves of the domain,
 33 corresponding to the opposite mills. These two counter-rotations gradually dissolve while the
 34 solution approaches the FS.

35 **Video 7.** It supplements Fig. 13 in Section 5.2. It provides the time-evolution of the
 36 RPZ curve for the initial condition MO2 (5.2). The circle formed by the initial RPZ curve
 37 immediately opens. The opening width constantly increases, until the arc is reduced to a single
 38 point opposite to the opening point at time $t \approx 10$. Then there is a bounce and the arc forms
 39 again and increases in size until it reaches a maximum and decreases again. Several bounces
 40 are observed with decreasing amplitudes. These bounces result in the non-monotonous behavior
 41 of the quantity d_z displayed on Fig. 13d.

42 **Video 8.** It supplements Fig. 14 in Section 5.2. It shows the time-evolution of the particles
 43 for the initial condition HW1 (5.4) (see Fig. 3a for details on the representation of the body
 44 orientation). For clarity, only a sample of 5000 particles are shown. Before time $t \approx 125$,
 45 we observe a steady HW state. Then, after time $t \approx 125$, the particles show an undulating
 46 wave-like behavior, with slowly increasing frequency and amplitude, which causes the decrease
 47 of the GOP. Around time $t \approx 178$, the particles are divided into two groups with pitch angles
 48 $\theta \simeq 0$ and $\theta \simeq \pi$, which suddenly reverses the global direction of motion. After time $t \approx 178$,
 49 the particles quickly adopt the same body-orientation. Shortly after time $t = 178$, the particles
 50 still have an undulating behavior but it quickly fades away until a FS is reached.

51 **Video 9.** It supplements Fig. 14 in Section 5.2. It shows the time-evolution of the RPX-
 52 curve for the initial condition HW1. Unlike in the MO case, the RPX curve does not shrink
 53 to the center of the circle before migrating to its limiting point. In this case, the limiting point
 54 near the unit circle towards which the RPX curve is converging attracts the RPX. During this
 55 transition, the circular shape of the RPX curve is preserved until it becomes a point.

56 **Video 10.** It supplements Fig. 14 in Section 5.2. It shows the time-evolution of the parti-
 57 cles for the initial condition HW2 (5.5). For clarity, only a sample of 5000 particles are shown
 58 (see Fig. 3a for details on the representation of the body orientation). At the beginning, we see
 59 two opposite alternations of the three side colors of the tetrahedra (green-blue-magenta followed
 60 by green-magenta-blue), which signals a double parallel twist. Then, gradually, the green color
 61 is eaten up by the blue and magenta ones and only one alternation of the blue and magenta
 62 colors remains. Then the color alternation shades away and gives room to a homogeneous
 63 color showing that the body orientations have stopped rolling and a FS is attained.

64 **Video 11.** It supplements Fig. 14 in Section 5.2. It provides the time-evolution of the
 65 RPX curve for the initial condition HW2 (5.5). The circle formed by the initial RPX curve
 66 immediately opens. The opening width constantly increases, although at a slower pace than
 67 for MO2 (see Video 7). Here, also contrasting with the MO2 case, the monotonous opening
 68 of the arc results in a monotonously increasing quantity d_x as shown in Fig. 14d.

69 **Video 12.** It supplements Fig. SM2 in Section SM8.1. It shows the time-evolution of the
 70 particles for a MO initial condition (5.1) in a rare case where it evolves into a HW. For clarity,
 71 only a sample of 5000 particles are shown (see Fig. 3a for details on the representation of the
 72 body orientation). It starts like Video 4 with the ensemble rotation of the particle directions

73 about the z axis until an instability initiated at time $t \approx 10$ gradually disrupts this organization.
 74 However, the disruption does not drive the system to an FS, but rather to a HW as shown by
 75 the alternations of blue, green and magenta colors propagating along the particle orientations.

76 **Video 13.** It supplements Fig. SM2 in Section SM8.1. It provides the time-evolution of
 77 the RPZ curve for a MO initial condition (5.1) in a rare case where it evolves into a HW. The
 78 behavior is essentially the same as in Video 5 except that the RPZ-curve shrinks to a single
 79 point far away from the unit circle. This shows that the end state of the RPZ-curve is closer to
 80 disorder than for a milling to flocking transition. Before that, the non-trivial topology across z
 81 is lost following a similar scenario as for the milling-to-flocking transition.

82 **Video 14.** It supplements Fig. SM2 in Section SM8.1. It provides the time-evolution of
 83 the RPX curve for a MO initial condition (5.1) in a rare case where it evolves into a HW.
 84 Initially, the RPX-curve is reduced to the origin, showing total disorder across the x direction.
 85 Then, after some chaotic transient, a closed curve enclosing the origin is formed. This curve
 86 initially stays close to the origin, still showing strong disorder. But gradually, the radius of
 87 the curve increases and approaches the unit circle. Thus, across x , the topology is initially
 88 undefined, but when it builds up, it shows its non-trivial character, the emerging RPX-curve
 89 having non-zero winding number about the origin.

90 **Video 15.** It supplements Fig. SM3 in Section SM8.2. It shows the time-evolution of the
 91 particles for a MO initial condition (5.1) in a rare case where it evolves into a FS through
 92 a transient HW. For clarity, only a sample of 5000 particles are shown (see Fig. 3a for
 93 details on the representation of the body orientation). The point of view is changed from
 94 Video 12 to better visualize the transient HW moving along the diagonal, appearing around
 95 time $t \approx 16$. At the beginning we witness the ensemble rotation of the particles and its
 96 disruption by an instability. After some chaotic behavior, the transient HW establishes as
 97 shown by the alternations of blue, green and magenta colors propagating along the diagonal.
 98 But after some time, the HW structure is disrupted again and the system eventually establishes
 99 a FS.

100 **Video 16.** It supplements Fig. SM3 in Section SM8.2. It provides the time-evolution of the
 101 RPZ curve for a MO initial condition (5.1) in a rare case where it evolves into a FS through
 102 a transient HW. The behavior is essentially the same as in Video 5 except that the RPZ-curve
 103 undergoes a longer-lasting chaotic dynamics before shrinking to a point which migrates towards
 104 the unit circle.

SM2. Quaternion framework. Despite its formal simplicity, the $\text{SO}_3(\mathbb{R})$ -framework used
 in the definition of the Individual Based Model is not well suited to numerical simulations due
 to the high computational cost required to store and manipulate rotation matrices. A more
 efficient representation of rotations in \mathbb{R}^3 is the quaternion representation based on the group
 isomorphism

$$\begin{aligned} \Phi : \mathbb{H} / \pm 1 &\longrightarrow \text{SO}_3(\mathbb{R}) \\ q &\longmapsto \Phi(q) : \mathbf{w} \in \mathbb{R}^3 \mapsto \{q[\mathbf{w}]q^*\} \in \mathbb{R}^3, \end{aligned}$$

105 where the 3-dimensional vector $\mathbf{w} = (w_1, w_2, w_3)^T \in \mathbb{R}^3$ is identified with the pure imaginary
 106 quaternion denoted by $[\mathbf{w}] = iw_1 + jw_2 + kw_3$ and q^* denotes the conjugate quaternion

107 to q . Conversely, the pure imaginary quaternion $q = iq_1 + jq_2 + kq_3$ is identified with the
 108 3-dimensional vector denoted by $\{q\} := (q_1, q_2, q_3)^T$. Note that for any quaternion q and any
 109 vector $\mathbf{w} \in \mathbb{R}^3$, the quaternion $q[\mathbf{w}]q^*$ is a pure imaginary quaternion. The group of unit
 110 quaternions is denoted by \mathbb{H} and is homeomorphic to the sphere $\mathbb{S}^3 \subset \mathbb{R}^4$.

111 We refer the reader to [SM5, Section 2] and [SM4, Appendix A] where details about the
 112 equivalence between the two representations can be found. Note that [SM4] studies a model
 113 in a full quaternion framework. Table SM1 below summarizes how the different objects can
 114 be computed in either of the two representations.

	Matrix	Quaternion
Orientation	$A \in \text{SO}_3(\mathbb{R})$	$q \in \mathbb{H}/\pm 1$ such that $\Phi(q) = A$
Flux	$J_k = \sum_j K(\mathbf{X}_k - \mathbf{X}_j)A_j$	$Q_k = \sum_j K(\mathbf{X}_k - \mathbf{X}_j)(q_j \otimes q_j - 1/4\mathbf{I}_4)$
Mean orientation	$\mathbb{A} = \arg \max\{A \mapsto A \cdot J\}$	$\bar{q} \in \mathbb{H}$ eigenvector associated to the largest eigenvalue of Q
Von Mises distribution	$M_{\mathbb{A}}(A) = \frac{\exp(\kappa\mathbb{A} \cdot A)}{\mathcal{Z}}$	$M_{\bar{q}}(q) = \frac{\exp(2\kappa(\bar{q} \cdot q)^2)}{\mathcal{Z}}$

Table SM1: Matrix *vs* quaternion formulation

115 **SM3. Numerical methods.** The IBM (2.3), (2.5) has been discretized within the quater-
 116 nion framework using the time-discrete algorithm described in Table SM2 below. This table
 117 shows one iteration of the algorithm during which the positions $\mathbf{X}_k^n \in \mathbb{R}^3$ and orientations
 118 $q_k^n \in \mathbb{H}$ for $k \in \{1, \dots, N\}$ are updated into \mathbf{X}_k^{n+1} and q_k^{n+1} respectively.

Algorithm: Iteration $n \rightarrow n + 1$ of the time-discrete algorithm
<p>1. Update the positions: for $k \in \{1, \dots, N\}$, set $\mathbf{X}_k^{n+1} = \mathbf{X}_k^n + c_0 \{q_k^n[\mathbf{e}_1](q_k^n)^*\} \Delta t$</p> <p>2. Draw a subset $I \subset \{1, \dots, N\}$ of jumping agents: for each agent $k \in \{1, \dots, N\}$, draw a random number r_k uniformly in $[0, 1]$. If $r_k > \exp(-\nu \Delta t)$, then $k \in I$.</p> <p>3. Compute the local flux: for $k \in I$, compute</p> $\bar{Q}_k^n = \frac{1}{N} \sum_{j=1}^N K(\mathbf{X}_k^n - \mathbf{X}_j^n)(q_j^n \otimes q_j^n - \frac{1}{4}\mathbf{I}_4).$ <p>4. Update the orientations: for $k \in I$ compute one unit eigenvector \bar{q}_k^n of Q_k^n of maximal eigenvalue and draw $q_k^{n+1} \sim M_{\bar{q}_k^n}$.</p>

Table SM2: One iteration of the time-discrete algorithm

119 At step 2, the Poisson process is discretized with a time step Δt during which the indices
 120 of the jumping agents are recorded. In the simulations Δt has to be chosen small enough so
 121 that the event that an agent jumps twice or more during a time interval of size Δt is negligible.
 122 In all the simulations, we take Δt such that $\nu \Delta t = 10^{-2}$.

123 At step 3, a random quaternion q sampled from a von Mises distribution with prescribed
 124 mean orientation \bar{q} can be obtained as $q = \bar{q}r$ where $r \in \mathbb{H}$ is sampled from a von Mises dis-
 125 tribution with mean orientation 1 (see [SM5, Proposition 9]). An efficient rejection algorithm
 126 to sample von Mises distributions can be found in [SM9].

127 All the simulations in this paper take place in a periodic box of size $L = (L_x, L_y, L_z)$. The
 128 observation kernel K is the indicator of the ball centered at 0 and of radius $R > 0$. The six
 129 parameters of the simulations are summarized in Table 1.

130 Finally, we would like to stress that the quaternion formulation is not only a convenient
 131 numerical trick. The equivalence it provides between body-orientation models and models of
 132 nematic alignment of polymers in dimension four has been exploited in [SM2] to study phase
 133 transitions in the body alignment model.

134 **SM4. Derivation of the macroscopic model.** The derivation of the continuum theory
 135 presented in Section 2.2 has been achieved in [SM5] (see also [SM2]) following earlier works
 136 [SM3, SM4]. It consists of two steps. The first step is the derivation of a mean-field kinetic
 137 model in the limit $N \rightarrow \infty$ showing that the system satisfies the propagation of chaos property:
 138 the agents, seen as random variables in $\mathbb{R}^3 \times \text{SO}_3(\mathbb{R})$ become independent and identically dis-
 139 tributed. Their law is given by the kinetic particle distribution f which satisfies the following
 140 PDE:

$$141 \quad \partial_t f + c_0 A e_1 \cdot \nabla_{\mathbf{x}} f = \nu (\rho_f M_{\mathbb{A}_{K^*f}} - f),$$

where $\rho_f \equiv \rho_f(t, \mathbf{x})$ is the local spatial density:

$$\rho_f(t, \mathbf{x}) = \int_{\text{SO}_3(\mathbb{R})} f(t, \mathbf{x}, A) dA,$$

and $\mathbb{A}_{K^*f} \equiv \mathbb{A}_{K^*f}(t, \mathbf{x})$ is the local average body-attitude defined by

$$\mathbb{A}_{K^*f}(t, \mathbf{x}) := \arg \max_{A \in \text{SO}_3(\mathbb{R})} A \cdot J_{K^*f}(t, \mathbf{x}),$$

computed from the local flux:

$$J_{K^*f} \equiv J_{K^*f}(t, \mathbf{x}) := \iint_{\mathbb{R}^3 \times \text{SO}_3(\mathbb{R})} K(\mathbf{x} - \mathbf{y}) A f(t, \mathbf{y}, A) d\mathbf{y} dA.$$

142 From a mathematical point of view, the probability distribution $f \equiv f(t, \mathbf{x}, A)$ is obtained as
 143 the limit in law of the empirical measure of the N -particle system. We refer to [SM7] where a
 144 rigorous proof of this result is presented for a similar model, and to [SM1] for a related work
 145 on the Vicsek model.

146 In the macroscopic regime the agent interactions become strong, which is expressed by
 147 the following hydrodynamic scaling:

$$148 \quad \varepsilon \sim \frac{c_0}{\nu L} \sim \frac{R}{L} \ll 1,$$

149 where L is a typical macroscopic length-scale of the system (such as the typical size of the
 150 flock). We define $\tilde{c}_0 = \varepsilon\nu L = \mathcal{O}(1)$ and $c'_0 = c_0/\tilde{c}_0$. Then, defining dimensionless time and
 151 space variables t' and \mathbf{x}' such that $\mathbf{x} = L\mathbf{x}'$ and $t = (L/\tilde{c}_0)t'$, we obtain (dropping the primes
 152 for simplicity):

$$153 \quad (\text{SM4.1}) \quad \partial_t f^\varepsilon + c_0 \mathbf{A} \mathbf{e}_1 \cdot \nabla_{\mathbf{x}} f^\varepsilon = \frac{1}{\varepsilon} (\rho_{f^\varepsilon} M_{\mathbb{A}_{f^\varepsilon}} - f^\varepsilon) + \mathcal{O}(\varepsilon),$$

where

$$\mathbb{A}_{f^\varepsilon} \equiv \mathbb{A}_{f^\varepsilon}(t, \mathbf{x}) := \arg \max_{A \in \text{SO}_3(\mathbb{R})} A \cdot J_{f^\varepsilon}(t, \mathbf{x}),$$

and

$$J_{f^\varepsilon} \equiv J_{f^\varepsilon}(t, \mathbf{x}) := \int_{\text{SO}_3(\mathbb{R})} A f^\varepsilon(t, \mathbf{x}, A) \, dA.$$

154 This last expression is obtained by Taylor expanding $J_{K * f^\varepsilon} = J_{f^\varepsilon} + \mathcal{O}(\varepsilon^2)$ and means that
 155 the interactions between the agents become spatially localized in the macroscopic regime.

156 The macroscopic model is obtained by formally taking the limit $\varepsilon \rightarrow 0$ in (SM4.1). If such
 157 a limit exists, it is necessarily of the form

$$158 \quad (\text{SM4.2}) \quad f^\varepsilon \xrightarrow{\varepsilon \rightarrow 0} \rho M_{\mathbb{A}}$$

where $\rho \equiv \rho(t, \mathbf{x})$ and $\mathbb{A} \equiv \mathbb{A}(t, \mathbf{x})$ depend on t and \mathbf{x} . Thus, the limiting distribution is fully
 described by the spatial density of agents and their average orientation. To obtain a system
 of equations for (ρ, \mathbb{A}) , we first use the local conservation of mass: integrating (SM4.1) over
 $\text{SO}_3(\mathbb{R})$ and noting the right-hand side vanishes, it holds that,

$$\partial_t \int_{\text{SO}_3(\mathbb{R})} f^\varepsilon \, dA + c_0 \int_{\text{SO}_3(\mathbb{R})} \mathbf{A} \mathbf{e}_1 \cdot \nabla_{\mathbf{x}} f^\varepsilon \, dA = \mathcal{O}(\varepsilon).$$

159 When $\varepsilon \rightarrow 0$, assuming (SM4.2) and using (4.4), we obtain (2.11a).

To obtain an equation for \mathbb{A} , it could be tempting to pursue this approach and multiply
 (SM4.1) by A before integrating it over $\text{SO}_3(\mathbb{R})$. However, the term resulting from the right-
 hand side of (SM4.1) does not vanish but equals (using (4.4) again):

$$\frac{1}{\varepsilon} \int_{\text{SO}_3(\mathbb{R})} A (\rho_{f^\varepsilon} M_{\mathbb{A}_{f^\varepsilon}} - f^\varepsilon) \, dA = \frac{1}{\varepsilon} \left(\frac{c_1}{c_0} \rho_{f^\varepsilon} \mathbb{A}_{f^\varepsilon} - J_{f^\varepsilon} \right) \neq 0.$$

Due to the factor ε^{-1} , its limit as $\varepsilon \rightarrow 0$ is unknown. An easy fix can be found if, instead
 of multiplying Eq. (SM4.1) by A before integrating it over $\text{SO}_3(\mathbb{R})$, we multiply it by the
 quantity $\psi_{\mathbb{A}_{f^\varepsilon}}(A) := \mathbb{A}_{f^\varepsilon}^T A - A^T \mathbb{A}_{f^\varepsilon}$. The rationale for using this quantity is because we aim
 to find an equation for the time-derivative of \mathbb{A} . Such a derivative must lie in the tangent
 space to $\text{SO}_3(\mathbb{R})$ at \mathbb{A} , denoted by $T_{\mathbb{A}}$. This suggests to multiply (SM4.1) by an element of
 $T_{\mathbb{A}}$. Given an arbitrary matrix A , a natural way to obtain an element of $T_{\mathbb{A}}$ is to take its
 orthogonal projection on $T_{\mathbb{A}}$, which is given by $\frac{1}{2}(A - \mathbb{A}A^T\mathbb{A})$. We could therefore choose to
 multiply (SM4.1) by this quantity. But a further simplification is possible by noting that this
 quantity is equal to $\frac{1}{2}\mathbb{A}\psi_{\mathbb{A}}(A)$ and that $\frac{1}{2}\mathbb{A}$ does not depend on A and so can be factored

out of the integral with respect to A . These considerations naturally lead to the choice of the antisymmetric matrix $\psi_{\mathbb{A}_{f^\varepsilon}}(A)$ as a multiplier. Because $\mathbb{A}_{f^\varepsilon}$ is obtained as the polar decomposition of J_{f^ε} , there exists a symmetric matrix S such that $J_{f^\varepsilon} = \mathbb{A}_{f^\varepsilon} S$. Using this remark and (4.4), we easily find that

$$\frac{1}{\varepsilon} \int_{\text{SO}_3(\mathbb{R})} \psi_{\mathbb{A}_{f^\varepsilon}}(A) (\rho_{f^\varepsilon} M_{\mathbb{A}_{f^\varepsilon}} - f^\varepsilon) dA = 0.$$

Then, multiplying (SM4.1) by ψ_{f^ε} , taking the limit $\varepsilon \rightarrow 0$ and assuming (SM4.2) leads to:

$$\int_{\text{SO}_3(\mathbb{R})} (\partial_t(\rho M_{\mathbb{A}}) + c_0 \mathbf{A} \mathbf{e}_1 \cdot \nabla_{\mathbf{x}}(\rho M_{\mathbb{A}})) \psi_{\mathbb{A}}(A) dA = 0.$$

Eq. (2.11b) of the SOHB model follows from this equation through tedious but straightforward computations detailed in [SM3, SM4].

Note that the simple form of the multiplier $\psi_{\mathbb{A}_f}$ is due to a particular simple expression of the collision operator. In more general cases, the obtention of the multiplier (referred to as the generalized collision invariant in [SM6]) is more involved (see e.g. [SM3, SM4, SM5]). A rigorous convergence result for the limit $\varepsilon \rightarrow 0$ is not available to date. In the case of the Vicsek model, such a rigorous result has been proved in [SM8].

SM5. Alternate expressions of δ . The following lemma provides alternate expressions for δ :

Lemma SM5.1. *We have*

$$(SM5.1) \quad \delta = -\{[(\mathbf{u} \cdot \nabla_{\mathbf{x}}) \Omega] \cdot \mathbf{v} + [(\mathbf{v} \cdot \nabla_{\mathbf{x}}) \mathbf{u}] \cdot \Omega + [(\Omega \cdot \nabla_{\mathbf{x}}) \mathbf{v}] \cdot \mathbf{u}\}$$

$$(SM5.2) \quad = -\frac{1}{2} \{(\nabla_{\mathbf{x}} \times \Omega) \cdot \Omega + (\nabla_{\mathbf{x}} \times \mathbf{u}) \cdot \mathbf{u} + (\nabla_{\mathbf{x}} \times \mathbf{v}) \cdot \mathbf{v}\}.$$

172

Proof. Eq. (SM5.1) follows from inserting the formula

$$0 = \nabla_{\mathbf{x}}(\Omega \cdot \mathbf{u}) = (\Omega \cdot \nabla_{\mathbf{x}}) \mathbf{u} + (\mathbf{u} \cdot \nabla_{\mathbf{x}}) \Omega + \Omega \times (\nabla_{\mathbf{x}} \times \mathbf{u}) + \mathbf{u} \times (\nabla_{\mathbf{x}} \times \Omega),$$

and similar formulas after circular permutation of $\{\Omega, \mathbf{u}, \mathbf{v}\}$ into (2.13). Eq. (SM5.2) follows from taking the half sum of (2.13) and (SM5.1) and applying the formula

$$\nabla_{\mathbf{x}} \times \mathbf{v} = \nabla_{\mathbf{x}} \times (\Omega \times \mathbf{u}) = (\nabla_{\mathbf{x}} \cdot \mathbf{u}) \Omega - (\nabla_{\mathbf{x}} \cdot \Omega) \mathbf{u} + (\mathbf{u} \cdot \nabla_{\mathbf{x}}) \Omega - (\Omega \cdot \nabla_{\mathbf{x}}) \mathbf{u},$$

and similar formulas after circular permutation of $\{\Omega, \mathbf{u}, \mathbf{v}\}$. ■

SM6. MO, HW, GS and generalized HW solutions. In this section, we provide proofs of Lemmas 3.1, 3.2 and 3.3. The prototypical helical traveling wave (HW) presented in Lemma 3.2 belongs to a more general class of solutions called generalized HW solutions described in Section SM6.2 below.

SM6.1. Proof of Lemma 3.1. Starting from the initial condition (3.4), we are looking for solutions of (2.11b) of the form

$$\mathbb{A}(t, \mathbf{x}) = \begin{pmatrix} \cos(\omega t) & u_1(t, z) & v_1(t, z) \\ -\sin(\omega t) & u_2(t, z) & v_2(t, z) \\ 0 & u_3(t, z) & v_3(t, z) \end{pmatrix},$$

178 where $\omega \in \mathbb{R}$ is an angular velocity which will be related to the parameters of the problem
 179 later and where the basis vectors $\mathbf{u} = (u_1, u_2, u_3)^\top$ and $\mathbf{v} = (v_1, v_2, v_3)^\top$ depend only on the
 180 z variable and time. In this situation, Equation (2.11a) is trivially satisfied which means
 181 that the system stays homogeneous in space. Solutions of this form have to satisfy three
 182 geometrical constraints which ensure that $\mathbb{A} \in \text{SO}_3(\mathbb{R})$. The first two ones are $\Omega \times \mathbf{u} = \mathbf{v}$ and
 183 $\mathbf{v} \times \Omega = \mathbf{u}$, which lead to

$$184 \text{ (SM6.1)} \quad \mathbb{A}(t, \mathbf{x}) = \begin{pmatrix} \cos(\omega t) & \sin(\omega t)v_3(t, z) & -\sin(\omega t)u_3(t, z) \\ -\sin(\omega t) & \cos(\omega t)v_3(t, z) & -\cos(\omega t)u_3(t, z) \\ 0 & u_3(t, z) & v_3(t, z) \end{pmatrix}.$$

185 The third one is a normalization constraint:

$$186 \text{ (SM6.2)} \quad \forall t > 0, \quad \forall z \in \mathbb{R}, \quad u_3(t, z)^2 + v_3(t, z)^2 = 1.$$

Using (SM6.2), we define a function $\alpha \equiv \alpha(t, z)$ such that

$$u_3(t, z) = \sin(\alpha(t, z)), \quad v_3(t, z) = \cos(\alpha(t, z)).$$

A direct computation shows that for \mathbb{A} of the form (SM6.1), we have

$$\mathbf{r} = (\partial_z u_3) \mathbf{u} + (\partial_z v_3) \mathbf{v}, \quad \delta = 0.$$

187 Therefore, Eq. (2.11b) can be rewritten more concisely into:

$$188 \text{ (SM6.3)} \quad \partial_t \mathbb{A} + c_4 [\Omega \times \mathbf{r}]_\times \mathbb{A} = 0,$$

189 where we recall Eq. (2.9) for the definition of $[\]_\times$. A direct computation shows that

$$190 \text{ (SM6.4)} \quad \Omega \times \mathbf{r} = (v_3 \partial_z u_3 - u_3 \partial_z v_3) \mathbf{e}_3 = (\partial_z \alpha) \mathbf{e}_3.$$

191 Inserting this in (SM6.3) implies that $u_3(t, z) \equiv u_3(z)$ and $v_3(t, z) \equiv v_3(z)$ are independent of
 192 time. We then observe that:

$$193 \text{ (SM6.5)} \quad \mathbb{A}(t, \mathbf{x}) = \mathcal{A}(-\omega t, \mathbf{e}_3) \mathcal{A}(\alpha(z), \mathbf{e}_1),$$

where we recall Eq. (2.8) for the meaning of \mathcal{A} . Therefore, using (SM6.3) and (SM6.4), we obtain:

$$-\omega [\mathbf{e}_3]_\times \mathbb{A} + c_4 (\partial_z \alpha) [\mathbf{e}_3]_\times \mathbb{A} = 0,$$

from which we deduce that \mathbb{A} satisfies (2.11b) if and only if α and ω satisfy:

$$c_4 \partial_z \alpha = \omega,$$

194 which implies

$$195 \text{ (SM6.6)} \quad \alpha(z) = \frac{\omega}{c_4} z + \bar{\alpha},$$

196 where $\bar{\alpha}$ is a constant, which can be interpreted as the phase at the origin $z = 0$. To recover
 197 Eq. (3.2), we just need to take $\bar{\alpha} = 0$ and define $\xi = \omega/c_4$. Eq. (3.3) follows from (SM6.5).

SM6.2. Generalized HW and proof of Lemma 3.2. Starting from the initial condition (3.7), we are looking for solutions of (2.11b) of the form

$$\mathbb{A}(t, \mathbf{x}) = \begin{pmatrix} 1 & 0 & 0 \\ 0 & \cos(\alpha(t, x)) & -\sin(\alpha(t, x)) \\ 0 & \sin(\alpha(t, x)) & \cos(\alpha(t, x)) \end{pmatrix},$$

for a real-valued function α of the t and x variables only. In this case, Ω is a constant vector and Equation (2.18a) is trivially satisfied. Moreover a direct computation shows that:

$$\mathbf{r} = 0, \quad \delta = (\partial_x \alpha)(t, x).$$

As a consequence, Eq. (2.21) is trivially satisfied and straightforward computations show that Eq. (2.11b) reduces to

$$\partial_t \alpha + (c_2 + c_4) \partial_x \alpha = 0.$$

198 This last equation is a linear transport equation with velocity $c_2 + c_4$, the solutions of which
199 are given by

200 (SM6.7)
$$\alpha(t, x) = \alpha_0(x - (c_2 + c_4)t)$$

201 for any initial condition $\alpha_0 \in L^1_{\text{loc}}(\mathbb{R})$. In the case of (3.7), $\alpha_0(x) = \xi x$. However, we see that
202 there are as many different solutions as functions in $L^1_{\text{loc}}(\mathbb{R})$. Such general solutions are called
203 “generalized HW”.

204 **SM6.3. Proof of Lemma 3.3.** The three rotation matrices are given by

205
$$\mathcal{A}(-\omega t, \mathbf{e}_3) = \begin{pmatrix} \cos(\omega t) & \sin(\omega t) & 0 \\ -\sin(\omega t) & \cos(\omega t) & 0 \\ 0 & 0 & 1 \end{pmatrix},$$

206
$$\mathcal{A}(\theta - \pi/2, \mathbf{e}_2) = \begin{pmatrix} \sin \theta & 0 & -\cos \theta \\ 0 & 1 & 0 \\ \cos \theta & 0 & \sin \theta \end{pmatrix},$$

207
$$\mathcal{A}(\xi(z - \tilde{\lambda}t), \mathbf{e}_1) = \begin{pmatrix} 1 & 0 & 0 \\ 0 & \cos(\xi(z - \tilde{\lambda}t)) & -\sin(\xi(z - \tilde{\lambda}t)) \\ 0 & \sin(\xi(z - \tilde{\lambda}t)) & \cos(\xi(z - \tilde{\lambda}t)) \end{pmatrix},$$

210 and a direct computation shows that the three column vectors Ω , \mathbf{u} and \mathbf{v} of the matrix $\mathbb{A}_{\xi, \theta}$
211 are given by

212
$$\Omega = \begin{pmatrix} \sin \theta \cos(\omega t) \\ -\sin \theta \sin(\omega t) \\ \cos \theta \end{pmatrix},$$

213
$$\mathbf{u} = \begin{pmatrix} -\cos \theta \sin(\xi(z - \tilde{\lambda}t)) \cos(\omega t) + \cos(\xi(z - \tilde{\lambda}t)) \sin(\omega t) \\ \cos \theta \sin(\xi(z - \tilde{\lambda}t)) \sin(\omega t) + \cos(\xi(z - \tilde{\lambda}t)) \cos(\omega t) \\ \sin \theta \sin(\xi(z - \tilde{\lambda}t)) \end{pmatrix},$$

214

215

$$216 \quad \mathbf{v} = \begin{pmatrix} -\cos\theta \cos(\xi(z - \tilde{\lambda}t)) \cos(\omega t) - \sin(\xi(z - \tilde{\lambda}t)) \sin(\omega t) \\ \cos\theta \cos(\xi(z - \tilde{\lambda}t)) \sin(\omega t) - \sin(\xi(z - \tilde{\lambda}t)) \cos(\omega t) \\ \sin\theta \cos(\xi(z - \tilde{\lambda}t)) \end{pmatrix}.$$

217 Then we compute

$$218 \quad \mathbf{r} = \xi \sin\theta \cos(\xi(z - \tilde{\lambda}t))\mathbf{u} - \xi \sin\theta \sin(\xi(z - \tilde{\lambda}t))\mathbf{u} = \xi \sin\theta (\sin(\omega t), \cos(\omega t), 0)^\top,$$

$$219 \quad \delta = \cos\theta \partial_z \mathbf{u} \cdot \mathbf{v} + u_3 \delta_z \mathbf{v} \cdot \Omega = \xi \cos\theta,$$

221 where we have used that $\partial_z \mathbf{u} = \xi \mathbf{v}$ and $\partial_z \mathbf{v} = -\xi \mathbf{u}$. It remains to check that Eq. (2.11b)
222 holds true. We split this equation into three equations, one for each vector Ω , \mathbf{u} and \mathbf{v} . The
223 first equation on Ω reads

$$224 \quad (\partial_t + c_2(\Omega \cdot \nabla_{\mathbf{x}}))\Omega + c_4 P_{\Omega^\perp} \mathbf{r} = 0.$$

225 This equation holds true because

$$226 \quad \partial_t \Omega = -\omega \begin{pmatrix} \sin\theta \sin(\omega t) \\ \sin\theta \cos(\omega t) \\ 0 \end{pmatrix}, \quad (\Omega \cdot \nabla_{\mathbf{x}})\Omega = 0, \quad P_{\Omega^\perp} \mathbf{r} = \mathbf{r} - (\mathbf{r} \cdot \Omega)\Omega = \xi \sin\theta \begin{pmatrix} \sin(\omega t) \\ \cos(\omega t) \\ 0 \end{pmatrix},$$

227 and $\omega = c_4 \xi$. The second equation on \mathbf{u} reads

$$228 \quad (\partial_t + c_2(\Omega \cdot \nabla_{\mathbf{x}}))\mathbf{u} - c_4(\mathbf{u} \cdot \mathbf{r})\Omega + c_4 \delta \mathbf{v} = 0.$$

Because $\tilde{\lambda} = c_2 \cos\theta$, we have

$$\partial_t + c_2 \Omega \cdot \nabla_{\mathbf{x}} = \partial_t + c_2 \cos\theta \partial_z = \partial_t + \tilde{\lambda} \partial_z \quad \text{and} \quad \partial_t + \tilde{\lambda} \partial_z (z - \tilde{\lambda}t) = 0.$$

Thus

$$(\partial_t + c_2(\Omega \cdot \nabla_{\mathbf{x}}))\mathbf{u} = \omega \begin{pmatrix} \cos\theta \sin(\xi(z - \tilde{\lambda}t)) \sin(\omega t) + \cos(\xi(z - \tilde{\lambda}t)) \cos(\omega t) \\ \cos\theta \sin(\xi(z - \tilde{\lambda}t)) \cos(\omega t) - \cos(\xi(z - \tilde{\lambda}t)) \sin(\omega t) \\ 0 \end{pmatrix},$$

229 and using $\omega = c_4 \xi$, it can be checked that

$$230 \quad (\partial_t + c_2(\Omega \cdot \nabla_{\mathbf{x}}))\mathbf{u} - c_4(\mathbf{u} \cdot \mathbf{r})\Omega = -c_4 \xi \cos\theta \mathbf{v} = -c_4 \delta \mathbf{v},$$

231 which yields the result. The equation on \mathbf{v} is analogous.

SM6.4. GOP of the MO and generalized HW. The GOP (given by Eq. (4.5)) of the MO and HW do not depend on time and only depend on the function α defined respectively by (SM6.6) and (SM6.7). Using Eq. (4.5), we can compute that the GOP is equal to:

$$\text{GOP} = \frac{1}{2} \left(\frac{c_1(\kappa)}{c_0} \right)^2 (1 + 2|\langle \mathbf{u} \rangle|^2) + \frac{1}{4},$$

where $\langle \mathbf{u} \rangle$ denotes the spatial average of the vector \mathbf{u} with respect to ρ (here the with respect to the uniform measure on the domain since ρ is constant and uniform). With the previous notations, we obtain

$$|\langle \mathbf{u} \rangle|^2 = \langle \cos \alpha \rangle^2 + \langle \sin \alpha \rangle^2,$$

232 For the generalized HW, depending on the choice of α , the GOP can take any value between
 233 GOP_1 and GOP_2 , these two extreme values being attained respectively when $|\langle \mathbf{u} \rangle| = 0$ and
 234 $|\langle \mathbf{u} \rangle| = 1$.

235 **SM7. Convergence rate of $|\text{d}\bar{\varphi}/\text{d}t|$ as $N \rightarrow \infty$.** The fact that the convergence rate of
 236 $|\text{d}\bar{\varphi}/\text{d}t|$ is close to N^{-1} agrees with previously documented observations in spherical statistics.
 237 Indeed, it has been shown in [SM11, Theorem 3(e)] that the estimation of the concentration
 238 parameter of a (spherical) von Mises distribution obtained from a crude averaging procedure
 239 from N independent samples produces a biased estimator with a (nonnegative) bias of order
 240 N^{-1} (see also [SM10, Section 10.3]). In the present case, a similar reasoning can be applied,
 241 which we now briefly develop. The key observation is that all the measured quantities are
 242 functions of empirical averages of the form (2.4). Under the chaos assumption (see Section
 243 SM4), when N is large, the body-orientations of the particles behave as N independent samples
 244 with common law $M_{\mathbb{A}}$, where \mathbb{A} solves the SOHB model (2.11) and $M_{\mathbb{A}}$ is defined by (2.6). In
 245 [SM3, Theorem 4.1], it has been shown that $c_4(\kappa)$ can actually be expressed as a function of
 246 a certain number p of averaged quantities

$$247 \quad c_4(\kappa) = F(\langle g_1 \rangle_{M_{\mathbb{A}}}, \dots, \langle g_p \rangle_{M_{\mathbb{A}}}),$$

248 where $g_i : \text{SO}_3(\mathbb{R}) \rightarrow \mathcal{M}_3(\mathbb{R})$ and $F : \mathcal{M}_3(\mathbb{R})^p \rightarrow \mathbb{R}$ are smooth functions. The IBM simulation
 249 thus defines an estimator $\hat{\kappa}$ of the concentration parameter such that

$$250 \quad c_4(\hat{\kappa}) = F(\hat{g}_1, \dots, \hat{g}_p),$$

251 where \hat{g}_i is the average of g_i obtained by replacing $M_{\mathbb{A}}$ by the empirical measure of the N
 252 body-orientations of the particles. We can then measure the bias by taking the expectation
 253 of the Taylor expansion of the previous expression around the point $(\langle g_1 \rangle_{M_{\mathbb{A}}}, \dots, \langle g_p \rangle_{M_{\mathbb{A}}})$:

$$254 \quad c_4(\hat{\kappa}) = c_4(\kappa) + \delta \hat{\mathbf{g}} \cdot \nabla F + (\delta \hat{\mathbf{g}})^{\text{T}} (\text{Hess } F) \delta \hat{\mathbf{g}} + R,$$

255 where $\delta \hat{\mathbf{g}} = (\hat{g}_1, \dots, \hat{g}_p)^{\text{T}} - (\langle g_1 \rangle_{M_{\mathbb{A}}}, \dots, \langle g_p \rangle_{M_{\mathbb{A}}})^{\text{T}}$ and R is a remainder. The gradient ∇
 256 and Hessian Hess are defined within the Euclidean framework given by (2.1). By the chaos
 257 hypothesis $\mathbb{E}[\delta \hat{\mathbf{g}}] = 0$ and by the central limit theorem, the term of order two behaves as
 258 N^{-1} . Since $\text{SO}_3(\mathbb{R})$ is compact, higher order moments of $\delta \hat{\mathbf{g}}$ can be controlled by a classical
 259 argument based on Hoeffding's inequality [SM12, Lemma 5.5 and Theorem 5.29]. This ensures
 260 that $\mathbb{E}[R]$ is $\mathcal{O}(N^{-2})$. We therefore obtain a biased estimator:

$$261 \quad \mathbb{E}[c_4(\hat{\kappa})] = c_4(\kappa) + \frac{a}{N} + \mathcal{O}(N^{-2}),$$

262 where $a \in \mathbb{R}$ depends on the derivatives of the considered functions and on the variance of
 263 the estimator (2.4) where the particles are replaced by independent identically distributed

264 samples with law $M_{\mathbb{A}}$. The fact that $a > 0$ can be empirically verified on Fig. 8b but has
 265 not been proved yet. For each N , the fluctuations around the average (biased) value can be
 266 monitored by computing the standard deviation of the 10 independent simulations. Fig. SM1
 267 shows this standard deviation as a function of N in a log-log-scale (blue dots). Although
 268 fluctuations remain significant with only 10 simulations per data point, by a standard linear
 269 regression (solid orange line) we obtain that the size of the standard deviation behaves as
 270 $N^{-\beta}$ with $\beta \simeq 0.54$, which is close to the value $\beta = 1/2$ which we expect from an application
 271 of the central limit theorem.

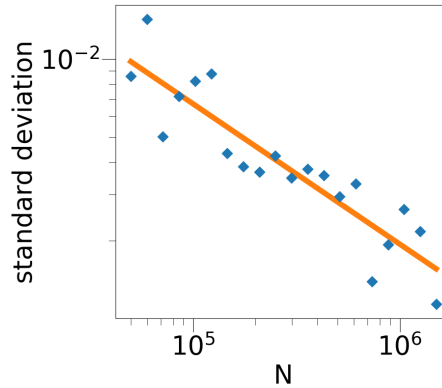


Figure SM1: Standard deviation of the 10 independent simulations as a function of N (blue dots) and regression line (solid orange line) in log-log scale. Parameters: $L = 1$, $\xi = 2\pi$, $R = 0.025$, $\nu = 40$, $c_0 = 1$, $\kappa = 10$.

272 **SM8. Rare events.** Although the scenario described in Section 5 of the main text is
 273 the most common one, the IBM sometimes leads to different, slightly more complex scenarios
 274 which are described in the present section. Now, the IBM is initialized by drawing N positions
 275 independently uniformly in the cubic domain $\mathcal{D} = [0, L] \times [0, L] \times [0, L]$ with periodic boundary
 276 conditions and N body-orientations independently from the von Mises distribution $M_{\mathbb{A}(0, \mathbf{x})}$
 277 where $\mathbb{A}(0, \mathbf{x})$ is given by (3.4) with $\xi = 2\pi/L$ (winding number equal to 1).

278 **SM8.1. From milling orbit to helical wave.** Here, we report on the occurrence of transi-
 279 tions from a MO to a HW. Among twenty independent simulations, this transition occurred
 280 only once (the other cases being a transition from a MO to a FS). We run the IBM and
 281 record the time-evolution of a set of indicators as shown in Fig. SM2 (see also supplementing
 282 videos 12 to 14 in Section SM1).

283 As shown in Fig. SM2a, the GOP does not converge towards GOP_2 characterizing the
 284 FS, but towards an intermediate value between GOP_1 (which characterizes MO or HW) and
 285 GOP_2 . As explained in Section SM6.4, such values of the GOP can be attained by a generalized
 286 helical wave solution (as can be observed in Video 12). The pitch $\bar{\theta}$ (Fig. SM2b) and yaw $\bar{\varphi}$
 287 (Fig. SM2c) behave like in the milling-to-flocking transition (see Figs. 13b and 13c) except for
 288 small-amplitude, slow-frequency oscillations appearing after the topological transition time.
 289 This may be due to some competition between two attractors, the FS and the HW, which being

290 alternately stronger and weaker, generate this oscillatory behavior. Note that a transition to a
 291 HW cannot occur when the global direction of motion at the transition time is not one of the
 292 principal axes of the square domain since a HW along another direction is not compatible with
 293 the periodic boundary conditions (see Section SM8.2). This is confirmed by the final values of
 294 $\bar{\varphi}$ and $\bar{\theta}$ (both equal to $\pi/2$) which correspond to a global direction of motion oriented along
 295 the y -axis (in what follows, in reference to (5.4) and to avoid confusion, we will still call that
 296 direction, the x direction).

297 The second and third lines of figures in Fig. SM2 show the triplets of topological indicators
 298 (d_z, \bar{r}_z, w_z) and (d_x, \bar{r}_x, w_x) which materialize the MO and HW structures respectively. The
 299 mean distance of the RPZ-curve to the origin \bar{r}_z (Figs. SM2e) decreases, revealing an increase
 300 of the disorder. Simultaneously, the distance of its center of mass to the origin d_z increases
 301 (Figs. SM2d) showing a transition trend to a FS. The winding number w_z (Fig. SM2f)
 302 jumps from 1 to 0 at the time of maximal disorder. However, d_z and \bar{r}_z do not reach zero,
 303 showing that complete disorder across z is not reached. Since the final state of the system
 304 is a generalized helical wave state (see Section SM6.4), we do not necessarily expect that
 305 complete disorder will be reached along the z -direction. In the mean time, \bar{r}_x starts from 0
 306 (complete disorder) and increases up to a value close to unity, showing the build-up of a HW.
 307 The quantity d_x increases during some time but eventually decreases to 0 (not shown in the
 308 figure) as it should for a HW. Finally, the winding number w_x is undefined in the initial stage,
 309 as it should for complete disorder, but builds up to 1 at the time where the winding number
 310 w_z drops to 0. There is a transfer of non-trivial topology from an MO structure to a HW
 311 structure.

312 **SM8.2. From milling to flocking via a helical wave state.** In some rare cases an inter-
 313 mediate unstable HW can be observed. Note that due to the periodic setting, an HW cannot
 314 be stable for most of the the global directions of motion. Although stable or unstable HW
 315 typically appear in one over twenty of our simulations, it should be kept in mind that the
 316 occurrence frequency also depends on the geometry of the domain and that this phenomena
 317 may be more frequent for other simulation settings. The procedure is the same as in the
 318 previous section. Fig. SM3 shows the results (see also supplementing videos 15 and 16 in
 319 Section SM1).

320 The transition stage between the MO and FS is significantly longer than in the previous
 321 situations. During that phase, the GOP (Fig. SM3a) oscillates between the value Ψ_1 charac-
 322 terizing the MO and lower values, i.e. lower order. Likewise, there are significant variations
 323 of the pitch $\bar{\theta}$ (Fig. SM3b) and yaw $\bar{\varphi}$ (Fig. SM3c). As in the previous section, this could be
 324 explained by antagonist effects of different attractors (the MO and HW) and subsequent os-
 325 cillations of the system between them. Video 15 reveals large scale band structures similar to
 326 a HW except that the global direction of motion is not one of the principal axes of the square
 327 domain. As, in most cases, this cannot be compatible with the periodic boundary conditions,
 328 such state cannot persist in time. The relatively long-time persistence of this stage could be
 329 explained in the present case by the fact that the global direction of motion seems to oscillate
 330 around the direction given by $\mathbf{e}_1 + \mathbf{e}_2$ (i.e. $\varphi = \pi/4$ and $\theta = \pi/2$) which is theoretically com-
 331 patible with the periodic boundary conditions, provided the wave length ξ is changed from
 332 $2\pi/L$ to $\sqrt{2}\pi/L$. This state does not seem to be stable as shown by the large oscillations of $\bar{\varphi}$

333 and $\bar{\theta}$. The topological indicators (d_z, \bar{r}_z, w_z) shown in the second line of figures of Fig. SM3
334 also display large oscillations. The quantity \bar{r}_z drops, and at the same time, d_z remains small,
335 while the winding number w_z has strong oscillations, indicating a state of large disorder across
336 z , which is consistent with the fact that the temporary HW order is organized in a different
337 direction. However, we see that w_z has a calmer period between two series of oscillations.
338 This calmer period corresponds to the interval of time during which the temporary HW order
339 prevails. Eventually the triplet converges to the value $(1, 1, 0)$ characterizing the FS.

340

REFERENCES

- 341 [1] F. BOLLEY, J. A. CAÑIZO, AND J. A. CARRILLO, *Mean-field limit for the stochastic Vicsek model*, Appl.
342 Math. Lett., 25 (2012), pp. 339–343.
- 343 [2] P. DEGOND, A. DIEZ, A. FROUVELLE, AND S. MERINO-ACEITUNO, *Phase transitions and macroscopic*
344 *limits in a BGK model of body-attitude coordination*, J. Nonlinear Sci., 30 (2020), pp. 2671–2736.
- 345 [3] P. DEGOND, A. FROUVELLE, AND S. MERINO-ACEITUNO, *A new flocking model through body attitude*
346 *coordination*, Math. Models Methods Appl. Sci., 27 (2017), pp. 1005–1049.
- 347 [4] P. DEGOND, A. FROUVELLE, S. MERINO-ACEITUNO, AND A. TRESCASES, *Quaternions in collective*
348 *dynamics*, Multiscale Model. Simul., 16 (2018), pp. 28–77.
- 349 [5] P. DEGOND, A. FROUVELLE, S. MERINO-ACEITUNO, AND A. TRESCASES, *Alignment of self-propelled rigid*
350 *bodies: from particle systems to macroscopic equations*, in Stochastic Dynamics Out of Equilibrium,
351 G. Giacomin, S. Olla, E. Saada, H. Spohn, and G. Stoltz, eds., vol. 282 of Springer Proceedings
352 in Mathematics and Statistics, Institut Henri Poincaré, Paris, France, 2017, Springer International
353 Publishing, 2019, pp. 28–66.
- 354 [6] P. DEGOND AND S. MOTSCH, *Continuum limit of self-driven particles with orientation interaction*, Math.
355 Models Methods Appl. Sci., 18 (2008), pp. 1193–1215.
- 356 [7] A. DIEZ, *Propagation of chaos and moderate interaction for a piecewise deterministic system of geomet-*
357 *rically enriched particles*, Electron. J. Probab., 25 (2020).
- 358 [8] N. JIANG, L. XIONG, AND T.-F. ZHANG, *Hydrodynamic limits of the kinetic self-organized models*, SIAM
359 J. Math. Anal., 48 (2016), pp. 3383–3411.
- 360 [9] J. T. KENT, A. M. GANEIBER, AND K. V. MARDIA, *A new unified approach for the simulation of a wide*
361 *class of directional distributions*, J. Comput. Graph. Statist., 27 (2018), pp. 291–301.
- 362 [10] K. V. MARDIA AND P. E. JUPP, *Directional Statistics*, vol. 494, John Wiley & Sons, 2009.
- 363 [11] G. SCHOU, *Estimation of the concentration parameter in von Mises–Fisher distributions*, Biometrika, 65
364 (1978), pp. 369–377.
- 365 [12] R. VERSHYNIN, *Introduction to the non-asymptotic analysis of random matrices*, in Compressed sensing,
366 theory and applications, Y. C. Eldar and G. Kutinyok, eds., Cambridge University Press, 2012,
367 pp. 210–260.

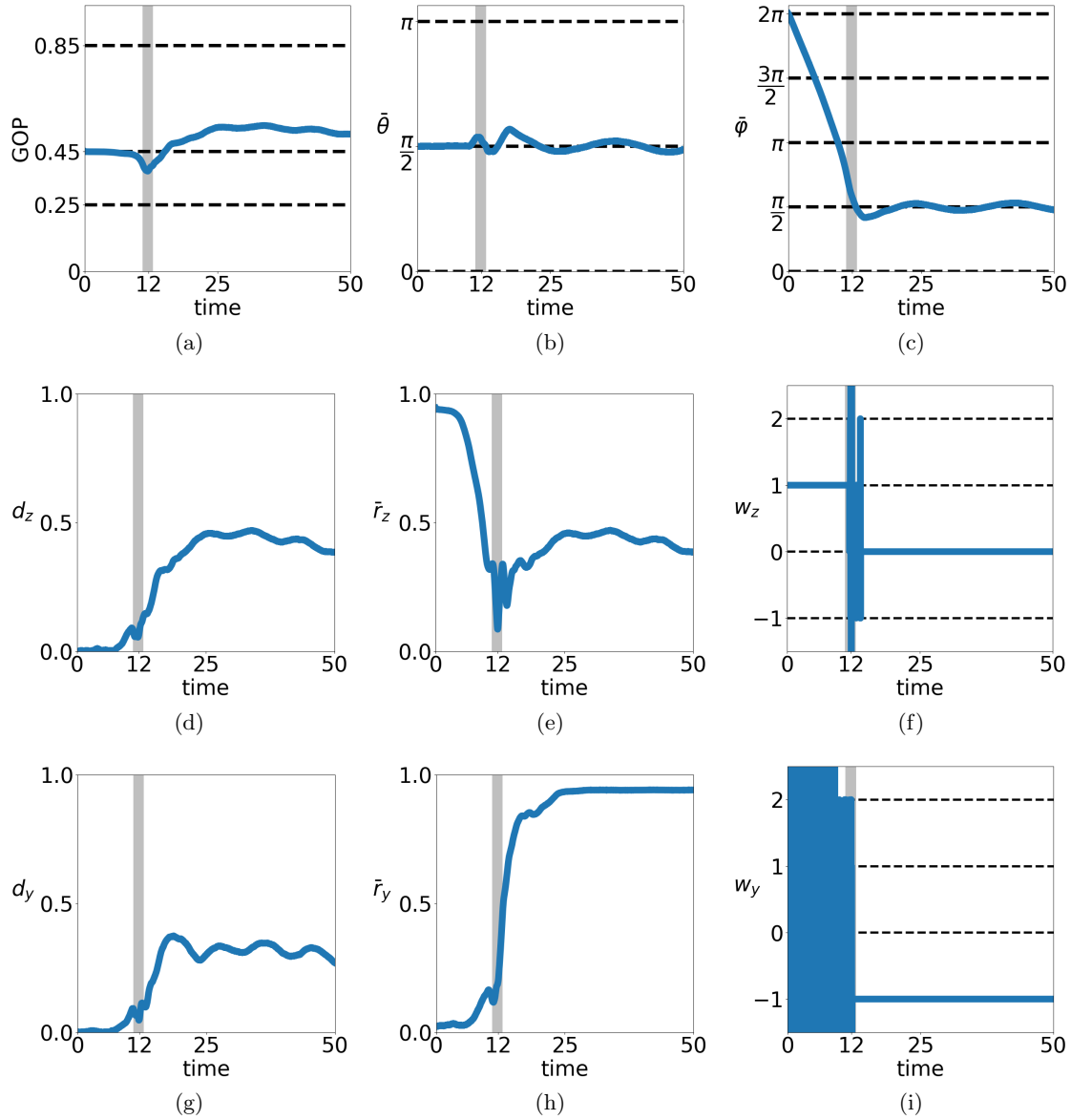


Figure SM2: Transition from a MO to a HW: example of a solution of the IBM for an initial condition sampled from (5.1) in the rare case where it leads to a HW. The following indicators are plotted as functions of time: (a) GOP (b) Pitch $\bar{\theta}$ of $\bar{\Omega}$. (c) Yaw $\bar{\varphi}$ of $\bar{\Omega}$. (d) Distance of center of mass of RPZ curve to the origin d_z . (e) Mean distance of RPZ curve to the origin \bar{r}_z . (f) Winding number of RPZ curve w_z . (g) Distance of center of mass of RPX curve to the origin d_x . (h) Mean distance of RPX curve to the origin \bar{r}_x . (i) Winding number of RPX curve w_x . Gray shaded zones highlight a small region around the time of minimal GOP. Parameters: $N = 1.5 \cdot 10^6$, $R = 0.025$, $L = 1$, $D = 0.1$, $\nu = 40$, $c_0 = 1$. See caption of Fig. 13 for further indications. See also Videos 12 to 14 in Section SM1.

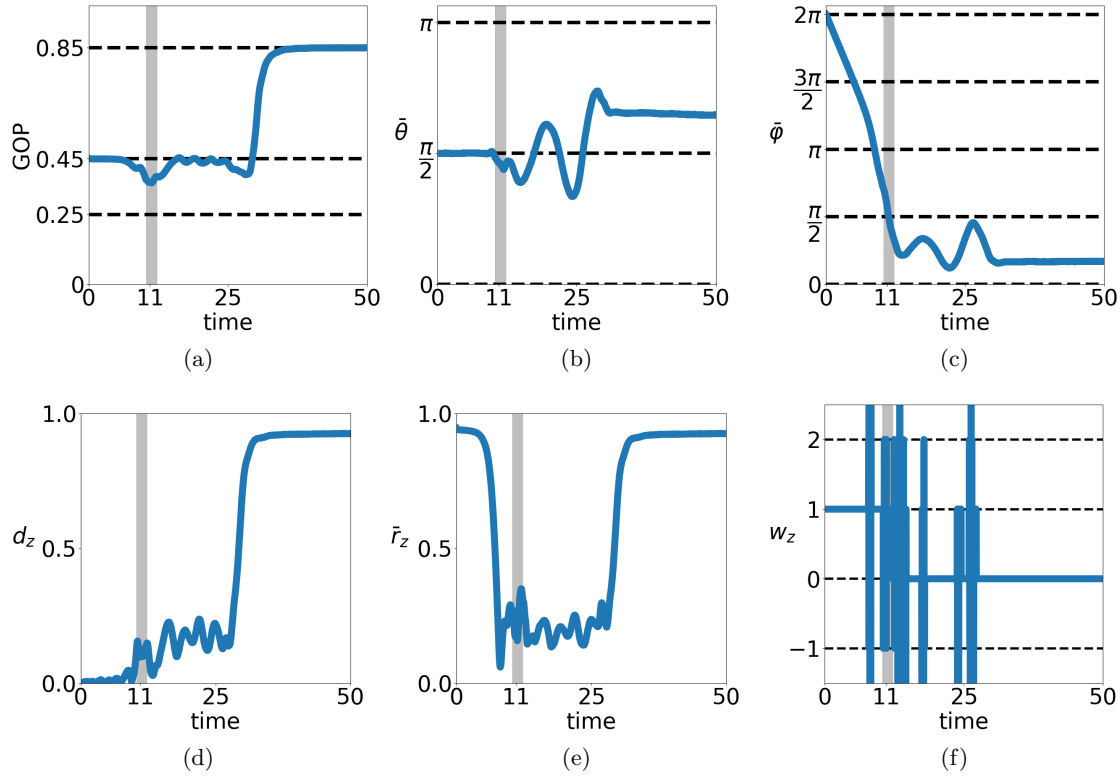


Figure SM3: Transition from a MO to a FS via an unstable HW: example of a solution of the IBM for an initial condition sampled from (5.1) in the rare case where it leads to a FS through a transient HW. The following indicators are plotted as functions of time: (a) GOP (b) Pitch $\bar{\theta}$ of $\bar{\Omega}$. (c) Yaw $\bar{\varphi}$ of $\bar{\Omega}$. (d) Distance of center of mass of RPZ curve to the origin d_z . (e) Mean distance of RPZ curve to the origin \bar{r}_z . (f) Winding number of RPZ curve w_z . Gray shaded zones highlight a small region around the time of minimal GOP. Parameters: $N = 1.5 \cdot 10^6$, $R = 0.025$, $L = 1$, $D = 0.1$, $\nu = 40$, $c_0 = 1$. See caption of Fig. 13 for further indications. See also Videos 15 and 16 in Section SM1.